Kinetics of the Initial Stages of Platinum Oxidation

by

Natalie Stubb
B.Sc., University of Redlands, 2017

A Thesis Submitted in Partial Fulfillment of the
Requirements for the Degree of

Master of Science

in the Department of Chemistry

Kinetics of the Initial Stages of Platinum Oxidation

by

Natalie Stubb

B.Sc., University of Redlands, 2017

Supervisory Committee

Dr. D. A. Harrington, Supervisor (Department of Chemistry)

Dr. I. Paci, Departmental Member (Department of Chemistry)

Supervisory Committee

Dr. D. A. Harrington, Supervisor (Department of Chemistry)

Dr. I. Paci, Departmental Member (Department of Chemistry)

Abstract

The kinetics of the oxidation of platinum metal have long been a topic of interest in the field of electrochemistry. Using a combination of cyclic voltammetry, potential step experiments, and sweep-hold experiments, this research studies the kinetics of the initial stages of oxide growth on Pt(100), Pt(111), and Pt(110) surfaces. By comparing the electrochemical results with surface X-ray diffraction (SXRD) experiments conducted at synchrotron facilities, it was found that the charge of the oxide peak is within 15 μC cm^{-2} or about 0.1 ML for all three surfaces. This means that the amount of oxide formed on each surface is similar. It was also determined that the oxide formed on Pt(111) is a Pt(II) species, consistent with an oxide like PtO. From calculations from the potential step experiments, it was determined that on Pt(100) there are two distinct regions of current decay, but that double layer charging is not one of the two seen. Instead, it was determined that the oxidation is likely a two step process with the first step being an adsorption step and the second being a place exchange oxide formation step. It was also found that more charge is passed when conducting potential step experiments to the oxide region from potentials in the hydrogen underpotential deposition (HUPD) region than from potentials in the double layer region. Finally, the results of a sweep-hold experiment on Pt(100) show that the values for charge are similar when calculated via the data from a sweep-hold and potential step experiment from a potential in the double layer region. The results of this research help further the kinetic understanding of the platinum surface during

its oxidation and reduction.

Table of Contents

List of Figures

Nomenclature

Variable	*Meaning*	*Units*
$\mathbf{a}, \mathbf{b}, \mathbf{c}$	Real space crystallographic vectors	Å
$\mathbf{a}^*, \mathbf{b}^*, \mathbf{c}^*$	Reciprocal space crystallographic vectors	$Å^{-1}$
A	Surface area	cm^2
C	Capacitance	F cm^{-2}
E	Potential	V
F	Faraday's constant	C mol^{-1}
G	Conductance	S cm^{-2}
h	Planck's constant	J s
I	Current	A
j	Current density	A cm^{-2}
k	Wavevector of the X-ray beam	$Å^{-1}$
p	Momentum	kg m s^{-1}
Q	Charge	C
R	Resistance	Ω cm^2

Greek	*Meaning*	*Units*
θ	Surface coverage	ML
κ	Conductivity	S cm^{-1}
λ	Eigenvalue	
σ	Surface charge density	μC cm^{-2}
π	Mathematical constant	
ρ	Resistivity	Ω cm
τ	Time constant	s
ϕ	General angle	rad
Ψ	Wave Function	

Subscript	*Meaning*
beam	X-ray beam
cubic	Cubic unit cell
dl	Double layer region
e	Electron
hex	Hexagonal unit cell
i	Initial
ml	Monolayer
p	Peak
Pt(100)	Platinum 100 surface
Pt(111)	Platinum 111 surface
s	Solution

Acknowledgements

I would first like to thank the University of Victoria for providing me the opportunity to continue in my studies in such a beautiful part of the world. I would also like to acknowledge the ESRF and DESY scientists and beamline staff for allowing us time and technical support at the synchrotrons to complete this work, especially our collaborator at the ESRF, Jakub Drnec. In addition, I would like to thank our collaborators at the University of Kiel, namely Timo Fuchs and Olaf Magnussen, who have made this journey so memorable and informative. I would also like to acknowledge my group members and other Chemistry department colleagues, as they have been an invaluable source of knowledge and compassion during my time at UVic. I would additionally like to thank my parents for always being incredibly supportive of my journey. Finally, I would like to thank my supervisor, David Harrington, for his continued support and mentorship throughout my time at UVic.

To my parents.

Chapter 1

Introduction

As a society we are currently in the midst of climate change discussions, and one of the recurring themes is how to combat global warming. A major output of these discussions has been an increased demand for renewable energy sources. A growing area of interest in the search for green energy has been in the development of fuel cells because they don't produce harmful greenhouse gas emissions while converting chemical energy into electricity [1–5]. Fuel cells themselves are not a new concept; they were invented in the nineteenth century and use an oxidation-reduction (redox) reaction between oxygen and hydrogen to produce electricity and water [6]. They are notably how the National Aeronautics and Space Administration (NASA) generated power in space during the 1960s [7].

The technology behind and diversity in the types of fuel cells in today's market has advanced substantially since then, and current research and production shows continued signs of growth in the field [8–13]. Alkaline fuel cells (AFCs) are depended upon in many space programs to this day and are very well developed. They are relatively cheap to make, can utilize over 60% of the chemical energy in hydrogen (as compared to a standard combustion engine which can only use 20% to generate work), and they operate at standard temperatures [14–18]. However if AFCs are exposed

to carbon dioxide, there is a poisoning effect that causes a buildup of carbonate salt inside the cell and blocks the flow of gases ultimately resulting in a power failure [19, 20]. This need to be kept from carbon dioxide adds difficulty and cost to the use of AFCs. The answer to this was the development of phosphoric acid fuel cells (PAFCs). These types of fuel cells are tolerant to carbon dioxide, and are highly commercialized. PAFCs are great for stationary power needs such as in a hotel or hospital, but operate at higher temperatures than AFCs and aren't as portable [21,22]. One type of fuel cell that appears to be promising is the proton exchange membrane fuel cell (PEMFC) [23–25]. These types of fuel cells work similarly to PAFCs, but are praised for their low operating temperatures and pressures and have a higher power density output. PEMFCs still have limitations [26–28] but most prominently have expensive noble metal components such as platinum metal, which is common in PEMFCs because of its stability at high temperatures, resistance to corrosion, and ability to effectively catalyze the oxidation and reduction reactions which are crucial to the operation of the cell [24, 29, 30].

Over the years, platinum has continued to be the standard for electrocatalytic reactions [31–34]. However it also degrades in aqueous environments and in the presence of carbon monoxide, which renders it less capable to catalyze the pivotal surface reactions required in PAFCs and PEMFCs [11,12,35]. The design of both PAFCs and PEMFCs requires the platinum metal catalyst to be subjected to an aqueous environment, and so understanding how the oxidation and reduction reactions occur in this environment on an atomic level can help us to establish conditions that optimize the efficiency of the metal and help prevent degradation of the catalyst. Unfortunately even after many years of study, the complete mechanism of these processes are still unknown [33, 36–40]. To help further this understanding, the kinetics of the initial stages of platinum oxidation is the focus of this research. PEMFCs utilize platinum nanoparticles in order to reduce material costs and overall weight due to their high surface area to volume ratio [41]. Our fundamental research uses macro-scale plat-

inum single crystals in aqueous environments to gain an understanding of the surface processes, and the results of this work can hopefully be applied to the nanoparticles in PEMFCs.

The goals of this research are focused on furthering the understanding of the kinetics of the initial stages of forming oxide on the three low index platinum surfaces. First, we wanted to probe the Pt(100), Pt(110), and Pt(111) surfaces through use of cyclic voltammetry to see how they compare. Second, we were interested in knowing the oxidation state of the oxide that is formed on the surface which we explored through cyclic voltammogram peak integration. Additionally, we wanted to know the number of electrons per place exchanged surface platinum atom for this process which involved the comparison of cyclic voltammogram data with X-ray diffraction data. Next, we use step experiments from various potentials in order to test for the number of elementary steps involved in the formation of oxide and begin the process of finding a kinetic rate law for the process. Finally, we wanted to compare step experiments to sweep-hold experiments to see what kinetic information could be gained from each type of experiment.

In order to effectively convey the relevant background and the results of this research, this thesis is divided into five chapters. Chapter 2 discusses the fundamental concepts of this work, as well as provides a literature review of the history of platinum as it pertains to this research. Chapter 3 examines the experimental methods implemented and reviews fundamental equations and concepts relevant to interpreting the results of the techniques used. Chapter 4 presents the results of the work done in this research, and Chapter 5 provides conclusions and future directions for the project.

Chapter 2

Fundamental Concepts and Literature

In this chapter, some fundamental concepts of electrochemistry will be covered. The simple circuit, the double layer, and solution resistance will be explored, as well as a description of the types of electrochemical experiments conducted in this research. Additionally, surface chemistry for the platinum surfaces used in this research will be described, and the concept of coverage will be explained. Finally, a brief history of platinum electrochemistry will be given which will include the theory of place exchange.

2.1 Introduction to Electrochemistry

Electrochemistry is the study of the relationship between electricity and chemical reactions, and the conversion between the two. An electrochemical reaction is a chemical reaction that either produces electrons or requires them to proceed. These electrons cross the interface between an electrode and electrolyte and result in the production of an electric current. Though electrochemistry is just a small branch of

the field of chemistry as a whole, its concepts have applications in physics, engineering, biology, and even within other branches of chemistry as an analysis technique [10, 42–45].

It is a long standing field of research, dating back to as early as 1799 when Alessandro Volta wrote a letter to the president of the Royal Society of London describing what would come to be the first battery, which he called his "electric pile" that could continuously provide electrical current [46]. Soon after, several scientists confirmed this discovery that electricity could be generated from chemical reactions and this new field of research began to gain momentum with researchers like Georg Ohm and Michael Faraday, whose laws now govern much of how we understand electricity. Early electrochemists were responsible for separating water into its components of hydrogen and oxygen in a process known as electrolysis [47, 48], and for the creation of the first galvanic cell which produced electricity and also allowed for the separation of many chemical compounds into their individual elements for the first time [49]. The first fuel cell was created in 1839 by William Grove, and about one hundred years of development later Francis T. Bacon produced an improved version with his hydrogen-oxygen fuel cell (an early AFC), which was the first to be sold commercially [6].

Both fuel cells and batteries are pivotal to our modern society, and are still widely studied because of their improved efficiency over combustion engines and their potential to advance green energy [6, 50, 51]. It is probably for this reason that modern electrochemical research is focused on the development of less toxic and more efficient batteries and fuel cells. The Nobel Prize in 2019 was awarded to John B. Goodenough, M. Stanley Whittingham, and Akira Yoshino: three chemists working in the field of electrochemistry who are credited with the combined discovery of the lithium-ion battery, which is used in almost every portable electronic device. The research discussed in this thesis is fundamental work, which looks at the kinetics of the very beginning stages of electrochemical oxidation of platinum metal, and which

has relevance to the development of fuel cells.

2.1.1 The Simple Circuit

Understanding the ideas of current, electric potential, resistance, and the elements of a simple circuit are essential to understanding how electricity, and therefore electrochemical reactions, work. Current, denoted as I, is the rate of flow of electric charge through a specified object or area and is measured in amperes (A). Electric potential, written as V, is the driving force for moving charges from one point to another and is measured in volts (V). Resistance, represented as R, is a measure of an object's opposition to pass electrical current and is measured in ohms (Ω). For a linear resistance, the current, potential, and resistance are all related through a mathematical equation known as Ohm's Law, written in Eq. 2.1.

$$V = IR \tag{2.1}$$

It is standard in the field of electrochemistry to rewrite Ohm's law with E as electric potential. Additionally, in this thesis current will be denoted as current density, (j), which is current per unit area, and resistance will be expressed in Ω cm^2. Thus Ohm's law will be recast as $E = jR$. Visually, Ohm's Law can be represented by the simplest of electrical circuits, as shown as **A** in Fig. 2.1, where the section labeled R is a resistor and the part labeled V is the object supplying a voltage (like a battery, for example). These components are connected by wires represented as lines.

More commonly, another element known as a capacitor is also part of the circuit. A capacitor is an object that stores electrical energy. It consists of two metal plates with a dielectric in between. An example of how a capacitor can be incorporated into a circuit is shown as **B** in Fig. 2.1, where the circuit is similar to the simple circuit in part **A**, with only the addition of the capacitor (C). For a linear capacitance, $C = Q/V$, where Q is charge. Although Ohm's Law is helpful in determining some

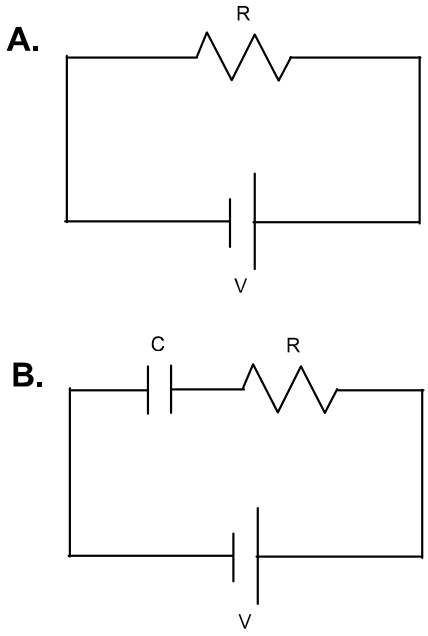

Figure 2.1: Two examples of simple circuits. **A** includes only a resistor (labeled R) and a voltage supply (labeled V). **B** has the same components as **A**, but also includes a capacitor (labeled C). The components are all connected by wires, represented by lines, through which electrons flow.

values in this research and is given here with a few basic circuit diagrams for that reason, it is important to note that it does not apply for electrochemical reactions because of the nonlinear relationship between current and potential in those reactions. For nonlinear resistance and capacitance, we use the relationships shown in Eq. 2.2 and 2.2.

$$R = \frac{dV}{dI} \tag{2.2}$$

$$I = C\frac{dV}{dt} \tag{2.3}$$

2.1.2 The Electrochemical Cell and Potentiostat

An electrochemical cell is used to conduct electrochemical experiments. Each experiment can be described by an equivalent circuit like the ones described in the previous section depending on how the cell is setup. In the cell there are three electrodes;

the working electrode (WE), the counter electrode (CE) and the reference electrode (RE), all immersed in an electrolyte solution and connected to a potentiostat, which acts as the battery in our simple circuit diagram and drives current through the cell.

A schematic of a simple electrochemical cell is shown in Fig. 2.2. The flow of electrons depends on the set up of the cell and the potentiostat, but in this research a potential difference is established between the working electrode and the reference electrode and current flows between the working and the counter electrode. A reference electrode is an electrode that will maintain a stable, known potential, and so the potentiostat can supply the required potential by controlling the voltage difference between the working electrode and reference electrode. This is accomplished by changing the current flow between the working and the counter electrodes. The reference electrode measures the potential at a point in solution between the working and counter electrodes and provides feedback to the potentiostat for it to accurately maintain the desired potential at the working electrode. The processes happening at the surface of the working electrode are of interest in this research, and measuring the current and potential provides information about the mechanism of how a surface process is occurring.

2.1.3 Solution Resistance

As discussed in Sec. 2.1.1, resistance is a measure of how much an object in an electrical circuit opposes the flow of current. The amount which electrolyte impedes the flow of ions is called the solution resistance and must be taken into account when making any electrochemical calculations. When drawing an equivalent circuit for an electrochemical reaction there may be several resistors for different processes; commonly charge transfer resistance and solution resistance. While charge transfer resistance only occurs when there is a Faradaic reaction, solution resistance is present in all electrochemical experiments as current must travel through the electrolyte as

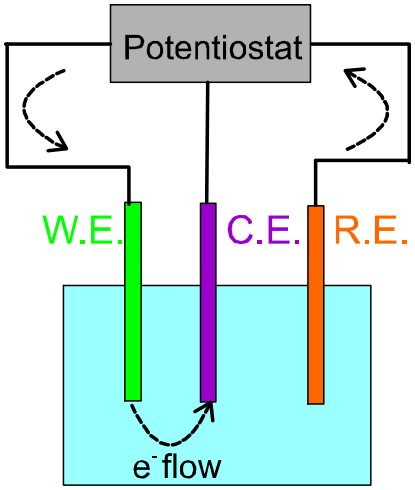

Figure 2.2: Schematic of an electrochemical cell set up. A voltage is applied to the working electrode (WE) and current ‡ows from the working electrode to the counter electrode (CE). The reference electrode (RE) measures the current in the electrolyte at a point between the two and provides feedback to the potentiostat in order for the desired voltage to be constantly applied to the working electrode.

it flows from the working electrode to the counter electrode. In a circuit diagram, solution resistance can be represented by a resistor.

2.1.4 The Electrical Double Layer

One of the fundamental concepts of electrochemistry is the electrical double layer. Whenever a potential difference exists between a conductive surface (often metal) and a solution, charge moves as a result. This takes the form of electrons and positive charges moving towards or away from each other. This creates a wall like structure of ions a few Angstroms thick at all points of the surface which are exposed to the liquid, which is called the double layer. The thickness of the double layer depends on the concentration of ions in the solution, and the speed at which it forms is dependent on the solution conductivity and the dielectric properties of the interface. Both cations and anions still remain free in the solution as the double layer forms. The formation of this wall of charge is referred to as double layer charging. A schematic representation

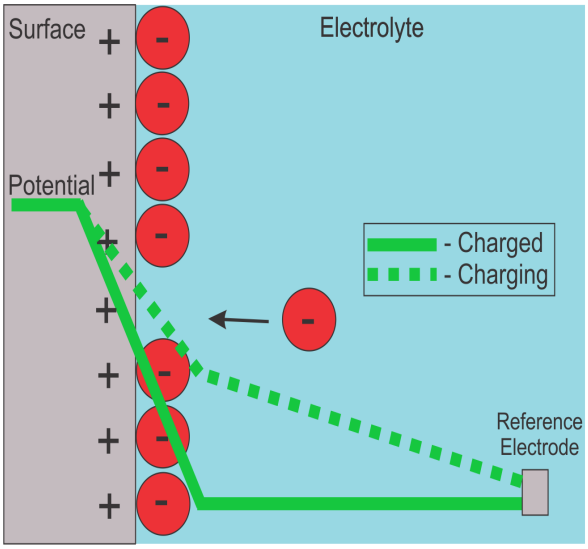

Figure 2.3: Example of how potential drops as it crosses an electrical double layer. The red circles represent anions, and the green line represents potential. This drop in potential on the left across the double layer is the driving force for current across the interface into the solution and the slope changes as the double layer charges. The thickness of the double layer on the surface is on the order of angstroms. The potential drop on the right in the charging case is in the solution between the working and reference electrodes, which is on the order of millimeters. Figure not to scale.

of this is shown in Fig. 2.3.

In the example shown in Fig. 2.3, the potentiostat establishes a potential difference between the working electrode (labelled 'surface' in the Figure) and the reference electrode. This causes a depletion of electrons on the surface which gives the surface a positive charge. Simultaneously, the electric field associated with the potential drop in the solution causes anions from the solution to move toward the electrode surface which forms the wall like double layer on the surface of the metal. The potential drops significantly across the charged interface into the liquid as demonstrated by the green line(s) in Fig. 2.3 and is part of what drives current across the interface between the electrode and the electrolyte. The slope of the potential drop becomes steeper as the double layer charges as shown by the dashed and solid green lines in Fig. 2.3. At first, there are very few ions on the surface of the metal (the double layer is charging) and so the potential drop is smaller across the metal and continues to gradually drop as it

moves out into solution towards the reference electrode. After it is fully charged, the potential drop is steep because it happens at once across the double layer and then levels out as it moves through solution. This phenomena was first noticed in 1853 by Herman von Helmholtz, who went on to show that the interface stores charge like a capacitor. In a circuit diagram, double layer charging is analogous to a capacitor. Roger Parsons also significantly contributed to the understanding of the electrical double layer in the late 1970s and 1980s [52–54].

As previously mentioned the electrical double layer is present on all charged surfaces exposed to an electrolyte, which describes all the electrodes in our experiments. Therefore we must take its effects into account especially when calculating charge. The total current across the interface between an electrode and electrolyte at any time is the sum of all the current due to Faradaic reactions (when there is a charge transfer across the surface/liquid interface) such as oxidation and reduction, and non-Faradaic processes like double layer charging. The current density associated with this process (j_{dl}) will contribute to the charge seen in the experimental data, but because it is not contributing to any Faradaic reactions on the surface it must be corrected for in order to accurately calculate charge associated with only the Faradaic reactions. The equations associated with this process as well as other relevant surface processes will be discussed in further detail in Section 2.3.1.

2.1.5 Cyclic Voltammetry

One type of electrochemical technique used extensively in this research is cyclic voltammetry (CV). In this technique, a specified potential is applied between a working electrode and a reference electrode and the resulting current is recorded. A curve of current versus potential is generated such as in Fig. 2.4, and much of what is happening at the surface of the working electrode can be deduced by analyzing the shape of the recorded curve. The CVs in this research will always plot potential ver-

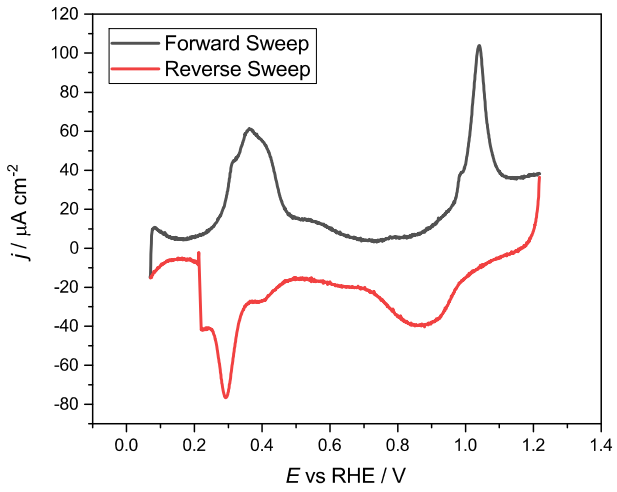

Figure 2.4: Example of a typical Pt(100) CV illustrating the forward and reverse sweeps. The black line indicates the forward sweep and the red line indicates the reverse sweep. The processes occuring in the peaks are discussed in Sec. 2.3.1. Sweep rate 20 mV/s, electrolyte 0.1 M $HClO_4$. This data collected in the cell prior to irradiation. Data collected in preparation for the CH5523 beam time in September 2018.

sus current density (j), which is current normalized to the surface area of the working electrode, and potential will always refer to the potential versus a reversible hydrogen electrode (RHE). The nature of a cyclic voltammogram is that it sweeps through a set of potentials and then reverses back through the same set in a repetitive way. For example, if we set a starting potential at -0.2 V and end potential of 1.5 V, then when conducting a CV the potentiostat would sweep through applying all the potentials between -0.2 V and 1.5 V, and then when it reached 1.5 V, it would turn around and sweep back down to -0.2 V. Moving towards more positive potentials is referred to as a forward sweep, and moving from more positive to less positive or even negative potentials is called a reverse sweep. An example of this is shown in Fig. 2.4, where the part of the CV that is the forward sweep is in black, and the reverse sweep is red. The shape of the curve in the forward and reverse sweeps gives information about what is happening at the surface of the working electrode. An example of this

is discussed extensively in Sec. 2.3.1.

2.1.6 Potential Step and Sweep-Hold Voltammetry

A potentiostat allows the user to conduct other experiments that are similar to cyclic voltammetry but that give different information about the surface. In this research, potential step and sweep-hold techniques were used to probe the surface of the working electrode. Potential step experiments are ones in which a potential is set and held at a specific voltage for a set period of time while the current is recorded, and then the potential is jumped directly to a different voltage without sweeping through all the voltages in between. Often in this research the potential step experiments consist of stepping down to a lower hold potential between each increased step but this isn't necessary; it only depends what sort of data the user is interested in collecting. In this type of experiment it is most interesting to look at a graph of current versus time, as opposed to current versus potential as is generated in a CV. An example of a potential step experiment is shown in Fig. 2.5, where the black line represents potential and the red line represents current, both plotted against time. As seen in Fig. 2.6, which is an expanded version of a single step in Fig. 2.5, there is an exponential decay of the current from the initial value to some steady state. This decay could be the result of a decrease in available sites on the surface of the electrode, for example, and would mean that there are less places at which Faradaic processes could occur which would cause a decrease in current. The current in the step shown also includes current associated with double layer charging, which has a time constant of $R_{\mathrm{s}}C_{\mathrm{dl}}$. The derivation of this time constant and the discussion of its importance is discussed more in Sec. 4.2.2.

Sweep-hold experiments are another type of electrochemical experiment where the potential is held at certain voltages. However in this case, the potential is swept between the two set potentials as in a CV instead of being stepped directly form one

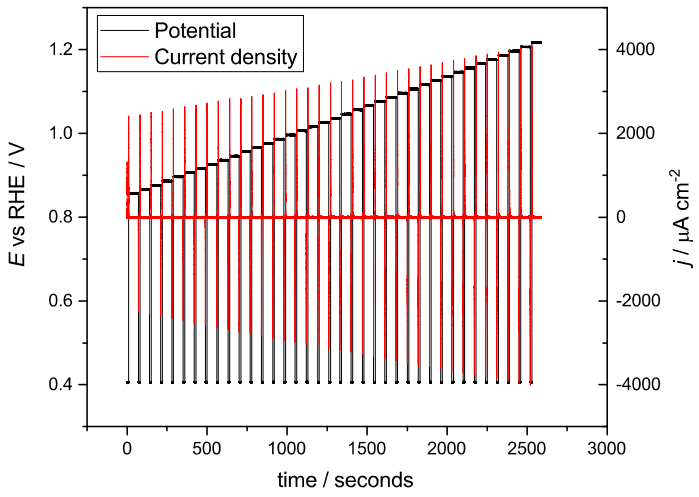

Figure 2.5: Example of a potential step experiment. The black line indicates potential and is plotted against time to illustrate the voltage of each step. The red line is the current density and is also plotted against time. Pt(100) in 0.1 M $HClO_4$ in Ar. The data in this figure is from file 57.mps from the CH4977 beamtime in July 2017 at the ESRF.

to the other as in a potential step experiment. In this research, the potential is also swept down to some lower starting potential between each hold which then creates what looks like a series of CVs to various potentials. An example of this sort of technique is shown in Fig. 2.7.

2.2 Introduction to Surface Chemistry

In this section, a brief overview of surface chemistry will be given. Specifically the different types of cubic crystal, the classification of a crystal plane, and the primitive unit cell for three different platinum surfaces will be introduced. The section will also briefly explain reciprocal space and explore the concept of coverage.

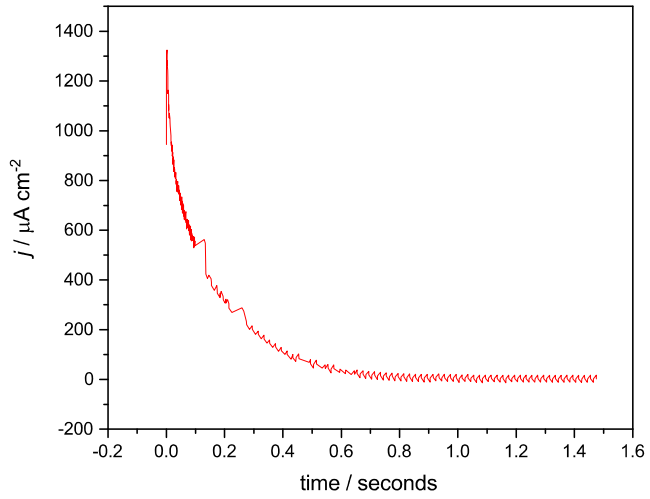

Figure 2.6: Example of step current decaying exponentially over time. It can be seen that the current has decayed to zero after a few seconds, and so only the first 1.5 seconds of the total 60 have been shown for clarity. Pt(100) in 0.1 M $HClO_4$ in Ar. The data in this figure is from file 57.mps from the CH4497 beamtime in July 2017 at the ESRF.

2.2.1 Platinum Crystal Surfaces

For many crystalline materials, the unit cell of the material can be modeled as a cube which encompasses between one and four atoms. Depending on the material of the crystal, the placement of the atoms within the cube varies. Three possibilities of cubic unit cells are shown in Fig. 2.8. The primitive cubic crystal contains $\frac{1}{8}$ of each of the eight corner atoms, equating to one full atom in the simple cubic unit cell. The body centered cubic (BCC) unit cell includes $\frac{1}{8}$ of each of the eight corner atoms plus one full atom in the middle, for a sum of two full atoms per cubic unit cell. Iron and tungsten are examples of BCC crystals. Platinum has a face centered cubic (FCC) crystalline structure, which contains $\frac{1}{8}$ of each of the eight corner atoms plus $\frac{1}{2}$ of each of the six atoms on the faces of the cube equating to four atoms per cubic unit cell. The conventional FCC unit cell is used rather than the primitive unit

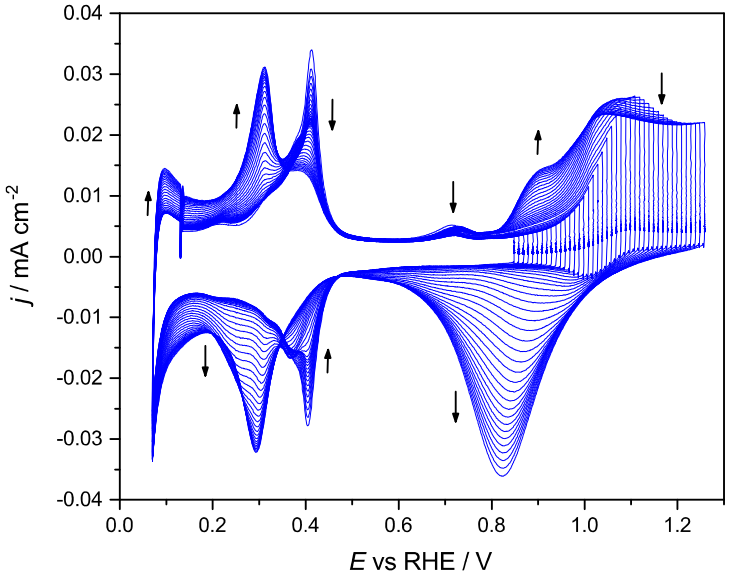

Figure 2.7: Example of a series of sweep-hold experiments. Pt(100) in 0.1 M H_2SO_4 in Ar, sweep rate 20 mV/s. The data in this figure is from file 15.mps from the CH5523 beam time in September 2018 at the ESRF.

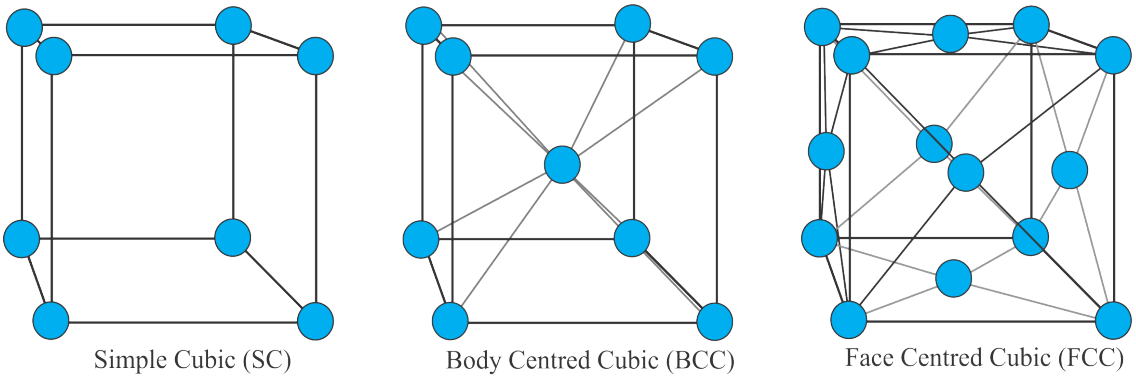

Figure 2.8: Example of three types of cubic unit cells; the Simple Cubic (SC), the Body Centered Cubic (BCC), and the Face Centered Cubic (FCC). Platinum is a FCC crystal.

cell (the one that contains just one atom) because it has more symmetry.

It is helpful to label the three dimensional directions of the cubic unit cell as the $a,\ b,$ and c directions from some chosen origin atom. Then if we cut through the cubic unit cell at various angles, we can create surfaces that are oriented along crystalline planes. Many different crystalline planes of the same elemental crystal can be achieved depending on the orientation of the newly constructed surface along the $a,\ b,$ and c directions of the cubic unit cell. In order to classify a crystal plane, it is assigned a set of three numbers to it in the form of (h, k, l). The variables $h,\ k$ and l are known as the Miller indices, and (h, k, l) describes a plane based on where that plane intersects $a,\ b,$ and c in units of lattice parameters. For example, if we were to intersect the platinum cubic unit cell lattice at the end of the $a,\ b,$ and c vectors from the origin atom (which we've chosen as the atom in the bottom layer back corner of the cubic unit cell outlined in black) we would create the rainbow triangular plane seen inside the FCC unit cell shown in Fig. 2.9. That plane can be seen to intersect the crystal lattice at a distance of one lattice parameter in the $a,\ b,$ and c directions from the origin atom ($a = 1,\ b = 1,$ and $c = 1$). We would then take the reciprocal of these numbers to get (h, k, l) and we would call this the $(1, 1, 1)$ plane. A platinum surface oriented along this plane would be called Pt(111). Similarly if we draw a

plane from the same origin atom that intersects a at 1 but is parallel to b and c, as in Fig. 2.10, we would create the rainbow square plane seen in that figure. A crystal surface oriented along this plane would have (h, k, l) coordinates of $(\frac{1}{1}, \frac{1}{\infty}, \frac{1}{\infty})$, which is to say it is the $(1, 0, 0)$ surface. Note that this would be an equivalent surface if it was oriented along the plane that is parallel to a and c, and intersected b at 1, or if it was oriented along one that is parallel to a and b, and intersected c at 1. To avoid confusion, we'll refer to this as the Pt(100) surface as opposed to Pt(010) or Pt(001) for the remainder of this text. Finally if we draw a plane that intersects at $a = 1$, $b = 1$, and is parallel to c as is the blue rectangle in Fig. 2.11, then we would create the $(1, 1, 0)$ plane, and all surfaces equivalent to it would be called Pt(110). Of course we could also refer to this surface as Pt(101) or Pt(011), but for the remainder of this text we will denote it as Pt(110). There are more surfaces that could additionally be drawn on the platinum crystal (a at 1, b at $\frac{1}{2}$, and c at $\frac{1}{2}$, for example which is the $(1, 2, 2)$ plane) but for this research we are only concerned with the three low index planes discussed.

The primitive surface unit cell, or the smallest repeatable parallelogram that can be drawn in the plane, can then be determined for each of the unique surfaces. In Figs. 2.9 - 2.11, these were outlined in red. For Pt(111), it can be seen that this shape is a rhombus. For Pt(100) and Pt(110) the primitive unit cells have the shape of a square and a rectangle, respectively. In the case of these three examples, each parallelogram contains one full atom.

The Reciprocal Lattice

A system of identifying these planes in reciprocal space, otherwise known as k-space, can also be defined. Reciprocal space is a set of imaginary points whose vectors from the origin are normal to the planes in real space. Knowing how the reciprocal and real lattices are connected mathematically allows for the interpretation of the results of X-ray scattering experiments in order to understand what is happening on the

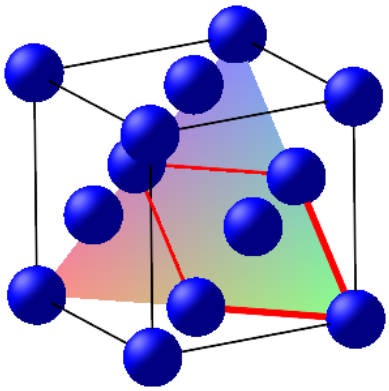

Figure 2.9: Schematic example of the Pt(111) plane (rainbow triangle) in the cubic unit cell. This plane intersects the cubic unit cell at $a = 1$, $b = 1$, and $c = 1$ from the origin atom which has been chosen as the atom in the back corner of the bottom layer. The shape of the simple surface unit cell outlined in red is a rhombus.

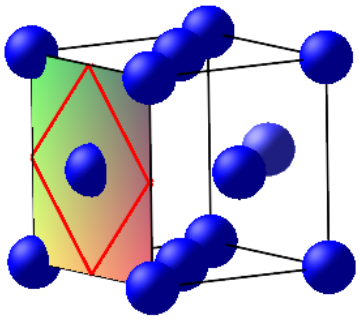

Figure 2.10: Schematic example of the Pt(100) plane (rainbow square) in the cubic unit cell. This plane intersects the cubic unit cell at $a = 1$ from the origin atom which has been chosen as the atom in the back right corner of the bottom layer, and is parallel to b and c. The shape of the simple surface unit cell outlined in red is a square.

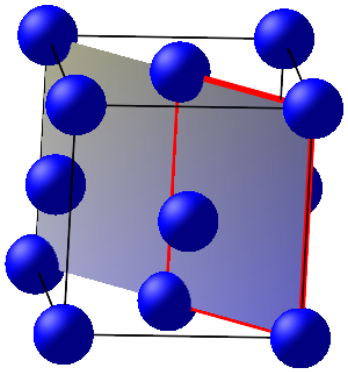

Figure 2.11: Schematic example of the Pt(110) plane (rainbow rectangle) in the cubic unit cell. This plane intersects the cubic unit cell at $a = 1$ and $b = 1$ from the origin atom which has been chosen as the atom in the back right corner of the bottom layer, and is parallel to c. The shape of the simple surface unit cell outlined in red is rectangular.

crystal surface in real space, as will be discussed further on.

2.2.2 Coverage

In the field of surface science, it is often interesting to discuss the amount or coverage of some adsorbed species on a surface. The coverage, denoted as θ, is the ratio of the total adsorbed atoms to the total surface atoms. Fig. 2.12 shows an example looking down on a surface unit cell (outlined in black). Inside this unit cell it can be seen that there are two full blue circles ($\frac{1}{4}$ of each of the four corner circles plus one in the middle) which represent atoms belonging to the crystal, and one red circle on top of the center blue circle, which represents an adsorbed species. The ratio of adsorbed species for this surface unit cell is 1 red atom to 2 total blue atoms, or a coverage of $\frac{1}{2}$. Although the coverage is strictly unitless, it is sometimes given the unit of ML, meaning monolayers. In the example of Fig. 2.12, there is 0.5 monolayer of

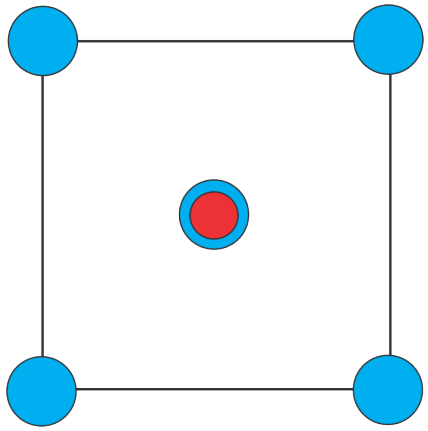

Figure 2.12: An example of how coverage (θ) is determined for a surface unit cell. This is the view looking down on a surface unit cell. The blue atoms represent the atoms of the crystal, and the red atom adsorbed onto the middle blue atom represents some adsorbed species. In this example, there is a ratio of 1 adsorbed atom (red) to 2 crystal atoms (blue) and so the coverage here would be $\frac{1}{2}$.

red atoms adsorbed. Additionally we will use θ_e to express the number of electrons passed through the interface per surface atom in units of monolayers. The calculation of this value will be explained in detail in Sec. 3.2.4.

2.3 A Brief History of Platinum Electrochemistry

This research is centered on the reactions and processes happening at the surface of platinum electrodes. Platinum is a remarkably good catalyst and a valued component of fuel cells because it is the most active elemental metal for the hydrogen and oxygen evolution and reduction reactions [8,29]. Though it is one of the most studied interfaces, there is still much unknown about how platinum oxidation and reduction happens on the atomic level [40]. The fundamental research of kinetics and growth mechanisms of platinum oxide are an important component to understanding how to preserve catalytic reactivity of platinum when used in fuel cells and electrolyzers. The majority of the understanding of the surface oxidation of platinum up to this point are exemplified in a 2011 review paper [33], which focuses on the electrochemical work

of researchers such as Jean Clavilier, Brian Conway, and Gregory Jerkiewicz on single crystal platinum and bead crystals. In combination with other techniques such as ultrahigh vacuum (UHV), low energy electron diffraction (LEED) and Auger electron spectroscopy (AES), Conway et al found that platinum oxide ultimately grows as a multilayer film with what is thought to be an OH adsorption step followed by a place exchange process to form platinum oxide [55,56]. This place exchange process will be discussed in further detail in Sec. 2.3.2.

Some work has been done specifically on the kinetics of the oxide formation. For polycrystalline platinum, the potential step charge is a direct logarithmic function of time, which means it is linear vs ln(time) [55–58]. There were some earlier studies that attributed this to the multilayer film, but Conway et al modelled it as time dependent surface dipole moment changes [55,59], where the dipoles were the Pt and O atoms in the place exchange process.

On single crystal platinum, the charge is again found to be linear vs ln(time) [60]. There are also noticeable differences in reactivity between the three low-index platinum surfaces; Pt(111), Pt(100), and Pt(110) [59,61,62]. However, this data was collected on well cycled surfaces and so the kinetics found are not for the initial stages of oxide formation on well ordered surfaces. Work by Gomez-Marin et al and Feliu et al on well-defined single crystals found that the initial formation of oxide is a two step process. The oxide formation begins with the dissociation of water followed by OH adsorption After OH adsorption, they report sequential adsorption of various species to form PtO(ads) via a nucleation-growth mechanism [63–65]. The oxide is formed from this adsorbed PtO to a maximum coverage of 2 ML [13,59]. Additionally, Rinaldo et al proposed a kinetic mechanism involving an adsorbed peroxo species that explained the shape of the oxide peak [11]. Such peroxo species have been observed by Raman studies [66]

Some work has also been done to observe place exchange in synchrotron studies on platinum nanoparticles and logarithmic growth has been reported [67]. Our group

also reported preliminary step experiments that showed logarithmic growth of place exchange coverage on Pt(111) [68]. This thesis uses a combination of electrochemical experiments and X-ray data to further investigate the kinetics of oxide formation on an atomic scale. This combination can be used to calculate the number of electrons that are required per place exchange platinum atom during the initial formation of the oxide on a well ordered surface which leads to finding a mechanism for the process.

Electrochemical experiments are very sensitive to any surface or solution impurities because adsorption of any contaminant molecules on the surface can cause a charge transfer reaction that reflects what is happening to the contaminant but not necessarily the surface of interest. This poses a problem for electrochemists, as it is near impossible to conduct an experiment without contamination of the electrode surface when it's exposed to air, which can contain any number of organic contaminants. Organic impurities can disrupt the reaction being studied by acting as a barrier to the desired surface atoms. Up until 1980, all of the electrochemical data published for single crystal platinum surfaces with atomic level purity was subject to this uncertainty. The electrochemical community had mostly come to a consensus on what they believed to be the correct cyclic voltammogram (CV) for many platinum surfaces [33]. However, with the discovery of flame annealing in a pivotal paper by Clavilier et al, this view changed [36]. Clavilier was able to achieve a higher quality of annealing by harnessing the high catalytic ability of platinum to rid the surface of organic impurities at high temperatures. This discovery allowed Clavilier to clean the surface to a degree that had never before been achieved. The CVs that were produced after preparing the surface of the electrodes in this way showed sharper peaks and, in the case of Pt(111), some never before seen peaks [69–71]. Most convincing for these new CVs, was that the charges calculated were associated with a ratio of one to one between hydrogen and surface platinum atoms. After characterization of the surface though other techniques such as UHV, LEED, and AES and verification of similar charges and coverages, it was concluded that a CV of a properly cleaned electrode

could be used to confidently characterize platinum surfaces and the reactions happening at various potentials [33, 72–74]. In this research, annealing is done under inert atmosphere, and then a drop of water purified using Millipore (18 MΩ cm) is placed onto the surface to protect it from organic pollutants. In this research, we make use of CV to gather quantitative information about the surface of our working electrode.

2.3.1 Assignment of the peaks of Pt(111), Pt(110), and Pt(100) CVs

In this section we will discuss peak analysis on cyclic voltammograms of Pt(111), Pt(110), and Pt(100). Understanding which reactions are taking place at the working electrode (one of the three platinum surfaces) at each of the features on each CV will help us assign certain surface processes to them. This will then further enable us to make calculations in respect to oxidation, reduction, and other interesting surface processes. Figs. 2.13, 2.14 and 2.15 show CVs in 0.1 M $HClO_4$ of Pt(111), Pt(100), and Pt(110), respectively. In each of these Figures, parts of the CV have been color coded to show areas of different features and make it easier to discuss them and assign the reaction(s) that cause each to appear.

We'll start by reviewing the Pt(111) CV, which is shown in Fig. 2.13. The black portion in this figure the hydrogen underpotential deposition (HUPD) area and is achieved with a one to one coverage of hydrogen to surface platinum [33, 36, 75–78]. The reversible surface process taking place in the HUPD region is as follows:

$$\mathrm{PtH(ads)} \rightleftharpoons \mathrm{Pt} + \mathrm{H^+ + e^-} \tag{2.4}$$

where the positive half of the sweep represents the forward reaction, and the negative half represents the reverse. If we were to sweep down to more negative potentials than shown in Fig. 2.13, the current density would become large and negative. This indi-

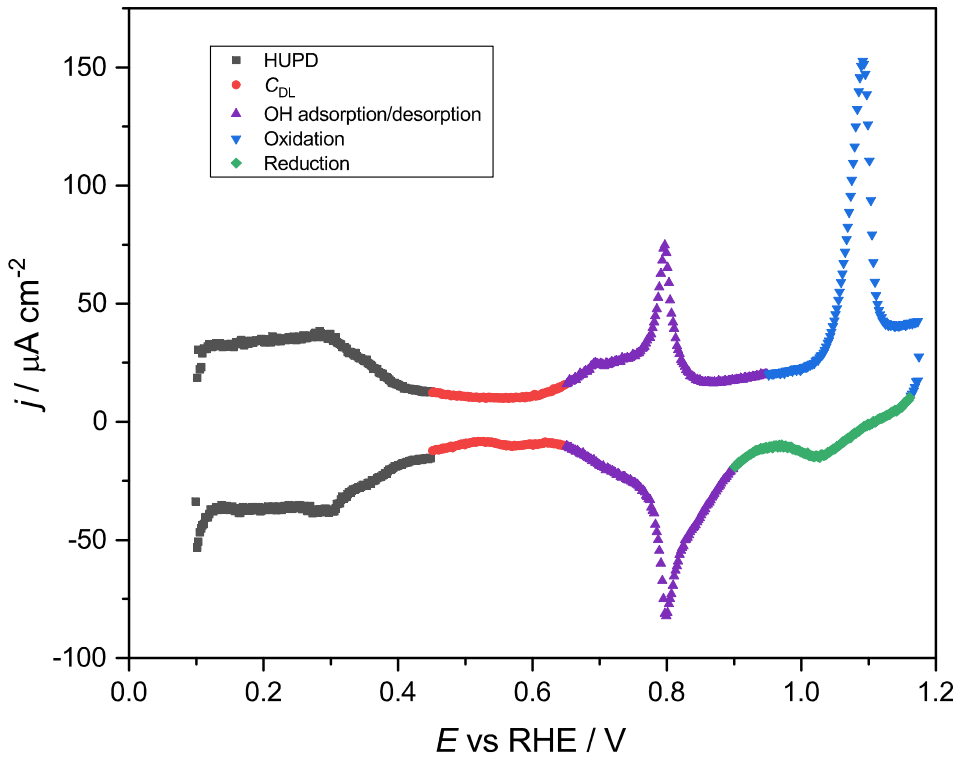

Figure 2.13: Cyclic voltammogram of Pt(111) in 0.1 M $HClO_4$. Sweep rate 50 mV/s. Parts of the CV are color coded to show the areas of different features and explain the reactions that cause them. In this figure, the portion in black is HUPD, the red is double layer charging, the purple is the formation of adsorbed hydroxide, the blue is platinum oxidation, and the green is platinum oxide reduction. Data collected in preparation for the CH5523 beam time in September 2018.

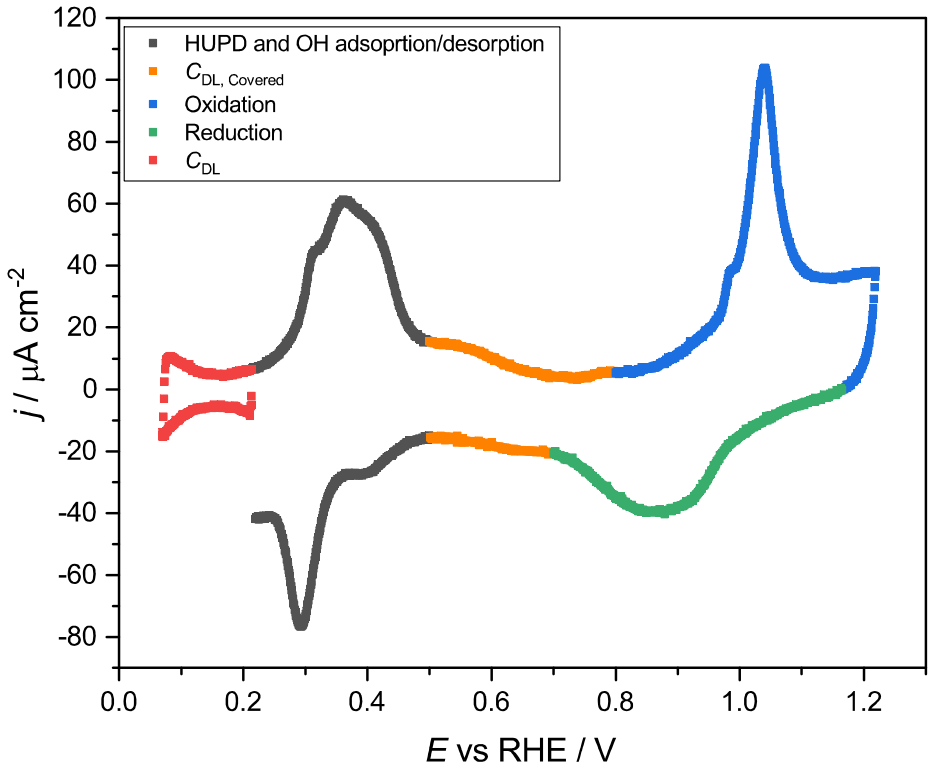

Figure 2.14: Cyclic voltammogram of Pt(100) in 0.1 M $HClO_4$. Sweep rate 50 mV/s. Parts of the CV are color coded to show the areas of different features and explain the reactions that cause them. In this figure, the portion in red is the double layer charging region, the black is HUPD and OH adsorption/desorption, the orange is double layer charging on a covered surface (or peak broadening), the blue is platinum oxidation, and the green is platinum oxide reduction. Data collected in preparation for the CH5523 beam time in September 2018.

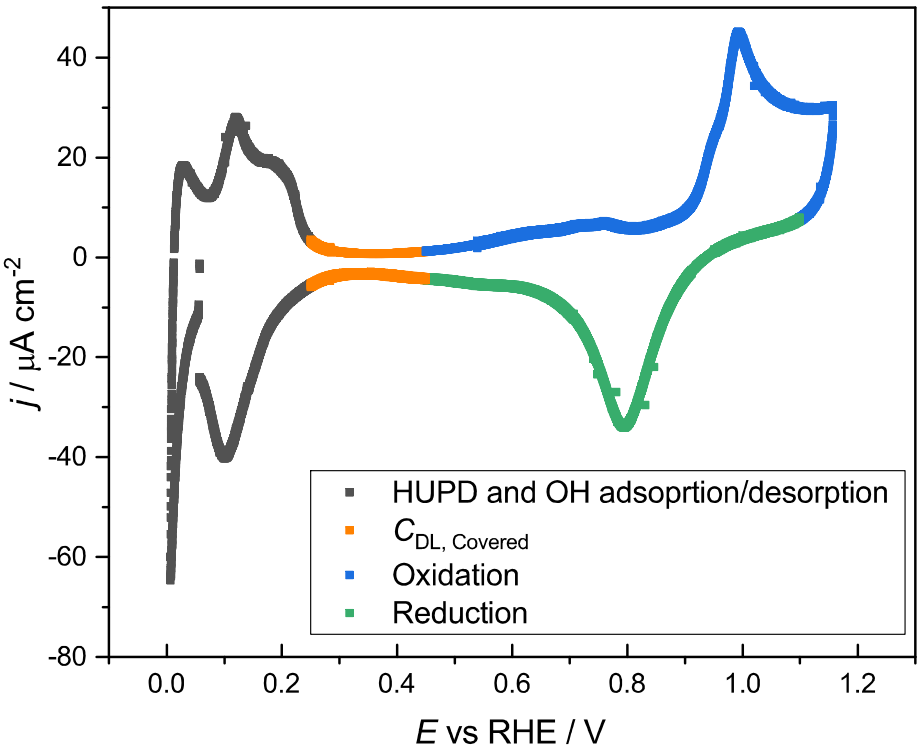

Figure 2.15: Cyclic voltammogram of Pt(110) in 0.1 M $HClO_4$. Sweep rate 50 mV/s. Parts of the CV are color coded to show the areas of different features and explain the reactions that cause them. In this figure, the portion in black is HUPD and OH adsorption/desorption, the red is double layer charging, the blue is platinum oxidation, and the green is platinum oxide reduction. This data collected during the December 2019 beamtime at DESY. EC file 27, cycle 15 (the first cycle to 1.2 V).

cates that the hydrogen evolution reaction (HER), where two H^+ ions are converted to hydrogen gas as shown in Eq.2.5, is occurring [52, 79, 80].

$$2H^+ + 2e^- \rightarrow H_2(g) \tag{2.5}$$

The next section of the Pt(111) CV is colored red, which is where double layer capacitance charging and discharging occurs. As discussed in Section 2.1.4 no Faradaic reactions occur here, but the equation that is assigned to this region is that of a capacitor that is independent of potential, as follows:

$$j_{\mathrm{dl}} = C_{\mathrm{dl}} v \tag{2.6}$$

where j_{dl} is the current density of the double layer region, C_{dl} is the capacitance of that region, and v is the sweep rate.

The next region of interest on the Pt(111) CV is known as the "butterfly peaks", which are outlined in Fig. 2.13 in purple. Before the evolution of flame annealing and electrolyte purification, these peaks were not seen on Pt(111) CVs. The first published result that included these peaks was in 1980 by Clavilier [36] and was considered to be the first true Pt(111) CV. They were reproduced quickly in various laboratories across the world verifying their presence and correspond to about 0.5 ML, with about 0.3 ML due to OH adsorption and 0.2 ML due to specific anion adsorption. [71, 77, 78]. After some years of debate in the electrochemistry community as to what causes these peaks, they have been attributed to the formation/dissociation of adsorbed hydroxide when the reaction occurs in perchloric acid (as they are in these CVs), and the adsorption and desorption of bisulfate ions when in sulfuric acid [76, 81]. The formation of adsorbed hydroxide is as follows, where Pt here indicates a free adsorption site on the surface of the working electrode:

$$H_2O + Pt \rightleftharpoons PtOH(ads) + H^+ + e^- \tag{2.7}$$

The peaks consist of two parts: the sharp peaks that occur at about 0.80 V and the broad region that leads to them starting at about 0.65 V. The broad portion is attributed to OH adsorption/desorption and the sharp peaks are associated with a phase transition [82–84].The adsorbed OH and water at the interface are believed to be in a hydrogen-bonded surface layer that extends over many Pt atoms [85]. The sharp peak is easily disrupted by steps or other types of defects on the surface, and a sharper peak indicates a better ordered surface.

As potential becomes more positive after the butterfly peaks, the next region of interest occurs. The blue portion the Pt(111) CV in Fig. 2.13 is the peak related to the formation of oxide [31,76–78]. As previously mentioned, this process is quite complicated and involves a series of adsorbed species, but the reaction is most commonly simplified as follows:

$$\mathrm{PtOH(ads)} \rightleftarrows \mathrm{PtO(ads)} + \mathrm{H^+} + \mathrm{e^-} \tag{2.8}$$

This peak has a coverage of about 0.3 ML [86–88]. The stability of the voltammogram when cycling to 1.1 V was assumed to be evidence that the peaks up to that potential involve only adsorption and not surface reconstruction. However, in 1994 You et. al. used X-ray diffraction to show that place exchange is happening at these potentials [89, 90]. This was confirmed again through use of X-ray diffraction by our group in 2017 [68]. One way to rationalize many of these observations is that the reaction in Eq. 2.8 occurs with the exception that PtO(ads) is instead a place exchanged PtO [91].

If we were to continue to sweep to more positive potentials beyond the oxidation peak we would see the onset of the oxygen evolution reaction (OER), where water from the electrolyte is converted to oxygen gas as follows:

$$2\mathrm{H_2O} \rightarrow 4\mathrm{H^+} + 4\mathrm{e^-} + \mathrm{O_2(g)} \tag{2.9}$$

The experiments in this thesis use CVs that are never swept to those higher potentials in order to avoid oxygen evolution, and thus the feature for that process is never visible in our experimental data.

Finally, the green region of the Pt(111) CV in Fig. 2.13 illustrates the oxide reduction reaction [37, 76–78]. This reaction is just simply the reverse of Eq. 2.8 and Eq. 2.7 where oxidized platinum is reduced back to elemental platinum and water is formed.

The Pt(100) and Pt(110) voltammograms differ from the Pt(111) voltammogram in a few ways. Firstly, the portion of the Pt(111) CV highlighted in black corresponds to just the HUPD region. For the Pt(100) and Pt(110) CVs shown in Figs. 2.14 and 2.15, the portion in black is a mix of HUPD (Eq. 2.4) and OH adsorption/desorption (Eq. 2.7) [33, 92]. This then leads to a double layer region on Pt(110) that covered by OH molecules, shown in orange in Fig. 2.15. Secondly, on Pt(111) the double layer region is well defined, but it can be seen that on Pt(100) there appear to be two sections that could correspond to double layer capacitance charging. These two regions are colored in red and orange in Fig. 2.14. It's most widely accepted that the region that has been highlighted in red corresponds to true double layer charging for Pt(100) and the orange region is some partially covered surface or peak broadening from both the HUPD and oxidation regions that cause it to not be truly flat as it is for Pt(111) in the same potential range [33]. Additionally it should be noted that although the oxide peak looks similar on Pt(100), the place exchange structure and reactivity are quite different [93]. Finally, the butterfly peak seen on Pt(111) is not seen on Pt(100) or Pt(110) because the surface symmetry is different and the atom spacing on Pt(100) and Pt(110) is not optimum for the OH-water surface layer. The adsorbed OH is more mobile on these surfaces, and so the butterfly-shaped peak is not seen [85].

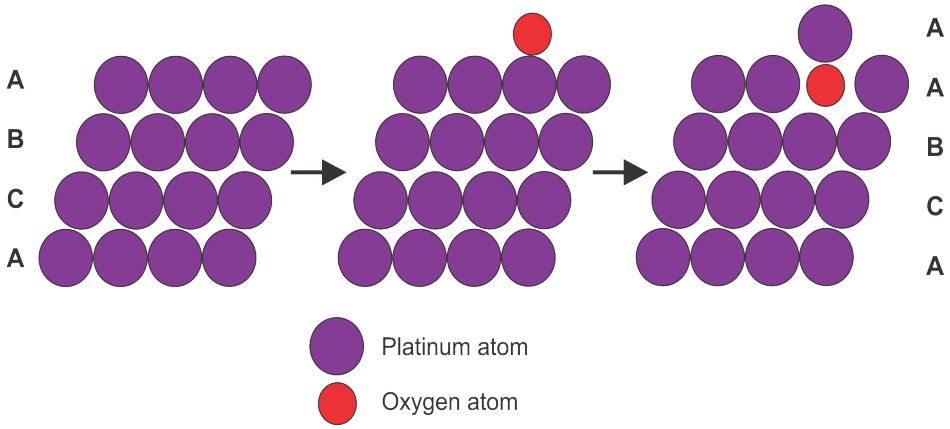

Figure 2.16: Schematic of how place exchange occurs on the surface. The image is a cross section view of the platinum crystal with the surface layer (A) at the top. The purple atoms represent the platinum atoms, and the red represent oxygen.

2.3.2 Oxide Formation

Oxide formation and growth on the platinum surface is interesting to study, especially in relationship to fuel cells and other catalytic reactions. Growth of an oxide layer on fuel cell catalysts can cause the fuel cell to behave differently than expected or intended. Understanding how the oxide forms on an atomic level could help unlock ways to create better mechanisms for preserving the catalyst for increased durability of these fuel cells. One mechanism for oxide formation on polycrystalline platinum known as "place exchange" was first proposed in the 1960s, and is still thought to be the best model for oxide formation [29, 56, 94]. In this process, a surface platinum switches places with the oxygen adsorbed to it. The oxygen atom goes into the crystal lattice and the platinum "pops up" out of its lattice site causing oxide growth. Previous work in this group has found that once out of the lattice, the place exchanged platinum atom moves about 2 Å above its original lattice site [68], and is surrounded and stabilized by three adsorbed oxygen atoms [93]. A schematic of the place exchange process is shown in Fig. 2.16.

On the left side of the figure, undisturbed polycrystalline platinum obeys the ABC stacking pattern of FCC crystals. This means that every third layer there is

a repeated layer in which the atoms will be directly above/below the atoms in the original layer, as seen in the drawing. The middle drawing of Fig. 2.16, an oxygen atom (red) is adsorbed to a surface platinum atom. Finally on the right side of Fig. 2.16, the place exchange step of this mechanism happens when the platinum atom switches places with the adsorbed oxygen. The platinum atom pops up out of its lattice spot and goes directly above the spot in the lattice where it formerly resided. In Fig. 2.16, the place exchanged platinum atom was an "A" layer atom. For this lattice to maintain its ABC stacking pattern, the layer above the "A" layer should be a "C" layer, but the place exchanged platinum atom maintains an "A" layer position. This disordered platinum atom stacking is important because when this new surface is struck with an X-ray beam, it will have a lesser X-ray intensity than that of the perfectly ordered surface. This decrease in intensity can be monitored in surface X-ray diffraction experiments, which will be discussed further in Sec. 3.3, and allows for the tracking of the oxidation of platinum surface atoms in real time.

Chapter 3

Experimental Techniques

In this chapter, the various experimental techniques will be described. First the electrochemical techniques and setup will be addressed and a sample calculation of the charge density for one monolayer, σ_{ml} will be shown. Next, the X-ray techniques will be explained and some calculations for real and reciprocal space lattice vectors will explained. Finally, the concepts of Bragg angles and crystal truncation rods will be explored.

3.1 Electrochemical Techniques

This research employed a variety of electrochemical techniques to probe platinum oxidation mechanisms. As previously mentioned, cyclic voltammetry, potential step experiments, and sweep-hold experiments were used to electrochemically study the oxidation of the working electrode (single crystal platinum metal). This next section will discuss the specifics of the electrochemical setup and techniques for the beam times in July 2017, March 2018, September 2018, and December 2019 for which the author was present.

3.1.1 Working Electrode Annealing

Although the flame annealing technique designed by Clavilier [36] is the standard for annealing smaller crystals, the heating is too localized and the cooling is too uncontrolled for larger crystals which leads to stress that is not suitable for this work. Therefore, due to the size and shape of the crystal used in these experiments as well as the safety procedures at the European Synchrotron Radiation Facility (ESRF) and Deutsches Elektronen-Synchrotron (DESY), a different method of annealing using an induction furnace was used instead. Use of an induction furnace is standard for annealing larger single crystals, and was used to heat our platinum crystals to temperatures similar to those that would be expected in flame annealing procedures. This annealing with induction furnace heating was done in an inert environment. The crystals were then cooled slowly in various different inert gases. A mixture of 98% Argon mixed with 2% Carbon Monoxide was used for Pt(111) and Pt(100) surfaces, and in 100% Carbon Monoxide for Pt(110) as recommended in the literature [95–97]. Early Pt(111) experiments done by this group were cooled in pure Argon or pure Nitrogen, as is also acceptable [98,99]. Figure 3.1 shows a photograph of one of many iterations of this annealing setup with commentary about the orange glowing color of the platinum crystal at high temperatures. This specific setup was used at DESY in December of 2019. A thermocouple was used to monitor the approximate surface temperature of the crystal electrode as can be seen in the bottom left of Fig. 3.1.

3.1.2 Electrochemical Cell Setup

In this experiment, a hanging meniscus cell design was used in order to perform electrochemical experiments while maintaining the ability to simultaneously collect X-ray data. Traditional electrochemical cells fully encase the working electrode and don't allow for an X-ray beam to access the surface of the electrode undisturbed, and thus we implemented the hanging meniscus cell design. Fig. 3.2 shows a schematic

Figure 3.1: Image of the annealing setup at DESY 2019 with commentary about the color of platinum at the temperature shown. Here the coil of the induction furnace can be seen wrapped around quartz tubing in which the platinum crystal is encased. 100% CO gas is being flowed around the crystal, and the temperature is being roughly monitored by a digital thermometer attached to the quartz that is holding the crystal.

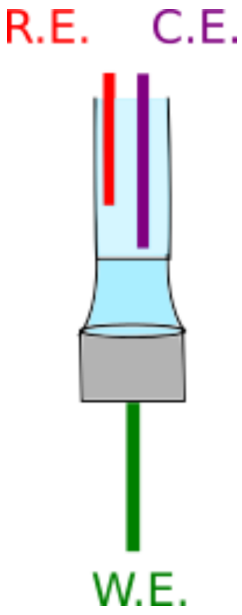

Figure 3.2: Schematic of the electrochemical set up of the hanging meniscus cell. The red line represents the reference electrode, and the purple line represents the counter electrode. Both of these are inside a glass tube which is suspended above the crystal surface. From the tube hangs the electrolyte meniscus, which is enlarged until it wets just the surface of the crystal, thus creating our hanging meniscus cell.

of the electrochemical setup of this hanging meniscus cell. The working electrode, a single crystal manufactured by Surface Preparation Laboratory with a circular face and diameter of 7 mm of Pt(100), Pt(111), or Pt(110) (shown in Fig. 3.3), was mounted into the bottom of this cell setup and connected to the potentiostat at the base of the crystal through contact with a platinum wire (shown in green in Fig. 3.2). The crystal itself is top hat shaped with a larger, flat brim at the bottom and the surface of interest at the top. It was held securely in the cell by a threaded Teflon ring which wrapped around the bottom "brim" of the crystal. Suspended above the surface of the working electrode in a glass tube were the reference (Ag/AgCl) and counter electrodes. The electrolyte, either 0.1 M $HClO_4$ or 0.1 M H_2SO_4, was then pumped through the glass tube containing the reference and counter electrode with a stepping motor pump system to form a hanging meniscus. The meniscus was enlarged just until it wet the entire top face of the crystal, as seen in the schematic.

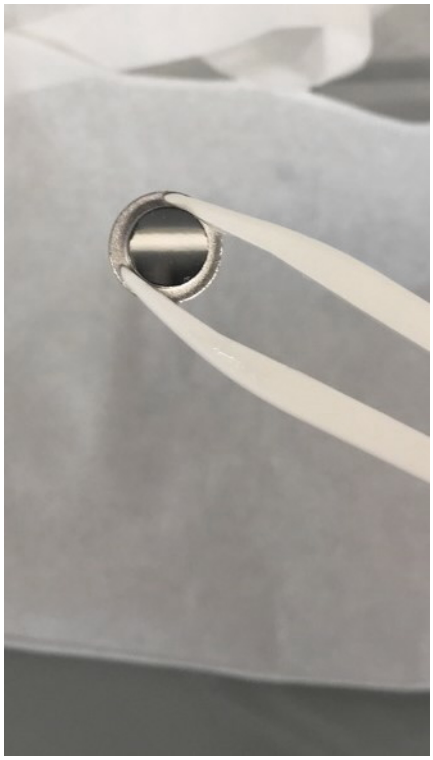

Figure 3.3: Photograph of one of our platinum single crystals held with teflon tweezers. From this top view, it is easy to see how the crystal is "top hat" shaped, and has a brim. In this photo, the tweezers squeeze the sides of the crystal to hold it securely in the air. The single crystal pictured here is one of several used as the working electrode in these experiments. The crystals used in all the experiments in this research have a diameter of 7 mm.

Over enlargement of the meniscus can cause it to fall from the top of the crystal and wet the sides. This doesn't effect the X-ray measurements, but it invalidates any electrochemical measurements so ensuring this proper set up before making any electrochemical measurements was crucial. The entire cell was encased in a Kapton film in order to maintain an oxygen-free atmosphere, which was accomplished by purging the cell with argon gas. Fig. 3.4 shows a picture of this setup including the encased cell mounted to a goniometer, which was used for the alignment of the crystal into the path of the X-ray. The details of the X-ray setup is detailed in Sec. 3.3.

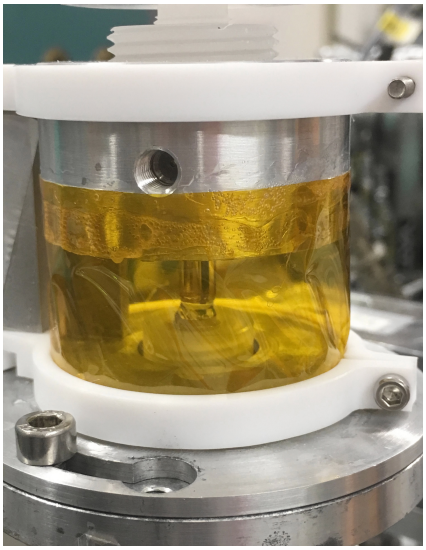

Figure 3.4: Photograph of the hanging meniscus cell used in the experimental setup. The crystal and electrolyte meniscus are encased in a Kapton film in order to flow argon gas around the working electrode to keep the reaction oxygen free. The base of the crystal is held secure in the cell by a teflon ring. It can be seen that the hanging meniscus is enlarged just so that the surface of the crystal is wet, but it has not spilled over and caused the sides to become wet.

3.2 Electrochemical Experiments

This section will cover many of the calculations needed to interpret the electrochemical data collected at the ESRF and DESY facilities. Normalizing current to electrode surface area, reference electrode potential conversion from Ag/AgCl to RHE, calculations of the expected solution resistance and monolayer value calculations will be shown. Use of these calculations will then be implemented into the data analysis in Chapter 4.

3.2.1 Normalizing to Electrode Surface Area

It's easy to see how many things in this research are proportional to the surface area of the working electrode; more surface area means more surface atoms which leads to a greater amount of surface reactions. In order to easily compare the results of this

work to literature values, everything was first normalized to the surface area of our single crystal electrodes. The single crystals used in this research all had a circular face that was 7 mm in diameter. The total area of this electrode, A, is then calculated in Eq. 3.1.

$$A = 0.35^2 \times \pi = 0.38485 \text{ cm}^2 \tag{3.1}$$

Thus the total surface area of the working electrode is found to be 0.38485 cm^2. Raw potentiostatic data is normally collected as current, and can be converted to current density (j) as is shown in the Figures in this paper by dividing the current by the area of the working electrode. If the raw data is first converted from current to current density before beginning other calculations, then the surface area will have been accounted for and all our numbers will be normalized to a per area number, thus making comparison between various surfaces easier.

3.2.2 Potential Conversion

The data in this thesis was collected using a Ag/AgCl reference electrode, but the potential has been converted to V vs RHE in every figure for clarity. To convert from one to the other, the formula shown in Eq. 3.2 was used, where $E^{\circ}_{\text{Ag/AgCl}}$ is 0.1976 V at the temperature at which the experiments were conducted, and $E_{\text{Ag/AgCl}}$ is the raw data potential. All of the electrolytes used in this work have a pH near enough to 1, and so the potential was converted from Ag/AgCl to RHE by adding 0.2566 V to the raw data potential.

$$E_{\text{RHE}} = E_{\text{Ag/AgCl}} + (0.059)\text{pH} + E^{\circ}_{\text{Ag/AgCl}} \tag{3.2}$$

This research consisted of conducting a variety of CVs, potential step, and sweep-hold experiments through the oxidation regions of each surface. Each of these exper-

iments were performed between a low potential of about 0.05 V and upper potential maximum of about 1.5 V. As discussed in Sec. 2.3.1, oxygen evolution begins to occur at potentials above about 1.5 V and hydrogen evolution happens around 0 V. For this reason, CVs were mostly kept between these potentials. Potential step and sweep-hold experiments, generally had upper potentials between 0.8 V and 1.4 V, and stepped back to potentials around either 0.05 V or 0.4 V to probe the different effects of stepping from both the UPD and double layer regions and to find the threshold of place exchange reversibility, which is where the surface transitions from reversible to irreversible behavior. This was done simultaneously with SXRD in order to probe the structure of the crystal surface at various potentials. Upon contact with the meniscus, we held the potential of the working electrode at a suitable potential in the HUPD regime for the specific surface, usually about 0.4 V, while aligning the sample with the X-ray beam. After alignment but before the start of an electrochemical experiment, carbon monoxide stripping was performed by cycling the crystal a few times between a potential in the HUPD regime to a potential in the double layer region.

3.2.3 Solution Resistance and Double Layer Charging Calculations

The first correction to consider for all electrochemical experiments is one for double layer charging (C_{dl}). By looking up expected C_{dl} values in literature, we can use the mathematical relationship $\tau = R_{\mathrm{s}}C_{\mathrm{dl}}$ to find the time constant (τ) for double layer charging process. To do so, we need to know the solution resistance (R_{s}) of our electrolyte. We'll start by noting that the tip of our reference electrode is less than 4 mm from the surface of our crystal, and the electrolyte for these measurements is 0.1 M $HClO_4$. The solution resistivity of 0.1 M $HClO_4$ used for this calculation was determined from an approximate calculation using the molar conductivities at infinite dilution, 349.65 cm^2 S mol^{-1} for H^+ and 6.73 cm^2 S mol^{-1} for ClO_4^- [100]

and assuming that they do not depend significantly on concentration. So at 0.1 M = 10^{-4} mol cm^{-3}, we have a conductivity, κ, of

$$\kappa = (349.65 + 6.73) \times 1 \times 10^{-4} = 3.56 \times 10^{-2} \text{ S cm}^{-1} \tag{3.3}$$

and a resistivity of

$$\rho = \frac{1}{\kappa} = 28.1 \ \Omega \text{ cm} \tag{3.4}$$

If we then assume that the electric field is uniform and normal to the surface of the working electrode, we can calculate the solution resistance using the formula below where ρ is resistivity, R_s is the solution resistance, and l is the distance between the reference and working electrodes. Using the area of our crystal, an l value of 4 mm, and our previously calculated value of 28.1 Ω cm for the solution resistivity we can calculate resistance in Eq. 3.5 as follows.

$$R_\text{s} = \rho \times l \tag{3.5}$$

$$R_\text{s} = 28.1 \times 0.4 = 11.2 \ \Omega \text{ cm}^2 \tag{3.6}$$

Now that we have the resistance of 0.1 M $HClO_4$, we can multiply by capacitance and get the time constant of the double layer charging for this system. In literature, the reported capacitance for Pt(111) is 73 μF cm^{-2} [101] and for Pt(100) is 30 μF cm^{-2} [102]. Using the relationship $\tau = R_\text{s} C_\text{dl}$ we then find for Pt(111)

$$\tau_{\text{dl,Pt(111)}} = 11.2 \ \Omega \text{ cm}^2 \times 73 \ \mu\text{F cm}^{-2} = 8.18 \times 10^{-4} \text{ s}$$

and for Pt(100)

$$\tau_{\text{dl,Pt(100)}} = 11.2 \ \Omega \text{ cm}^2 \times 30 \ \mu\text{F cm}^{-2} = 3.36 \times 10^{-4} \text{ s}$$

The theoretical values for resistance, capacitance, and the time constant of double layer charging calculated in this section will be compared to the experimental values determined for the potential step experiments further on in Sec. 4.2.2.

3.2.4 Monolayer Calculations

To determine the charge per displaced platinum atom during the oxidation process, the area associated with each platinum atom on the surface of the working electrode must be calculated. That number and the charge of an electron can then be used to find the charge density for one monolayer, σ_{ml}. From Fig. 2.9, it can be seen that the area associated with two equilateral triangles (or one rhombus) corresponds to a single Pt(111) atom. Thus the total number of platinum atoms on the surface could be calculated if we knew how many of these rhombuses could fit on the surface of the electrode used, which can be done by dividing the area of the crystal by the area of a unit cell. The calculation of the area of the rhombus can be simplified by just calculating the area of one of the two equilateral triangles within it and doubling that. One of the two equilateral triangles is shown in Fig. 3.5 outlined in green.The area, A_{triangle}, of an equilateral triangle is given in Eq. 3.7

$$A_{\mathrm{triangle}} = \frac{\sqrt{3}}{4} s^2 \tag{3.7}$$

where s is the side length of the triangle. The lattice parameter of Pt as used in our research at the ESRF was 3.9242 Å [103]. So the side length of the darker triangle containing the green triangle shown in Fig. 3.5 would be the diagonal of a square with the side length equal to the lattice parameter. This would mean that the diagonal is 5.5496 Å. We can then take the area of the large equilateral triangular plane shown in Fig. 3.5 using Eq. 3.8.

$$A_{\mathrm{triangle}} = \frac{\sqrt{3}}{4} s^2 = \frac{\sqrt{3}}{4} (5.5496)^2 = 13.336 \text{ Å}^2 \tag{3.8}$$

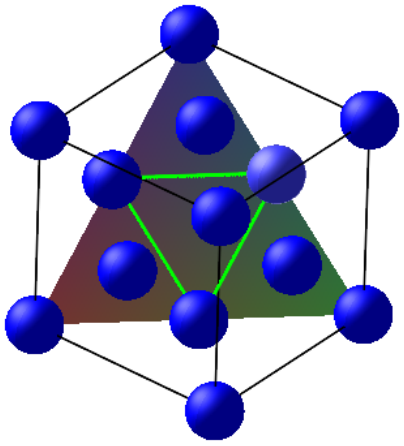

Figure 3.5: Example of the geometry associated with calculating the area of a single Pt(111) atom. One of the two equilateral triangles that corresponds to a single Pt(111) atom is outlined in green. Finding this area and then doubling it allows us to find the area associated with one Pt(111) atom.

The area, A_{triangle}, of the triangular plane shown in Fig. 3.5 incloses two Pt atoms. Thus the area, A_{PtAtom}, for one Pt(111) atom is half of that, 6.6681 Å^2. We can repeat this process for Pt(100) using similar geometry and find that the area associated with one Pt(100) atom is 7.6996 Å^2. If we then assume that there's one electron for each platinum atom, and already we know that the way we've defined unit cells for both Pt(100) and Pt(111) mean that there's one platinum atom per unit cell, then we can say that there's one electron for each unit cell. We can then use the fact that the charge of an electron is 1.60217×10^{-19} C and the area associated with a single Pt(111) atom is 6.6681 Å^2 and find the charge per unit area for Pt(111) as shown in Eq. 3.9.

$$\frac{1.60217 \times 10^{-19}\ \text{C}}{7.6996\ \text{Å}^2} = 240.27\ \mu\text{C cm}^{-2} \tag{3.9}$$

This process can be repeated with the area for Pt(100) and Pt(110) find that the charge per unit area is 208.08 μC cm^{-2} and 147.13 μC cm^{-2}, respectively. Literature

values by other groups find values of 240.3 μC cm^{-2} for Pt(111), 208.1 μC cm^{-2} for Pt(100), and 147.2 μC cm^{-2} for Pt(110) [104].

If a CV peak is integrated to yield charge and then the ratio of the charge of the peak with the calculated σ_{ml} of the specific surface is taken, the result is the unitless value of θ_{e}. This is the coverage expressed in monolayers and is equivalent to the number of electrons passed per surface platinum atom. It will be referred to as θ_{e} for the rest of this text.

3.3 X-ray Techniques

In addition to the electrochemical techniques, this research employed surface X-ray diffraction (SXRD) to study the formation of oxide on our platinum crystal surfaces. The first in situ SXRD studies performed on electrochemical systems was fairly recent, happening in 1988 [105] [106]. This combination of electrochemical techniques and SXRD allows us see the formation of the oxide structure in real time by using CV to induce surface oxidation and simultaneously monitoring the X-ray diffraction pattern. In this section, the X-ray experimental setup and the theory of SXRD and its components will be discussed. The results in this thesis were collected at the European Synchrotron Radiation Facility in Grenoble, France and at the Deutsches Elektronen-Synchrotron in Hamburg, Germany. Both of these facilities have synchrotrons, which are electron accelerators that make use of a closed ring to achieve the acceleration needed to create X-ray beams. All X-ray experiments were performed inside experimental hutches, which are lead lined to prevent X-ray exposure to the user. Figure 3.6 shows a panoramic photograph of the inside of experimental hutch ID31 as it was set up for a beam time in September 2018 at the ESRF. The incoming beam is on the right, the cell and electrolyte pump system on the goniometer in the middle, and on the left is the detector, which has been covered with beam stops to prevent damage to the detector at certain points of the reciprocal lattice where the

intensity counts will be too high.

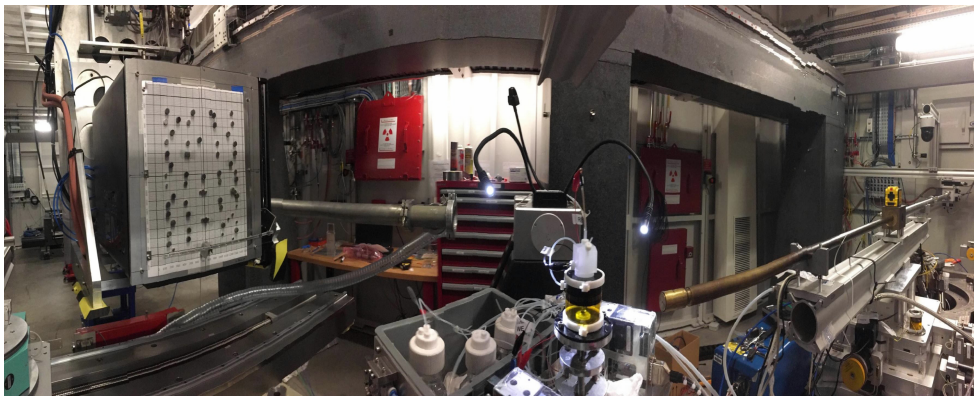

Figure 3.6: Panoramic photograph of the inside of the experimental hutch ID31 at the ESRF as it was in September 2018. The incoming beam can be seen coming from the ring into our specific hutch in the right side of the photo and being directed at the electrochemical cell (middle). To the left side the X-ray detector is seen covered in a specific pattern of beamstops in order to protect it from the reflected beams of too high intensity that will be present during this experiment.

Surface X-ray diffraction is a non-destructive technique used to study surface structures and requires very high energy particles in order to do so. This research is focused on the formation of platinum oxide at the surface of the electrode, and SXRD is an obvious choice for studying this because it can give a structural view of the surface of the crystal. The theory behind SXRD is simple; strike a sample with an X-ray beam and observe the scattering pattern. The interpretation and the math behind this technique and its analysis, however, is quite complicated and will be discussed in detail in this section.

3.3.1 X-ray Experimental Setup

In order to capture data from the X-ray scattering experiments, a Maxipix detector was used. As previously mentioned, the electrochemical cell setup was mounted to a goniometer, which allowed movement of the crystal surface in six directions to accurately align the beam in order to capture the desired portion of the crystal lattice

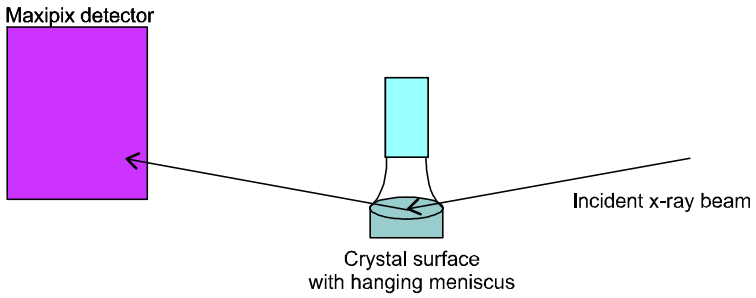

Figure 3.7: Schematic showing the X-ray experimental setup. To collect X-ray data, the crystal was placed in the path of the beam, and the maxipix detector was aligned behind it to capture the reflection. As shown, the incident X-ray beam goes through the hanging meniscus to the surface of the crystal, and reflects toward the detector. This setup allowed for the collection X-ray and electrochemical data simultaneously which provided real time data. Figure not to scale.

reflection. This careful, multidimensional alignment is crucial in gathering the X-ray data. A schematic of this setup including the X-ray beam is shown in Fig. 3.7.

3.3.2 Real and Reciprocal Space Lattice Vectors

As previously mentioned, careful alignment of the crystal surface is crucial to the success of X-ray experiments because it will determine what portion of the X-ray reflection the detector will capture. In order to be sure that the X-ray detector collects the desired portion of the reflection, we need to know the location and length of the reciprocal lattice vectors in relationship to the real space vectors. One of the fundamental concepts of X-ray diffraction is the mathematical relationship between the real and reciprocal space crystallographic lattices [107]. The real space lattice vectors were discussed in detail in Section 2.2.1, and we will use $\mathbf{a}$, $\mathbf{b}$ and $\mathbf{c}$ when referring to these vectors. In this section, we will discuss the relationship between $\mathbf{a}$, $\mathbf{b}$ and $\mathbf{c}$ and the reciprocal space vectors, which we will refer to as $\mathbf{a}^*$, $\mathbf{b}^*$, and $\mathbf{c}^*$. The mathematical relationship between the real and reciprocal, lattice vectors is given as

follows, where the dot represents the dot product.

$$2\pi = \mathbf{a} \cdot \mathbf{a}^* \tag{3.10}$$

$$2\pi = \mathbf{b} \cdot \mathbf{b}^* \tag{3.11}$$

$$2\pi = \mathbf{c} \cdot \mathbf{c}^* \tag{3.12}$$

All other combinations of dot products of any real and reciprocal space unit vectors will result in a value of 0 rather than 2π. The conventional unit cell for a face centered cubic like platinum is a cubic unit cell. We'll denote the real space lattice vectors of a cubic unit cell as $\mathbf{a}_{\text{cubic}}$ and the reciprocal lattice vector as $\mathbf{a}^*_{\text{cubic}}$. To find the location of $\mathbf{a}^*_{\text{cubic}}$, we note from Eqs. 3.10-3.12 that $\mathbf{a}_{\text{cubic}} \cdot \mathbf{a}^*_{\text{cubic}} = 2\pi$, $\mathbf{b}_{\text{cubic}} \cdot \mathbf{a}^*_{\text{cubic}} = 0$, and $\mathbf{c}_{\text{cubic}} \cdot \mathbf{a}^*_{\text{cubic}} = 0$. This means that $\mathbf{a}^*_{\text{cubic}}$ must be perpendicular to $\mathbf{b}_{\text{cubic}}$ and $\mathbf{c}_{\text{cubic}}$, and therefore must be parallel to $\mathbf{a}$. We can find the location of of $\mathbf{b}^*_{\text{cubic}}$ and $\mathbf{c}^*_{\text{cubic}}$ using the same set of equations and find that $\mathbf{b}^*_{\text{cubic}}$ is parallel to $\mathbf{b}_{\text{cubic}}$ because it must be perpendicular to $\mathbf{a}_{\text{cubic}}$ and $\mathbf{c}_{\text{cubic}}$, and that $\mathbf{c}^*_{\text{cubic}}$ is parallel to $\mathbf{c}_{\text{cubic}}$ because it must be perpendicular to $\mathbf{a}_{\text{cubic}}$ and $\mathbf{b}_{\text{cubic}}$. Now that we know where the reciprocal lattice vectors are in relationship to the real space vectors (and therefore each other), we need to find their lengths. We can do this by expanding the dot product to solve for the length of the reciprocal lattice vectors. Let's start by using the geometric definition of a dot product, given in Eq. 3.13, where $\mathbf{x}$ and $\mathbf{y}$ are two vectors, $|x|$ is the magnitude of $\mathbf{x}$, $|y|$ is the magnitude of $\mathbf{y}$, and $\phi_{x,y}$ is the angle between the two subscripted vectors x and y.

$$x \cdot y = |x||y| \cos(\phi_{x,y}) \tag{3.13}$$

Using this definition, we can expand Eq. 3.10 as shown in Eq. 3.14.

$$2\pi = |a||a^*| \cos(\phi_{a,a^*}) \tag{3.14}$$

We can then rearrange Eq. 3.14 to solve for the magnitude of $|a^*|$ as shown in Eq. 3.15.

$$|a^*| = \frac{2\pi}{|a|\cos(\phi_{a,a^*})} \tag{3.15}$$

We can rearrange Eqs. 3.11 - 3.12 in the same way to solve for their respective reciprocal space vector lengths, as shown in Eqs. 3.16 - 3.17.

$$|b^*| = \frac{2\pi}{|b|\cos(\phi_{b,b^*})} \tag{3.16}$$

$$|c^*| = \frac{2\pi}{|c|\cos(\phi_{c,c^*})} \tag{3.17}$$

As discussed earlier in the outcome of Eqs. 3.10 - 3.12, for a cubic unit cell the real vector and its reciprocal vector are parallel to each other. This gives us $\phi = 0$ for Eqs. 3.15 - 3.17 and because $\cos(0) = 1$, we can rewrite those equations as follows:

$$|a^*_{\text{cubic}}| = \frac{2\pi}{|a_{\text{cubic}}|} \tag{3.18}$$

$$|b^*_{\text{cubic}}| = \frac{2\pi}{|b_{\text{cubic}}|} \tag{3.19}$$

$$|c^*_{\text{cubic}}| = \frac{2\pi}{|c_{\text{cubic}}|} \tag{3.20}$$

Thus we find that the length of these cubic reciprocal space vectors is equal to 2π times the reciprocal of the spacing between the real space planes. In order to calculate the length of the reciprocal lattice vectors, we need to first know $|a_{\text{cubic}}|$, $|b_{\text{cubic}}|$, and $|c_{\text{cubic}}|$. As previously stated the lattice parameter for platinum is 3.9242 Å, and because this is the cubic unit cell, the lattice parameter is also equal to $|a_{\text{cubic}}|$, $|b_{\text{cubic}}|$ and $|c_{\text{cubic}}|$. Now that we have the lengths of the real space vectors, we can use the relationships outlined in Eqs. 3.18 - 3.20 and solve for the length of our reciprocal space vectors. In doing this we calculate that $|a^*_{\text{cubic}}| = 1.6021$ Å^{-1}, $|b^*_{\text{cubic}}| = 1.6021$ Å^{-1}, and $|c^*_{\text{cubic}}| = 1.6021$ Å^{-1}. The real and reciprocal lattice vectors for a cubic unit cell are

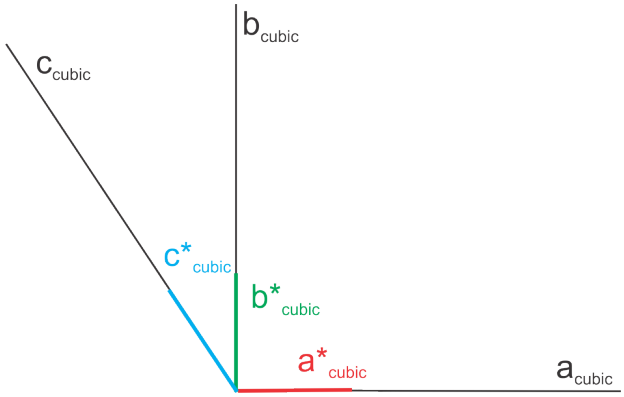

Figure 3.8: Schematic of how real and reciprocal space vectors are situated in three dimensions for the cubic unit cell. In this setup for the cubic unit cell, the reciprocal space vectors are along the real space vectors, and are in color; **a*** in red, **b*** in green, and **c*** in blue. Note that the **c** and **c*** vectors would point out of the page in three dimensions, and that the angle between all is 90°. $|a_{\text{cubic}}| = |b_{\text{cubic}}| = |c_{\text{cubic}}| = 3.9242$ Å,and $|a^*_{\text{cubic}}| = |b^*_{\text{cubic}}| = |c^*_{\text{cubic}}| = 1.6021$ Å^{-1}.

visualized in Fig. 3.8.

The conventional face centered cubic unit cell shown in Fig. 2.8 isn't the only unit cell for platinum. We could also find the real and reciprocal space vectors for a hexagonal unit cell, which is convenient for experiments with Pt(111). Let's think back to Fig. 2.9 to help us visualize the geometry we need to do to find the lengths of the real space vectors, $|a_{\text{hex}}|$, $|b_{\text{hex}}|$ and $|c_{\text{hex}}|$. $|a_{\text{hex}}|$ and $|b_{\text{hex}}|$ are simply the side lengths of the red rhombus outlined on the $(1, 1, 1)$ plane in Fig. 2.9. We can then use the geometry of a $45° - 45° - 90°$ isosceles triangle and find that the distance between two Pt(111) atoms is $\frac{a}{\sqrt{2}}$,where a is the lattice parameter of platinum. To find $|c_{\text{hex}}|$, we need to find the distance between two Pt(111) planes. To visualize this in Fig. 2.9, $|c_{\text{hex}}|$ would be the body diagonal of the entire cubic unit cell. Using the geometry for a cube, the body diagonal for the full cube would be a vector with the coordinates of its tail at (0,0,0) and the coordinates of its head at (a, a, a). Using the formula to find the magnitude of a vector, we find that $|c_{\text{hex}}| = a\sqrt{3}$.

To find the reciprocal space vectors for the hexagonal unit cell, $|a^*_{\text{hex}}|$, $|b^*_{\text{hex}}|$ and

$|c^*_{\text{hex}}|$, we need to think about the relationship between the real and reciprocal space vectors. Eqs. 3.18 - 3.20 worked for the cubic unit cell but they don't hold for the case of the hexagonal unit cell. This is because the angles between all the real vectors in a hexagonal unit cell are not all 90° as was the case in the cubic unit cell. For the hexagonal cell, the angle between $\mathbf{a}_{\text{hex}}$ and $\mathbf{b}_{\text{hex}}$ is 120°,the angle between $\mathbf{b}_{\text{hex}}$ and $\mathbf{c}_{\text{hex}}$ is 90°,and the angle between $\mathbf{a}_{\text{hex}}$ and $\mathbf{c}_{\text{hex}}$ is 90°. We can find where the reciprocal space lattice vectors of a hexagonal unit cell are in relationship to the real space vectors (and therefore each other) by again using the relationships in Eqs. 3.15 - 3.17 and the angles between the real space vectors Since $\mathbf{a}^*_{\text{hex}}$ must be perpendicular to $\mathbf{b}_{\text{hex}}$ and $\mathbf{c}_{\text{hex}}$, we know that $\mathbf{a}^*_{\text{hex}}$ is 30° away from $\mathbf{a}_{\text{hex}}$. Similarly, because $\mathbf{b}^*_{\text{hex}}$ must be perpendicular to $\mathbf{a}_{\text{hex}}$ and $\mathbf{c}_{\text{hex}}$, we know that $\mathbf{b}^*_{\text{hex}}$ is 30° away from $\mathbf{b}_{\text{hex}}$. Lastly, we know that $\mathbf{c}^*_{\text{hex}}$ is parallel to $\mathbf{c}_{\text{hex}}$ because it must be perpendicular to $\mathbf{a}_{\text{hex}}$ and $\mathbf{b}_{\text{hex}}$. Now that we know where the hexagonal unit cell reciprocal space vectors are, we can use the formulas we already derived in Eqs. 3.15 - 3.17 to find their lengths. This is done in Eqs. 3.21 - 3.23.

$$|a^*_{\text{hex}}| = \frac{2\pi}{|a_{\text{hex}}|\cos(30°)} \tag{3.21}$$

$$|b^*_{\text{hex}}| = \frac{2\pi}{|b_{\text{hex}}|\cos(30°)} \tag{3.22}$$

$$|c^*_{\text{hex}}| = \frac{2\pi}{|c_{\text{hex}}|\cos(0°)} \tag{3.23}$$

If we substitute the values we found for the hexagonal unit cell real space vectors in to Eqs. 3.21 - 3.23 and note that $\cos(30°) = \frac{\sqrt{3}}{2}$,then we can simplify to Eqs. 3.24 - 3.26.

$$|a^*_{\text{hex}}| = \frac{8\pi}{\sqrt{6}a} \tag{3.24}$$

$$|b^*_{\text{hex}}| = \frac{8\pi}{\sqrt{6}a} \tag{3.25}$$

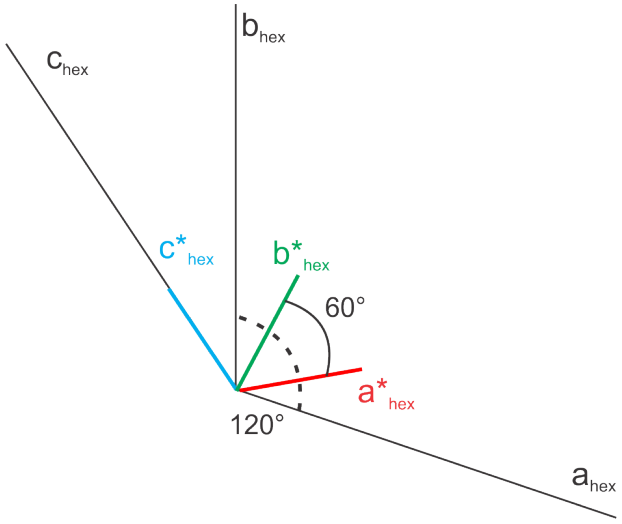

Figure 3.9: Schematic of how real and reciprocal space vectors are situated in three dimensions for the hexagonal unit cell. Here real space vectors are in black and the reciprocal space vectors are in color; **a*** in red, **b*** in green, and **c*** in blue. In this setup for the hexagonal unit cell, only the **c*** reciprocal space vector is along its corresponding real space vectors. Note that the **c** and **c*** vectors would point out of the page in three dimensions, and that the angles between the vectors aren't all 90 degrees, as was the case with the cubic unit cell.

$$|c^*_{\text{hex}}| = \frac{2\pi}{\sqrt{3}a} \tag{3.26}$$

We can use the relations outlined in Eqs.3.24-3.26 and solve for the length of our reciprocal space vectors because we know that the lattice parameter of platinum is 3.9242 Å, and we calculate that $|a^*_{\text{hex}}| = 2.6146$ Å^{-1}, $|b^*_{\text{hex}}| = 2.6146$ Å^{-1}, and $|c^*_{\text{hex}}| = 0.92442$ Å^{-1}.Now that we've found the locations and magnitudes of $\mathbf{a}^*_{\text{hex}}$, $\mathbf{b}^*_{\text{hex}}$, and $\mathbf{c}^*_{\text{hex}}$, we can visualize the real and reciprocal space vectors for a hexagonal unit cell in Fig. 3.9. Note that the angle between $\mathbf{a}^*_{\text{hex}}$ and $\mathbf{b}^*_{\text{hex}}$ must be 60° because $\mathbf{a}^*_{\text{hex}}$ is 30° away from $\mathbf{a}_{\text{hex}}$ and $\mathbf{b}^*_{\text{hex}}$ is 30° away from $\mathbf{b}_{\text{hex}}$ as we found earlier.

Up until this point we have discussed reciprocal space unit vectors. However, in our experiments, we are concerned with the points in reciprocal space that are along these vectors. Each lattice point in reciprocal space represents a set of parallel planes in real space. If we want to find a reciprocal lattice vector that represents the Pt(110)

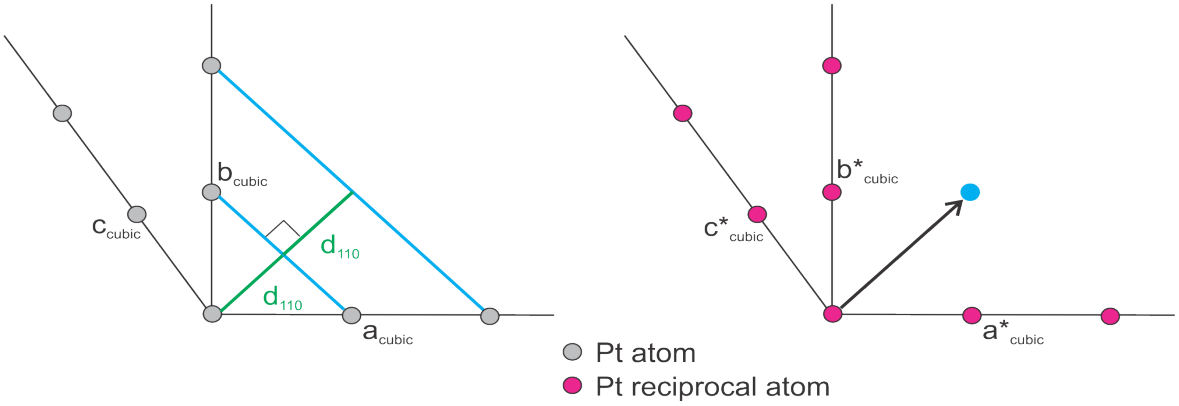

Figure 3.10: A visualization of a how a plane in real space and a point in reciprocal space are related. The grey circles represent atoms along the cubic unit cell (c_{cubic} is perpendicular to a_{cubic} and b_{cubic} and points out of the page in three dimensions). The blue line in real space on the left hand side of the figure represents the set of planes parallel to the $(1, 1, 0)$ plane. The blue circle in reciprocal space on the right hand side of the figure shows the point in reciprocal space that corresponds to the set of parallel planes in real space that are represented by the blue line.

planes for example, we note that the reciprocal vector, G, would follow Eq.3.27.

$$G_{110} = 1 \times a^*_{\text{cubic}} + 1 \times b^*_{\text{cubic}} + 0 \times c^*_{\text{cubic}} \tag{3.27}$$

Fig. 3.10 shows the drawing of this point in reciprocal space as a blue dot, and it represents the corresponding set of parallel planes (blue line) in real space which is also shown in the figure. We can apply some of the previous equations to the general reciprocal vector G_{hkl}, which is perpendicular to the (hkl) plane, and find that its length, $|G_{hkl}|$, is $\frac{2\pi}{d_{hkl}}$, where d_{hkl} is the spacing between the (hkl) plane. Understanding this relationship will help us correlate our X-ray data with what is happening on the surface of our crystal.

3.3.3 The Wavevector

The X-ray beam in these experiments can be considered as a vector in reciprocal space which is called the wavevector or k-vector. As previously mentioned, there are

as many lattice points in reciprocal space as there are sets of parallel planes in real space. In order to capture the desired portion of the reciprocal lattice, we need to know the angle and magnitude of the reflected beam (wavevector). We'll start by calculating the magnitude of the beam. We know that the energy of the beam for our experiments at the ID03 beamline of the ESRF synchrotron was 22.5 keV, and due to the conservation of energy we know that the energy of reflected beam must be the same. We can then solve for the k-vector using a series of equations that relate energy to momentum, and then momentum to the k-vector. Knowing that 22.5 keV is equivalent to 3.60×10^{-5} J, we can use Planck's Equation, where h is Planck's constant, to solve for the frequency, ν, as shown in Eq. 3.28.

$$\nu_{\text{beam}} = \frac{E_{\text{beam}}}{h} = \frac{3.60 \times 10^{-5} \text{ J}}{6.626 \times 10^{-34} \text{ m}^2 \text{ kg s}^{-1}} = 5.44 \times 10^{18} \text{ s}^{-1} \tag{3.28}$$

Knowing that the frequency of the beam used for our experiments, ν_{beam}, is 5.44×10^{18} s^{-1} we can use the relationship between wavelength, λ, and frequency to determine the wavelength of the beam as shown in Eq. 3.29, where c is the speed of light.

$$\lambda_{\text{beam}} = \frac{c}{\nu_{\text{beam}}} = \frac{3.00 \times 10^{8} \text{ m s}^{-1}}{5.44 \times 10^{18} \text{ s}^{-1}} = 0.551 \text{ Å} \tag{3.29}$$

Now that we have the wavelength of the beam as 0.551 Å, we can solve for momentum, p, using the de Broglie relationship in Eq. 3.30.

$$p_{\text{beam}} = \frac{h}{\lambda_{\text{beam}}} = \frac{6.626 \times 10^{-34} \text{ m}^2 \text{ kg s}^{-1}}{0.551 \text{ Å}} = 1.20 \times 10^{-23} \text{ kg m s}^{-1} \tag{3.30}$$

We have calculated that the momentum of the beam used for these experiments was 1.20×10^{-23} kg m s^{-1}. In order to relate momentum to the k-vector, we represent the X-ray beam as a plane wave. The k-vector is in the beam direction and its magnitude, $|k|$, is expressed in Eq. 3.31.

$$|k| = \frac{2\pi}{\lambda} \tag{3.31}$$

Combining Eqs. 3.30 and 3.31 leads to the following equation for momentum, now written as magnitudes so it is also true in three dimensions:

$$|p| = \frac{h}{2\pi}|k| \tag{3.32}$$

We can substitute our known values of momentum as calculated in Eq.3.30, and solve for the magnitude of our k-vector.

$$|k| \ = 1.20 \times 10^{-23} \text{ kg m s}^{-1} \times \frac{2\pi}{6.626 \times 10^{-34} \text{ m}^2 \text{ kg s}^{-1}} = 11.4 \text{ Å}^{-1} \tag{3.33}$$

The k-vector of our beam is calculated to be 11.4 Å^{-1} and points in the beam propagation direction. We also did some experiments at the ID31 beamline of the ESRF synchrotron where the energy of the beam was 68 keV. In these experiments, the magnitude of the k-vector was 34.4 Å^{-1}. The energy of the beam at DESY was 70 keV, and thus the magnitude of the k-vector for those experiments was 35.6 Å^{-1}.

3.3.4 Bragg Angles

In addition to knowing the k-vector of the beam, we also need to know the Bragg angle, ϕ_{Bragg}, which is the angle at which the reflected beam scatters off the crystal planes. In this section we'll do a calculation based on conservation of energy and conservation of momentum to find the Bragg angles. **A** in Fig. 3.11 shows the incoming beam, $\mathbf{k}_i$, striking some crystal planes and some of the possibilities for the location of the reflected beam, labeled $\mathbf{k}_f$. The reciprocal lattice vector $\mathbf{G}$, which is normal to the crystal planes is also shown, as well as the incident angle of $\mathbf{k}_i$ which is labeled θ_i. In part **B** of Fig. 3.11, we show that due to the conservation of momentum we can add $\mathbf{k}_i$ to $\mathbf{G}$ and the result (dashed green line) is the wavevector of the outgoing beam, $\mathbf{k}_f$. For interactions with a crystal the change in momentum is $\hbar\mathbf{G}$, therefore conservation of momentum gives $\mathbf{k}_f = \mathbf{k}_i + \mathbf{G}$. The black dashed

line in part **B** represents the Ewald sphere. It can be seen that $\mathbf{k}_i$ and $\mathbf{k}_f$ must both intersect the Ewald sphere. Translating $\mathbf{k}_f$ to have its origin at the end of $\mathbf{k}_i$ we find that the Bragg angle formed between the crystal planes and the outgoing beam $\mathbf{k}_f$ must be the same as the angle between the crystal and the incoming beam $\mathbf{k}_i$, as shown in part **C** of Fig. 3.11. To solve for $\phi_{\text{Bragg,Pt(001)}}$, we'll use the fact that we know $|c^*_{\text{cubic}}| = 1.6021$ Å^{-1} and for this calculation we'll use a beam energy of 22.5 keV for which $|k_i| = |k_f| = |k| = 11.4$ Å^{-1}. We can then use the simple right triangle trigonometry shown in part **B** of Fig. 3.11 now written mathematically in Eq. 3.34 to find $\phi_{\text{Bragg,Pt(001)}}$.

$$\phi_{\text{Bragg,Pt(001)}} = \arcsin\left(\frac{\frac{1}{2} \times |c^*|}{|k|}\right) = 4.029^\circ \tag{3.34}$$

So $\phi_{\text{Bragg,Pt(001)}} = 4.029^\circ$. We can do the same calculation for Pt(111) and find that $\phi_{\text{Bragg,Pt(111)}} = 2.324^\circ$.

3.3.5 Crystal Truncation Rods (CTRs)

As previously mentioned, points in reciprocal space correspond to a set of parallel planes in real space. For a perfect 3D infinite crystal, the reciprocal lattice points would go on forever and there would be no intensity between them. However, because the crystal used in this research is of finite size and is a mixture of 2D on the surface and 3D in the bulk metal, lines of intensity arise between the Bragg peaks which are called crystal truncation rods (CTRs). In practice, this means that we see minimal amounts of intensity all along the CTRs with maximum points of intensity at the reciprocal lattice points. Measuring the variations in X-ray intensity along the CTRs tells us about surface structures that are present. For a certain incidence angle of an X-ray beam onto the surface only the portions of the CTRs that intersect with the Ewald sphere (a construction that relates wavevector, Bragg angle, and the reciprocal lattice) can be seen on the detector. Thus the crystal must be rotated while

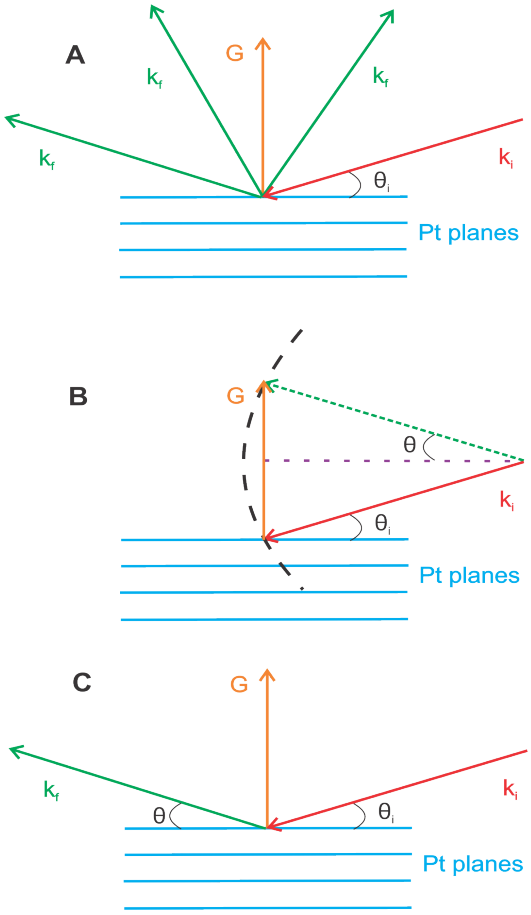

Figure 3.11: Schematic of how the conservation of both energy and momentum for an X-ray beam striking the parallel planes of a platinum crystal leads us to find the position of the reflected beam. In part **A** the conservation of energy is observed as $\mathbf{k}_i$ (incoming beam) is shown in red, and several possibilities for $\mathbf{k}_f$ (reflected beam) in green are drawn, which shows that the reflected beam must have the same energy as the incoming beam but that it could be in any direction. In **B**, the conservation of momentum is illustrated, as $\mathbf{k}_i$ and $\mathbf{k}_f$ must have the same incident angle, θ. In this drawing the vectors have been arranged head to tail in order to better illustrate the identical angles and the experimental geometry. Finally in **C**, the conservation of energy and momentum are shown together to find the reflected beam vector. The reciprocal lattice vector, **G**, is shown throughout the schematic in orange.

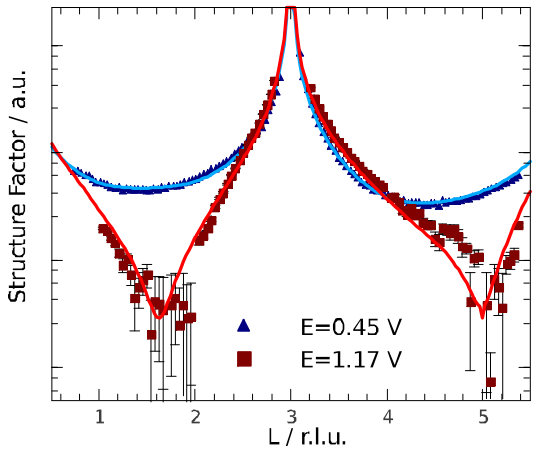

Figure 3.12: Example of Pt(111) crystal truncation rod (CTR) data. Two CTRs taken at different potentials are shown with their respective fits. The CTR data provides information about the location and coverage of the place exchanged platinum atoms. Reprinted from "Initial stages of Pt(111) electrooxidation: dynamic and structural studies by surface X-ray diffraction", J. Drnec, M. Ruge, F. Reikowski, B. Rahn, F. Carlà, R. Felici, J. Stettner, O. M. Magnussen, and D. A. Harrington, **224**, 220–227, Copyright (2017), with permission from Elsevier.

performing these X-ray experiments so that the Ewald sphere intersects at multiple places along a CTR in order to gain an understanding of what is happening all along the rod. Fig. 3.12 shows an example of two CTRs taken at different potentials and their fits. The data gained from CTR studies gives information about the location of place exchanged platinum atoms. From the fits of the CTRs to structural models, we can then deduce the structure of the place exchanged platinum atoms and their coverage.

Chapter 4

Results and Discussion

In this chapter, the results of this research will be discussed. First the results of integration of CVs will be explored and will be compared with X-ray data for Pt(111). Next, step experiments on various platinum surfaces will be explained and analyzed. Finally, the results of a sweep hold experiment will be discussed.

4.1 Integrations in Cyclic Voltammetry

A useful analysis method for CVs is to integrate the peaks. Doing so results in the charge associated with the process that correlates to the curve that is being integrated. From the charge, the coverage θ_e can be calculated which is then easily comparable with the X-ray data. In order to integrate peaks from a CV, the limits of the peak must first be defined so that the area associated with it can be calculated. This can be challenging because every CV is unique and so standardizing how to define the beginning and end of each peak is important for consistency when comparing oxidation and reduction charges between different surfaces. Additionally, each peak needs to be baseline corrected for double layer charging and any background reactions. The current seen in each peak in a CV is a combination of current from the surface process

occurring at that potential and also double layer charging. In order to accurately calculate the charge that is associated with the surface process in question, the double layer charging must be subtracted from the total charge of the peak. In this section, how those topics were addressed in this research and the outputs of integration will be explored.

4.1.1 Defining the Limits of a Peak

The first thing to consider when integrating a CV peak is how to define the limits of a peak. Fig. 4.1 shows the raw data of a Pt(111) CV, which has a peak that corresponds to oxidation at about 1.075 V. Looking at this peak, it's not obvious where it starts or stops. It could begin anywhere from the base of the peak before it at about 0.850 V up until about 1.000 V where the slope starts to drastically increase. Similarly, it could end anywhere from the low point on the right side of the peak around 1.100 V on the forward sweep to where the current becomes negative at about 1.100 V on the reverse sweep.

In this research, the right hand limit for the oxidation peak was always taken as the point at the largest potential. The limit for the left side of the oxide peak however is a bit more complicated. In theory, there should be a potential near the beginning of the peak that has the same current as the current in the double layer region. In practice, sometimes there are no potentials that have the same current, or there are many potentials that do. In the case of the many potentials, the left side of the peak was defined as the furthest positive potential that had the same current as the current in the double layer region. In the case where no potentials have the same current as the double layer region, the smallest potential between 0.7 V and 1.0 V (depending on which surface it is - on Pt(111) it would be the smallest potential after the butterfly peaks which occur around 0.7-0.8 V) that has a current value closest to that of the double layer is chosen as the beginning of the oxide peak.

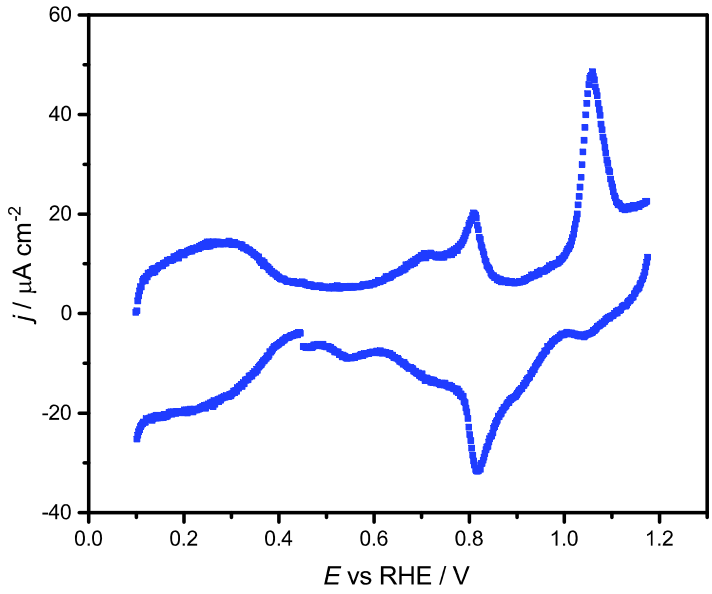

Figure 4.1: Pt(111) CV in 0.1 M $HClO_4$. Sweep rate 20 mV/s. Data from the IHCH925 beam time in February 2015, EC file 452.

4.1.2 Corrections for Double Layer Charging

One of the challenges to peak integration is correcting for double layer charging. As previously mentioned, double layer charging is an ever present non-Faradaic process. This means that double layer charging is occurring at all points during the CV, but the charge that passes due to this process doesn't contribute to the reaction occurring on the surface. Thus to accurately calculate the charge that contributes to the formation of the oxide, part of the charge seen in the oxidation peak must be assigned to double layer charging, and not to oxide formation. The simplest way to do this is to find the current in the double layer region of the CV, and subtract that off the peak of interest before integrating, but what exactly constitutes as the double layer region is often unclear as the surface is not always perfectly flat in that region and often the entire CV is shifted up or down depending on either the trace amounts of oxygen or beam-induced peroxide present in solution. The location of the CV in relationship

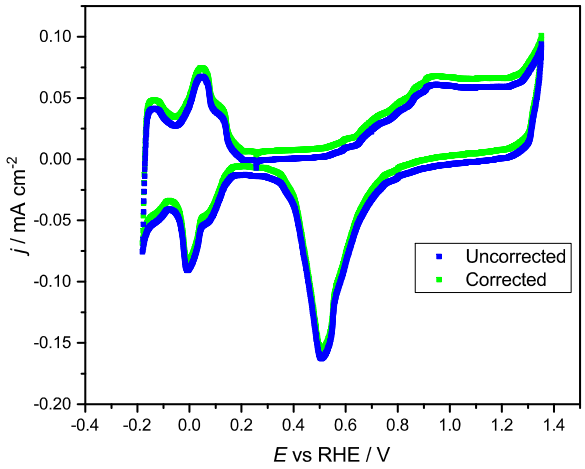

Figure 4.2: Cycled Pt(100) CV before and after being centered based on the equalizing of the HUPD regions about the x-axis. The blue line shows the raw CV data and the green line shows it after being centered around x = 0 based on equalizing the areas of the oxidation and reduction peaks of the HUPD region. 0.1 M $HClO_4$ with a sweep rate of 50 mV/s. Data from the CH1354 beamtime in March 2018, file 26.mps cycle 07.

to the x and y axes is irrelevant when thinking about the area of the peaks, but shifting the CV so that the oxidation and reduction charges of the HUPD peaks have equal area in respect to some horizontal line should give a baseline of zero because the amount of adsorption and desorption of hydrogen should always be the same. In light of this, the first step to analyzing a CV was to shift it either up or down so that the HUPD peaks had equal area in respect to the horizontal line, y = 0. This made integration of all peaks and any double layer corrections to them simplified. Fig. 4.2 shows a Pt(100) CV before (blue) and after (green) it was centered around y = 0 based on this method of equalizing the areas of the oxidation and reduction peaks of the HUPD region.

Once the peak limits have been assigned and the CV is aligned in this way, double layer charging must be corrected for before integrating for charge. A series of different baseline corrections can be done to try to compensate for the charge going to double

layer charging. Fig. 4.3 includes a zoom in of the Pt(111) oxide peak from Fig. 4.1 shown in black, and then a series of three different baseline corrections that could feasibly be made in green, red, and blue. The green line represents no correction for double layer charging, the red line represents a constant current double layer correction that is consistent with the current at the base of the peak, and the blue line shows a more severe, sloped double layer charging correction that also corrects for peroxide beam damage. Fig. 4.4 shows the outcome of integrating the oxide peak to get θ_e using each of these double layer corrections plotted against potential. The colors correspond to the corrections in Fig. 4.3, with green being no correction, red being the constant current correction, and blue being the sloped correction, and the dashed lines are best fits. It can be seen in Fig. 4.3 that no double layer charging correction leads to a θ_e value of about 1.75, the constant current correction leads to a θ_e value of about 0.8, and the sloped baseline correction results in a θ_e value of about 0.4. The green line clearly results in too large of a value because it doesn't correct for double layer charging which must be present. However, comparing this to the strictest baseline correction (blue) will give us an idea as to how to better the error arising from our correction. After literature comparison [86] [87] [88] which give a value of about 0.3 of a monolayer as typical, it was decided that either a constant current baseline or a sloped baseline is the best correction depending on the shape of the oxide peak. If the right side of the peak comes nearly back down to the height at which it started, then a constant current baseline is preferred. If, however, the peak comes down higher than it started as is the case in Fig. 4.1, a sloped correction is preferred to get charge values and peak shapes like those in literature [104] [37] [108].

The same sort of correction can be made for the reduction peak. Looking at the corrected Pt(100) CV in green in Fig. 4.2, we see that only two baselines can really be considered; no baseline correction (which we know will give us too large of a number because it doesn't account for double layer charging) and a flat baseline correction. The inflection point on both the left and ride side of the peak has been taken as the

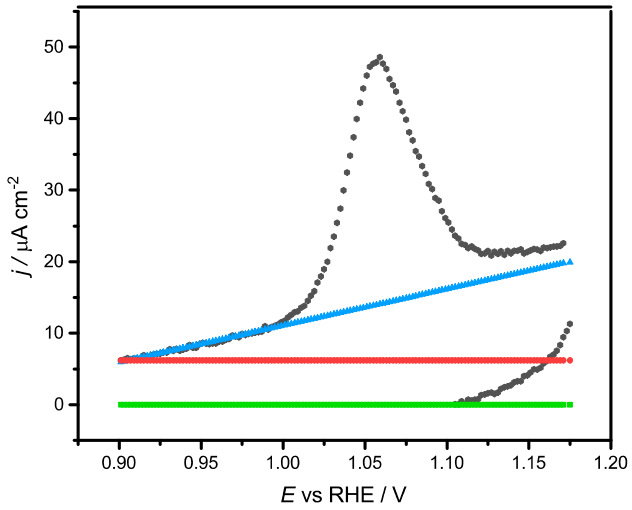

Figure 4.3: Three baseline possibilities to correct for double layer charging in a CV for a platinum oxide peak. The oxide peak is shown in black, and then a series of three different baseline corrections that could be made are in green, red, and blue. The green line represents no correction for double layer charging, the red line represents a constant current double layer correction that is consistent with the current at the start of the peak (as determined by the method described in Sec. 4.1.1), and the blue line shows a more severe, sloped double layer charging correction. Pt(111) CV in 0.1 M $HClO_4$. Sweep rate 20 mV/s. Data from the IHCH925 beam time in February 2015, EC file 452.

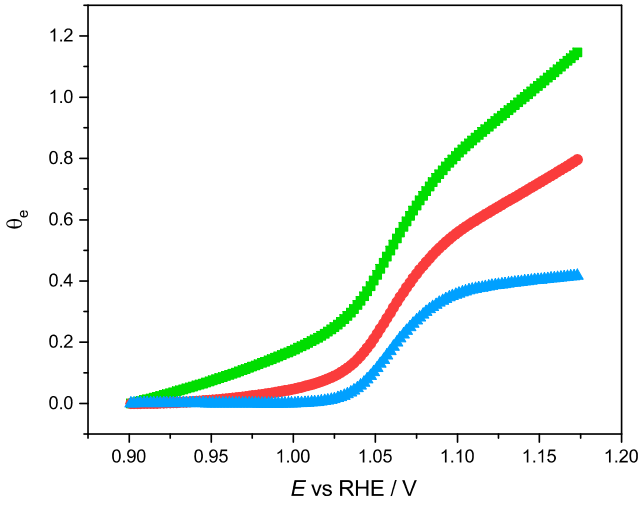

Figure 4.4: The outcome of integrating the charge of the oxide peak using the three double layer baseline corrections shown in Fig. 4.3 plotted against potential. The colors are consistent between the figures with the green line being no correction for double layer charging, the red line being the constant current correction, and the blue line being the sloped correction.

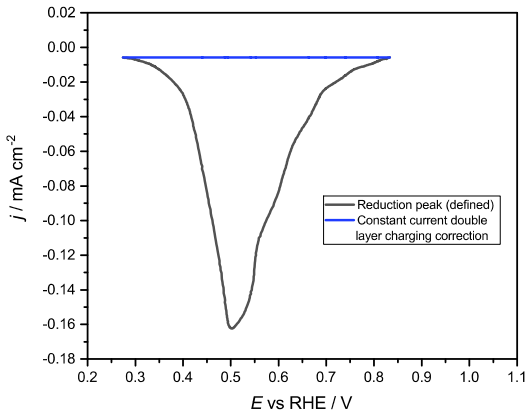

Figure 4.5: A defined reduction peak (black) and example of a baseline that provides a constant current double layer charging correction (blue). Data from the CH1354 beamtime in March 2018, file 26.mps cycle 07, Pt(100) in 0.1 M $HClO_4$.

start and end points of the peak, and the current at the start of the right hand side of the peak taken in order to correct for double layer charging. Fig. 4.5 shows the reduction peak from the CV shown in Fig. 4.1 now with a line drawn for the baseline correction. After integrating this reduction peak with a constant current double layer charging correction, the baseline correction here shown in blue agrees most similarly with the results of the integration of the oxidation peak for the same figure, and thus is taken to be the correct charge associated with the reduction peak. As with the oxidation corrections, a flat baseline is preferred in situations where the peak begins and ends at similar current values (as is the case in Fig. 4.5) and a sloped baseline is preferred in the case where the peak is less well defined, as in the case of Fig. 4.1. These forms of double layer charging corrections are present throughout the CV and sweep-hold work shown in this thesis. Step experiments require double layer charging correction as well, and the process of doing so is discussed further in Sec. 4.2.2.

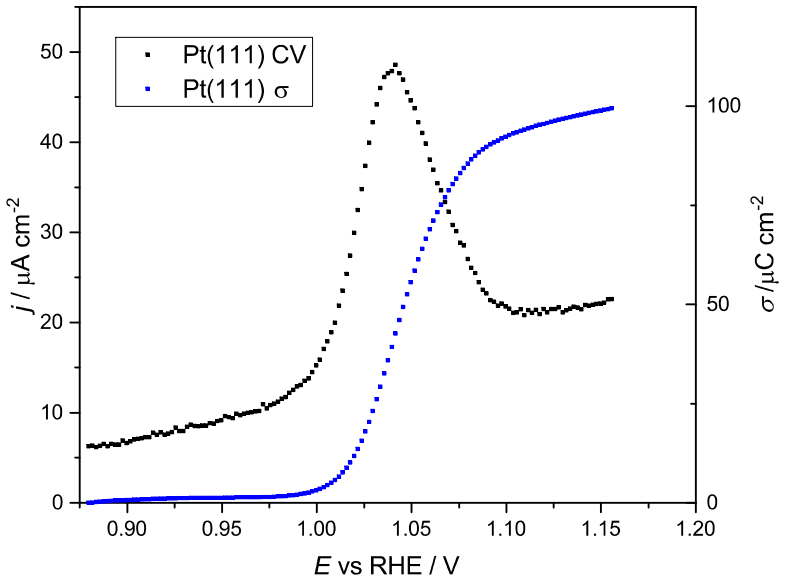

Figure 4.6: Charge density, σ, in blue overlaid with it's corresponding Pt(111) oxidation peak in black. Sweep rate 20 mV/s, CV conducted in 0.1 M $HClO_4$. Data from IHCH 925 beamtime at the ESRF in February 2015. EC file 452 cycle 1.

4.1.3 Outputs of Integration

It's interesting to look at the number of electrons per place exchanged Pt atom on the surface of our working electrode in order to see how much charge is dedicated to that process, and we can use the experimental CV data to do so. The charge density can be overlaid with the CV data of the oxidation peak to get a sense of how σ changes with potential. Fig. 4.6, Fig. 4.7, and Fig. 4.8 show examples for Pt(111), Pt(100), and Pt(110) respectively. As expected, the charge increases as potential increases and at rates corresponding to the change in current density. The σ and θ_e values for all three surfaces can plotted against potential to see how they compare to each other, as is shown in Fig. 4.9. Looking at these figures, it can be seen that the curves for all three surfaces have a range of potentials over which σ (and therefore θ_e) most rapidly increases. For Pt(111), the largest rate of increase is between 1.05 V and 1.125 V

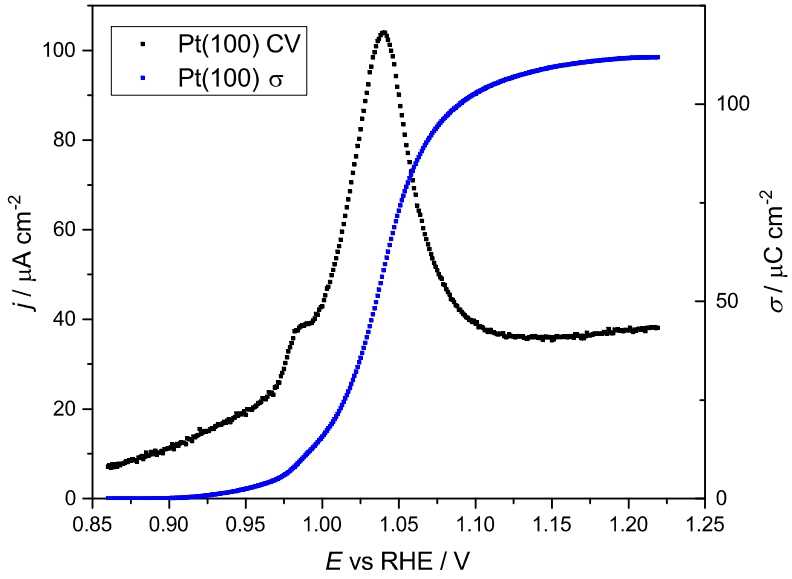

Figure 4.7: Charge density, σ, in blue overlaid with it's corresponding Pt(100) oxidation peak in black. Sweep rate 50 mV/s, CV conducted in 0.1 M $HClO_4$. Data collected in preparation for the CH5523 beam time in September 2018.

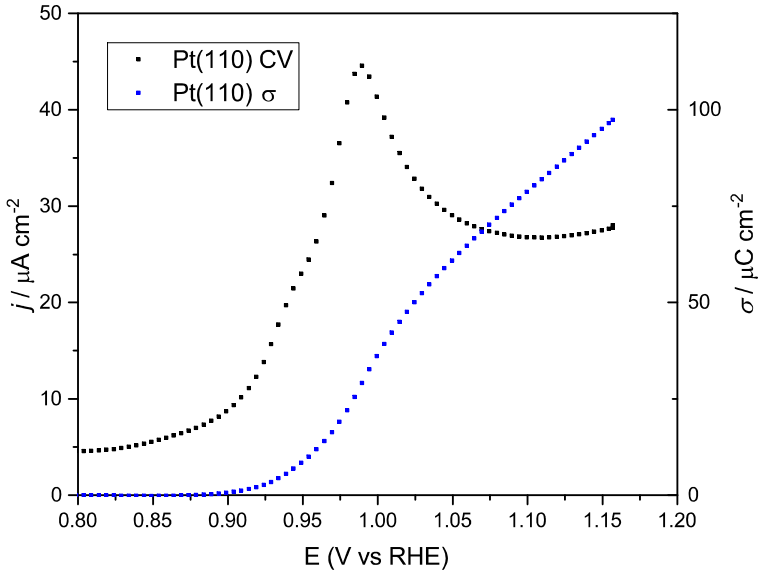

Figure 4.8: Charge density, σ, in blue overlaid with it's corresponding Pt(110) oxidation peak in black. Sweep rate 50 mV/s, CV conducted in 0.1 M $HClO_4$. Data from potentiostat file 25.mps from the DESY beamtime in December 2019.

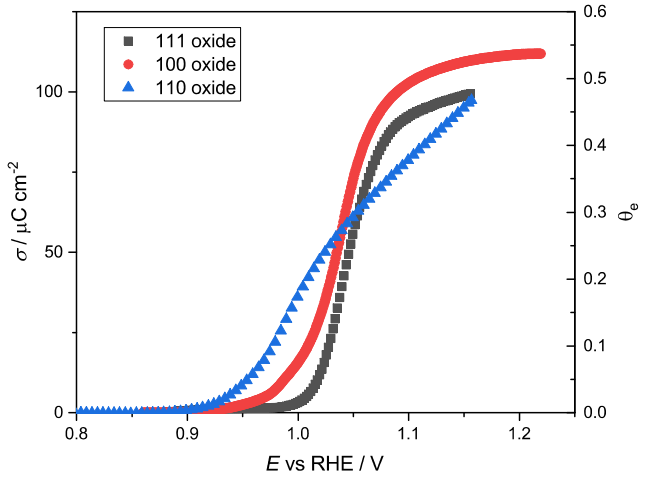

Figure 4.9: The σ values for three different platinum surfaces versus potential. Pt(111) data from the IHCH 925 beamtime at the ESRF in February 2015. EC file 452 cycle 1. Pt(100) data collected in preparation for the CH5523 beam time in September 2018. Pt(110) data from potentiostat file 25.mps from the DESY beamtime in December 2019.

which is about 0.5 V offset from that of Pt(100) and Pt(110) which increase fastest at lower potentials. This corresponds to the offset of the oxide peak potential for those surfaces and shows that the growth of oxide is most rapidly occurring at lower potentials for Pt(100) and Pt(110) than for Pt(111). It can also been seen from this data that the σ for the oxidation peak for all three surfaces is within 15 μC cm^{-2} and the θ_{e} values are all within about 0.1 ML. This means that for the three surfaces studied, about the same amount of oxide is formed.

4.1.4 Interpretation and Comparison with X-ray Data

The electrochemical data for these CVs can be compared with the X-ray data to give more detailed information about the surface. Fig. 4.10 shows the CV from Fig. 4.1 in blue overlaid with the corresponding (1, 1, 1.5) X-ray intensity in orange. From this data, the reversibility of the place exchange can be seen. The intensity is high at lower potentials while the surface is still ordered, and then at potential close to the oxidation peak on the voltammogram the surface order is disrupted and the X-ray intensity drops. Then as the potential is reversed, the intensity slowly recovers indicating that reversible place exchange has occurred. The θ_{e} values calculated using electrochemical measurements can be compared to data from the X-ray measurements, θ_{PE}, which is the number of place exchanged atoms. Fig. 4.11 shows a graph of both θ values plotted against each other, the slope of which results in the number of electrons passed per place exchanged atom. It can be seen that there are a few points at the beginning where electrons are being passed (θ_{e} is increasing) but no atoms are being place exchanged (θ_{PE} is not increasing). Once the place exchange starts, the slope of the curve can either be taken from the θ_{PE} range of -2.5×10^{-4} to 0.07, as indicated by the green dashed line or from the range 0.01 to 0.07 as indicated by the red dashed line. From the slope of the red line, of curve increases at a rate of about 1.7 electrons per place exchanged atom. This value is close to two, which would be consistent with the production of an oxidized platinum species in the +2 state, such as PtO.

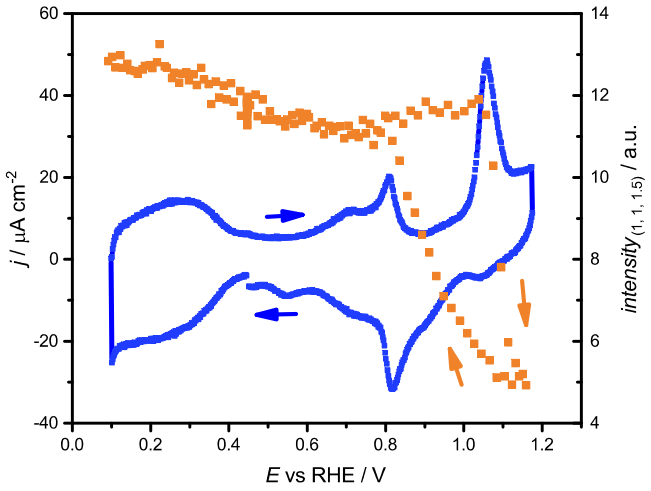

Figure 4.10: CV of Pt(111) overlaid with the corresponding (1, 1, 1.5) X-ray intensity. CV data is shown in blue, X-ray in orange. It can be seen that as the oxide is formed, there is a corresponding drop in intensity. As the potential is reversed, the intensity recovers which indicates a reversible oxidation process. Sweep rate 20 mV/s. Data from the IHCH925 beam time in February 2015, EC file 452, X-ray scan 664.

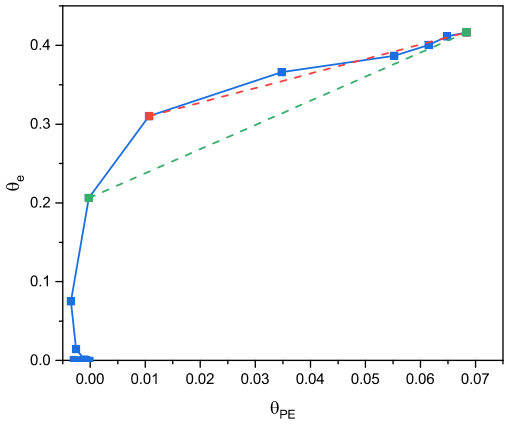

Figure 4.11: θ_e values plotted vs θ_{PE} values for the Pt(111) oxide peak. The resulting graph has a slope corresponding to the number of electrons passed per place exchanged atom. Pt(111) in 0.1 M $HClO_4$. Data from the IHCH925 beam time in February 2015, EC file 452, X-ray scan 664.

If the range is increased by one data point as the green line, the slope increases to 2.8. This value seems less likely, as the beginning of the θ_{PE} range corresponding to that fit is -2.5×10^{-4} and the slope of the raw data at that point still appears to be increasing due to a passing of electrons but not consistent with the movement of place exchanged platinum atoms.

In addition to giving us the oxidation state of the oxide, this data gives information about the number of steps in the reaction mechanism to form the oxide. If the formation of the oxide was a one step process, the X-ray intensity in Fig. 4.10 should gradually drop off with the increase in current associated with the state of the oxidation peak at 0.9 V. However, what is seen is the X-ray maintaining a high level of intensity until about the middle of the peak (1.1 V) when it suddenly and sharply drops off. This leads to a belief that the oxide formation is two processes; the first where electrons are passed but there is no movement of platinum atoms (such as an adsorption step) and then a second step where atoms are place exchanged to form platinum oxide. In a 2013 study, Feliu et al suggested a two component oxidation formation mechanism on electrochemical measurements alone [64], and the X-ray data gathered in this study coupled with electrochemical data in Fig. 4.11 corroborates this theory.

4.2 Step Experiments

4.2.1 Introduction and Theory

This section will examine how σ and θ_e vary with time and potential during potential step experiments. By doing so the kinetics of platinum oxide growth and reduction can be calculated as well as that of the double layer charging capacitance. Cyclic voltammetry also allows for examination of σ and θ_e for both double layer charging and Faradaic processes, but potential step experiments are particularly useful to con-

duct when investigating kinetics. When potential is constant as in a step experiment kinetic equations can be solved for quantitative solutions, which becomes much more difficult when potential is varied as in a CV. By monitoring the current response versus time to this sort of potential variation, the details of kinetic rate laws of the processes of interest can ultimately be solved for.

As previously mentioned, some charge goes to building and maintaining the double layer during every electrochemical experiment. In order to accurately calculate σ and θ_e for oxidation and reduction, the amount of charge that goes to the double layer needs to be calculated so that the charge found can be corrected for that component. To ensure that the kinetics of the oxidation process are in fact what is being calculated, we need to take into account other possible factors that could contribute to charge that are independent of the kinetics. For example, since potential step experiments jump from one potential directly to another instead of sweeping through the potentials in between as in a CV, there may be some lag between when we change the potential and when the potentiostat actually achieves the desired potential. This could then affect the calculated σ and θ_e values as the change in current and potential wouldn't reflect the behavior of an ideal step experiment. In short this means that the effects of the potentiostat response time need to be considered.

In an ideal world a change in potential would occur instantaneously, rising and falling infinitely fast but that's not what happens in practice. The potentiostat has a setting called bandwidth which determines how quickly the instrument can change the potential, which is what drives the experiment. The Biologic potentiostat that was used for this experiment could be set to a bandwidth setting between one and seven, where each number corresponds to a specific bandwidth cutoff frequency. The relationship between frequency and $\tau_{\text{potentiostat}}$ is given in Eq. 4.1.

$$\tau_{\text{potentiostat}} = \frac{1}{2\pi f} \tag{4.1}$$

The bandwidth setting used for these experiments was five, which corresponds to a frequency of 62 kHz. Substituting this frequency into Eq. 4.1, it is found that $\tau_{\text{potentiostat}}$ is 2.57×10^{-6} seconds. This is an estimate of how quickly potential can rise, and therefore is simply an order of magnitude calculation. In these experiments the potentiostat recorded data points roughly every 4×10^{-4} seconds, which is two orders of magnitude slower than $\tau_{\text{potentiostat}}$ which means that the potential should be quickly rising within a data point interval and there should be almost no lag in response time. This is found to be the case in the raw data as it rises to about 98% of the intended potential within the first data point.

The next thing to consider is if our experiments are capturing the double layer charging or if that process is faster than the potentiostat can measure data points. We can do this by calculating the time constant of the double layer charging process. This will require the use of Ohm's law given in Eq. 2.1 which relates potential (V), current density (j), and resistance (R) in a circuit. One way to model an ideal potential step experiment is as the equivalent circuit as seen in Fig. 4.12, where R_{s} is the solution resistance and C_{dl} is the double layer capacitance. This is the equivalent circuit to the schematic in Fig.2.3, where C_{dl} is the capacitor that represents the wall-like structure of anions built up on the surface of the metal and R_{s} is the solution resistance between the surface and the reference electrode at point 'C'. V_{s} will be the voltage drop across R_{s} and V_{c} the voltage drop across C_{dl}. The current density through R_{s} will be j_{s}, and j_{c} will be the current through C_{dl}. Finally, E will be the potential from point A to point C. Circuit theory can be used to solve for both solution resistance and double layer capacitance from the observed current decay in the potential step experiments. For each device in Fig. 4.12 we can set up a specific current relationship. Eq. 4.2 shows this relationship for R_{s}.

$$V_{\text{s}} = j_{\text{s}} R_{\text{s}} \tag{4.2}$$

For a capacitor, j_{c} is related to the capacitance and the rate at which V_{c} changes

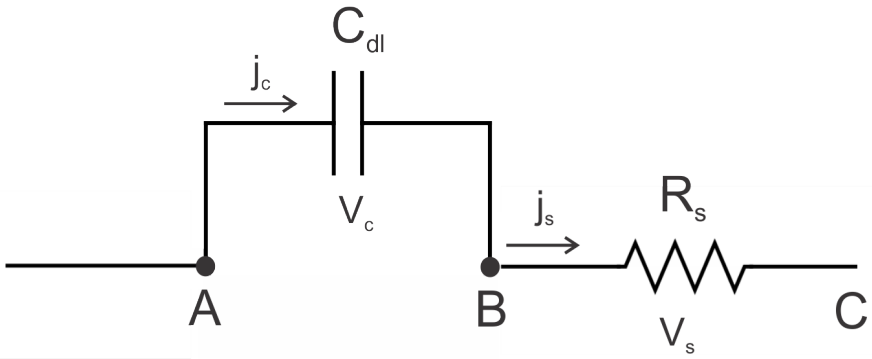

Figure 4.12: An equivalent circuit model of an ideal potential step experiment. R_{s} models the solution resistance and C_{dl} models the double layer capacitance. The break in the wire parallel to C_{dl} represents the fact that there is no charge transfer resistance.

with time as seen in Eq. 4.3

$$j_{\mathrm{c}} = C_{\mathrm{dl}} \frac{dV_{\mathrm{c}}}{dt} \tag{4.3}$$

From Kirchoff's current law, we know that at all times the relationship in Eq. 4.4 holds.

$$j_{\mathrm{s}} = j_{\mathrm{c}} \tag{4.4}$$

Thus we will refer to the current through the circuit as simply j. From Kirchoff's voltage law we know that the sum of the voltage drops must be equal to the applied potential, which leads to Eq. 4.5.

$$E = V_{\mathrm{s}} + V_{\mathrm{c}} \tag{4.5}$$

The initial conditions of interest for a potential step experiment are that the current is zero before the step. If $j = 0$ it follows from Ohm's law that V_s is also zero. Then from Eq. 4.5 it can be seen that if V_{s} is zero then the voltage across the capacitor is equal to the applied potential before the step, which we will call E_{initial}. Just after the step the conditions change and we will refer to the potential as E_{final} and the current as j_0. As potential changes from E_{initial} to E_{final}, current can be modeled as

a differential equation that can be solved as Eq. 4.6

$$j = j_0 \exp\left(-\frac{t}{\tau}\right) \tag{4.6}$$

where $\tau = R_s C_{dl}$ and j_0 is given by

$$j_0 = \frac{\Delta E}{R_s} \tag{4.7}$$

where $\Delta E = E_{\text{final}} - E_{\text{final}}$. Eq. 4.7 happens because potential cannot be instantaneously changed across the capacitor so all the additional potential comes across the resistor. This result also means that j_0 is potential dependent. Eq. 4.6 takes the form of an exponential decay, meaning that we would expect the current to decay exponentially during a potential step experiment. Ideally this means we could fit each current decay to an equation of the form of Eq. 4.6 and extract j_0 and τ from the fit. The first step to doing this analysis is to plot the the data on a log scale to check to see if is actually exponential, and then fit the initial stages of each step to a linear function. Eq. 4.8 shows an example of the form of the linear fit

$$\log(j) = \log(j_0) - \frac{t}{\tau} \tag{4.8}$$

and how j_0 (the intercept) and τ (the reciprocal of the slope) can be extracted from it. ΔE for each step is known and so Eq. 4.7 can be used to extract R_s. Since $\tau = R_s C_{dl}$, it is then simple to find C_{dl}. Once all the fits have been done and the values extracted, we can compare the τ_{dl}, R_s, and C_{dl} values with the expected values to test to see if what is being fitted is actually double layer charging. If they are the same the charge from that process can be corrected for by subtracting it off the fitted exponential, leaving only the Faradaic component.

4.2.2 Implementation and Analysis

In this section, the implementation of the above analysis will be shown for both oxidation and reduction of potential step experiments.

Oxidation Steps on Pt(100) in $HClO_4$ from the Double Layer

One step experiment conducted at the CH4799 beamtime at ID31 at the ESRF in July 2017 was steps on Pt(100) in 0.1 M $HClO_4$ where steps were taken from a potential in the double layer region (about 0.4 V) to various potentials in the oxide region. The potential was held constant at the upper potential for 60 seconds, and then was stepped back to about 0.4 V and held for 5 seconds. This process was repeated for potentials in 10 mV increments between 0.85 V and 1.22 V. Fig. 4.13 shows some plots of the raw data of the oxidation portion of a few representative steps of this experiment, and Fig. 4.14 shows the same steps but plotted on a log scale. Each step was held at the upper potential for a full minute, but it can be seen from this data that the current decays approximately back down to zero in about 0.2 seconds and so the entire step isn't shown.

A noticeable slope change can be seen in the plots of the early steps. This is not totally unexpected because the decay should be two separate processes if it is catching double layer charging. The first process should be a very quick exponential decay in the beginning of each step that is associated with double layer charging, and the second should be a slower decay that takes over from the first and is associated with the Faradaic component. As previously discussed, double-layer charging current for potential step experiments is a quick exponential decay, and so it's possible that the time constant of the exponential decay for these steps is faster than the frequency over which data points collected. If it is, that will vastly change the way that we correct as compared to if it is orders of magnitude larger than the time over which we collect data points. In this section we will calculate the double layer charging capacitance

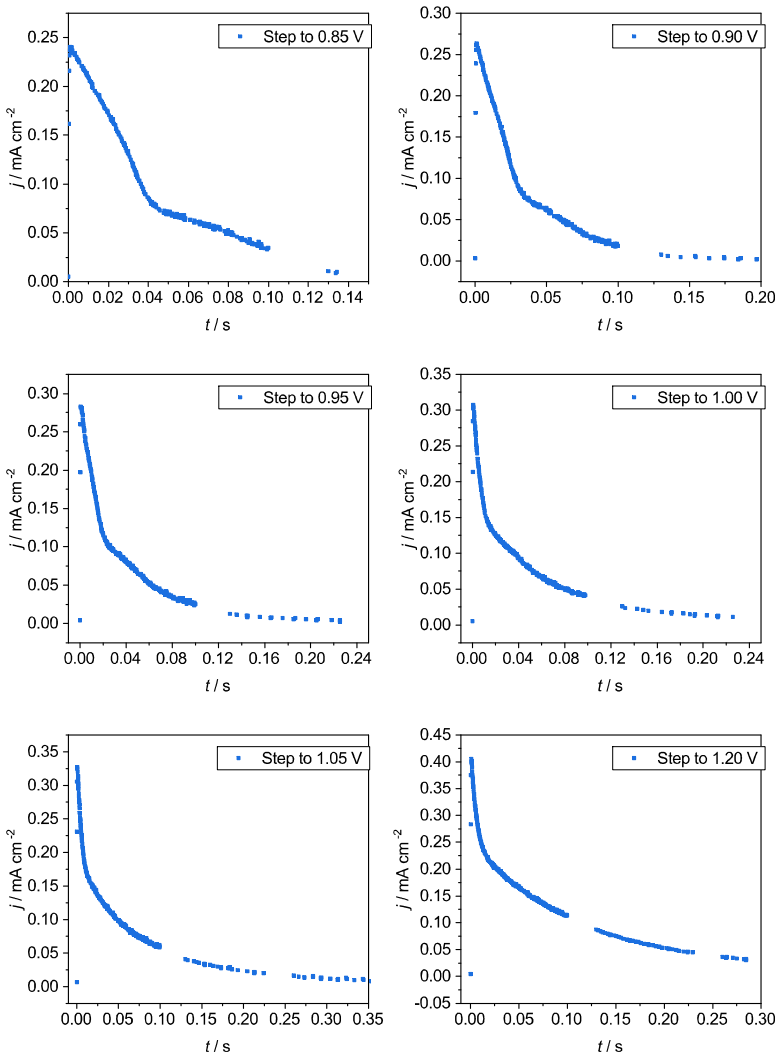

Figure 4.13: Example of the oxidation portion of six potential steps on Pt(100) in 0.1 M $HClO_4$ from the double layer at various potentials. The step to 0.85 V, 0.90 V, 0.95 V, 1.00 V, 1.10 V, and 1.20 V were chosen as the six representive steps out of the 36 in total. Data from EC file 57 at the CH4799 beamtime at ID31 at the ESRF in July 2017.

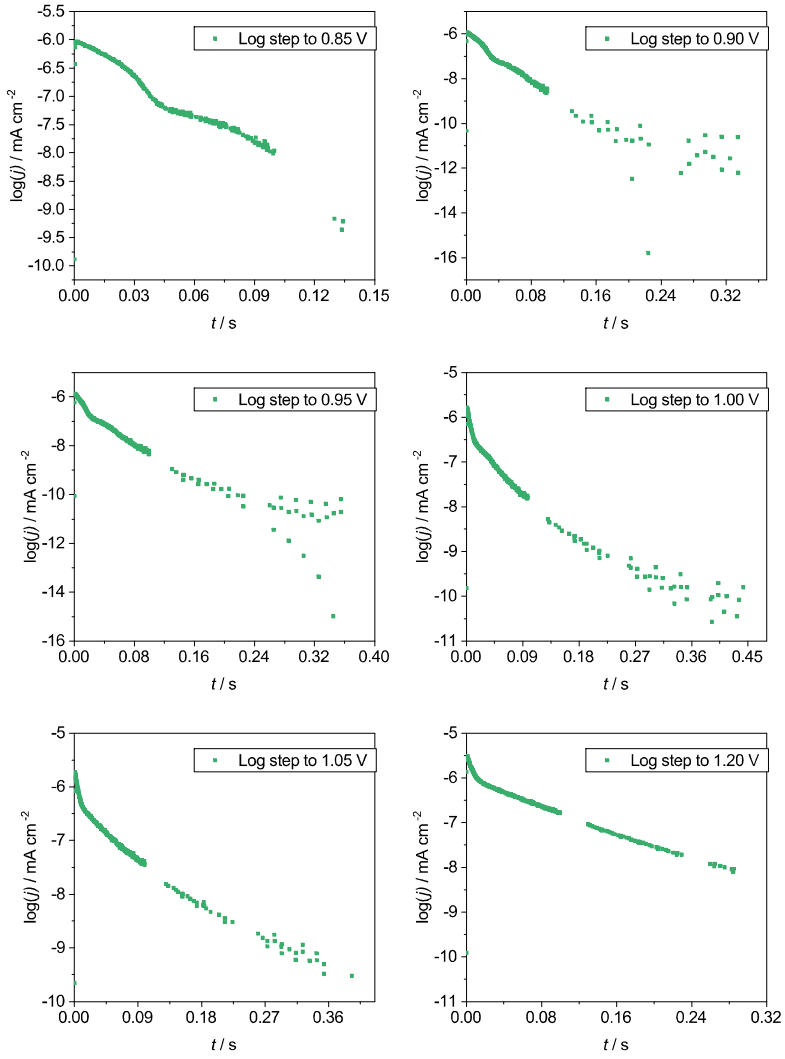

Figure 4.14: Log plots (base e) of the oxidation portion of six potential steps from the double layer on Pt(100) in 0.1 M $HClO_4$ at various potentials. The data in this figure is the log of the data in Fig. 4.13. Data from EC file 57 at the CH4799 beamtime at ID31 at the ESRF in July 2017.

for Pt(100) and Pt(111) in order to correct for this in the step experiments.

To try to find the portion of each step associated with double layer charging, we looked for an exponential decay in the early portion of each step. One noticeable issue with each step of the raw data is that there are about four points at the beginning of each oxidation and reduction step where the current and potential are still rising. An initial thought is that it is a lag in the potentiostat response, but that was disproved earlier when it was noted that the raw data showed no lag in potential rise. In order to fit these steps, those first points were excluded because they don't fit the shape of an exponential and thus complicate the fitting. It is evident from the plots of the raw data in Fig. 4.13 that these current decays take the form of an exponential for at least some portion of the beginning of each step. This is further confirmed by looking at the steps on a log scale as in Fig. 4.14 and noticing that there appears to be a linear section at the beginning of each step. This linear section on a log plot corresponds to an exponential portion on the raw data plot. Looking at the residual sum of squares from the linear fits of the log plots seen in Fig. 4.15, it can be seen that the log of the steps are linear for portions at the beginning of the step but deviate as time goes on. Smaller values indicate better linear fits. At first glance, it appears as if the errors of the fits don't appear to change much until about $t = 0.01$. However if we zoom in on Fig. 4.15 it can be seen that RSS is only consistently less than 0.0005 though about $t = 0.003$ which corresponds to about the first ten data points on each step. This zoom is shown in Fig. 4.16.

Using the fits of the first ten points which are attributed to an exponential decay in the beginning of the step, τ_{dl}, R_{s}, and C_{dl} were extracted and then plotted versus potential as seen in Figs. 4.17, 4.18, and 4.19, respectively.

It can be seen that the solution resistance is consistent throughout the potential range. This is a good sign because we would expect that the solution resistance would be constant between the various steps. A decrease and then leveling out of capacitance is what is to be expected for oxide growth, but not for double layer charging. At 0.85

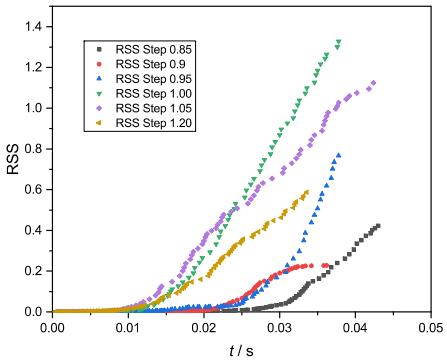

Figure 4.15: The residual sum of squares (RSS) from the linear fits of the initial seemingly linear portion of the log plots from the oxidation portion of potential steps on Pt(100) in 0.1 M $HClO_4$ from the double layer. The same six respresentive steps from Fig. 4.13 are shown. Data from EC file 57 at the CH4799 beamtime at ID31 at the ESRF in July 2017.

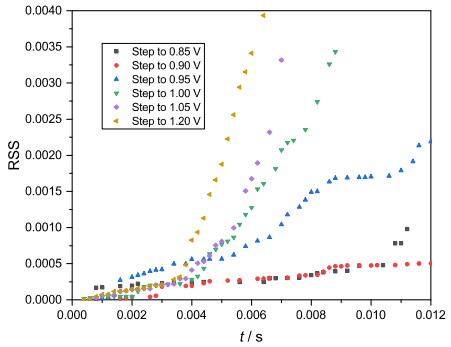

Figure 4.16: A zoom of the RSS from Fig. 4.15. The RSS value is only consistently less than 0.005 though about $t = 0.003$ which corresponds to about the first ten data points on each step. Data from EC file 57 at the CH4799 beamtime at ID31 at the ESRF in July 2017.

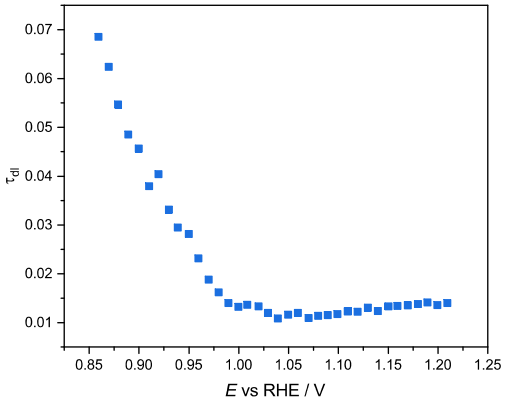

Figure 4.17: The time constant of the initial exponential decay plotted versus potential for the oxidation portion of potential steps on Pt(100) in 0.1 M $HClO_4$ from the double layer. It can be seen that the time constant gets smaller as the potential increases indicating a faster process. Data from EC file 57 at the CH4799 beamtime at ID31 at the ESRF in July 2017.

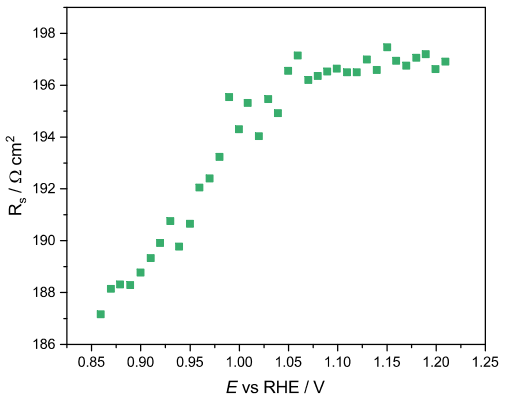

Figure 4.18: The solution resistance plotted versus potential for the oxidation portion of potential steps on Pt(100) in 0.1 M $HClO_4$ from the double layer. Data from EC file 57 at the CH4799 beamtime at ID31 at the ESRF in July 2017.

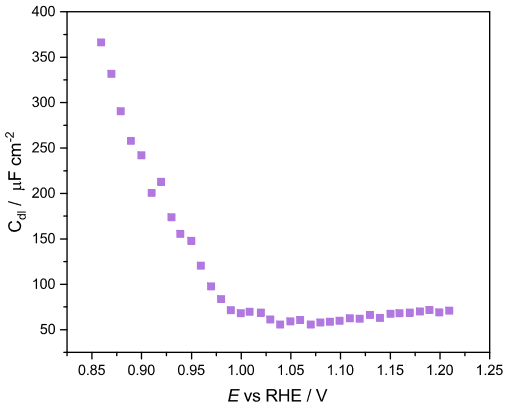

Figure 4.19: The capacitance of the initial exponential decay plotted versus potential for the oxidation portion of potential steps on Pt(100) in 0.1 M $HClO_4$ from the double layer. It can be seen that the capacitance gets smaller as the potential increases indicating a decrease in the rate of oxide growth. Data from EC file 57 at the CH4799 beamtime at ID31 at the ESRF in July 2017.

V, the oxide hasn't begun to form and the platinum metal is still a fairly clean surface. At this point the capacitance is high. As the potential is increased the oxide begins to form, creating an oxide layer that acts as an insulator and causes the capacitance to decrease. At some point the oxide reaches its peak and the capacitance levels out causing the flat line at about 1.00 V. The time constant mirrors this behavior. If this was double layer charging, we would expect that the time constant and capacitance doesn't change much with potential. This then leads to the conclusion that either we've missed the double layer charging process in this experiment because it is too quick, or that if it is there it does not heavily influence on the data.

Thinking back to the theoretical τ_{dl}, R_{s}, and C_{dl} previously calculated in Sec. 3.2.3, the experimental values are found to be much larger. For τ_{dl}, this reinforces the idea that we've missed double layer charging because the theoretical value calculated in Sec. 3.2.3. was about two orders of magnitude quicker than what is seen in Fig. 4.17. Additionally, double layer charging values from literature would be expected to be of the order of microseconds, which is much smaller than we are seeing here [109].

The R_s values seen in Fig. 4.18 are about one order of magnitude higher than the calculated value for R_s. This is somewhat reasonable as the geometry used to calculate the theoretical value assumed a counter electrode that was parallel to and of the same size at the working electrode 4 mm away. However, in practice we have a large working electrode and a smaller counter electrode that is quite far away. We can use a resistance formula [110] fitting to these experimental conditions as shown in Eq. 4.9.

$$R_s = \frac{\arctan(\frac{z}{a})}{2\pi a\kappa} \tag{4.9}$$

where z is the distance between the reference and working electrodes, a is the radius of the counter electrode wire, and κ is the conductivity calculated in Eq. 3.3. Using a z value of 4 mm and an a value of 0.5 mm, we estimate an R_s value of 129.3 Ω cm^2 which is consistent with the values shown in Fig. 4.18.

Reduction Steps on Pt(100) in $HClO_4$ from the Double Layer

The process above was then repeated for the reduction portion of the steps on Pt(100) in 0.1 M $HClO_4$ that were collected at the CH4799 beamtime at ID31 at the ESRF in July 2017. Fig. 4.20 shows some plots of the raw data of the reductive portions of the steps shown in Fig. 4.13. Each reductive step was held for five seconds, but it can be seen from this data that the current decays back to zero in about 0.2 seconds. In order to plot these values on a log scale to complete the RSS analysis as was done with the oxidation, the data was multiplied by negative one so that the log could be taken. All the data shown in this section was done on the data set once it was made positive. The RSS analysis for the first several points of each reduction step was taken as was done with the oxidation data resulting in Fig. 4.21. As before, when we zoom as in Fig. 4.22 we again see consistency of RSS values under 0.0005 through about $t = 0.003$. Using the fits of the reduction points through the first 0.003 seconds, τ_{dl}, R_s, and C_{dl} were again extracted for each step. Each reduction step was done

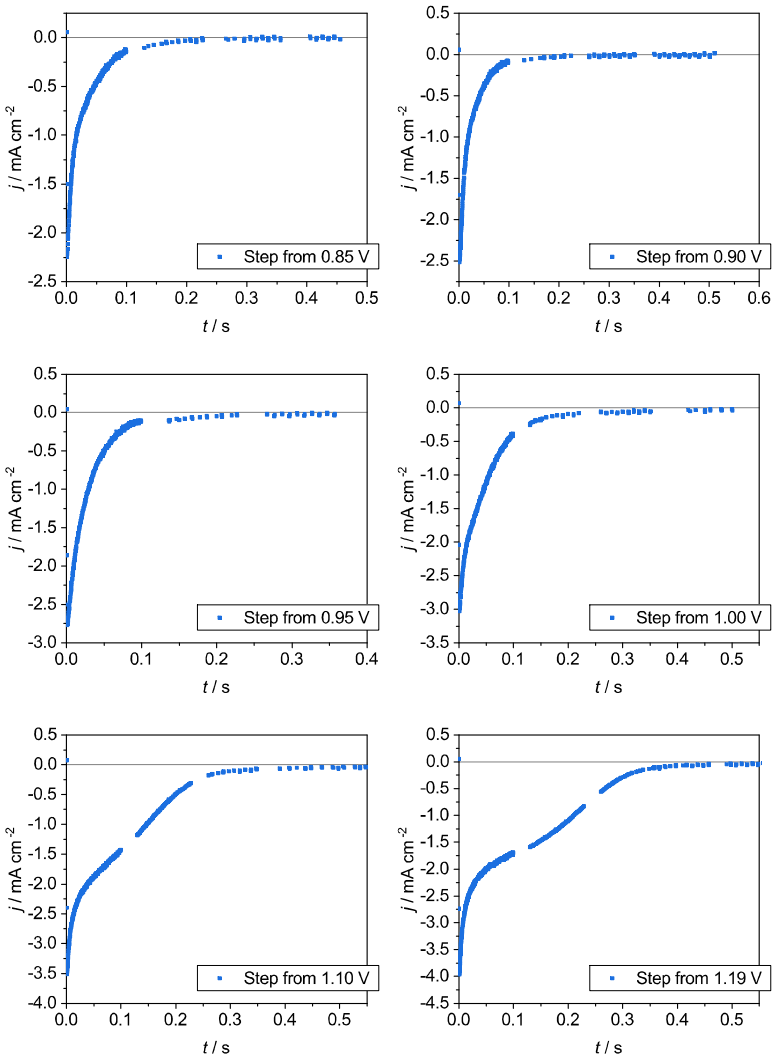

Figure 4.20: Example of the reduction portion of six potential steps on Pt(100) in 0.1 M $HClO_4$ from the double layer at various potentials. The step from 0.85 V, 0.90 V, 0.95 V, 1.00 V, 1.10 V, and 1.19 V were chosen as the six representive steps out of the 36 in total. Data from EC file 57 at the CH4799 beamtime at ID31 at the ESRF in July 2017.

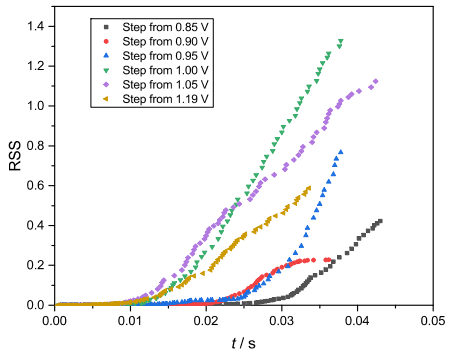

Figure 4.21: The residual sum of squares (RSS) from the linear fits of the log plots from the reduction portion of potential steps on Pt(100) in 0.1 M $HClO_4$ from the double layer. The six respresentive steps are shown. Data from EC file 57 at the CH4799 beamtime at ID31 at the ESRF in July 2017.

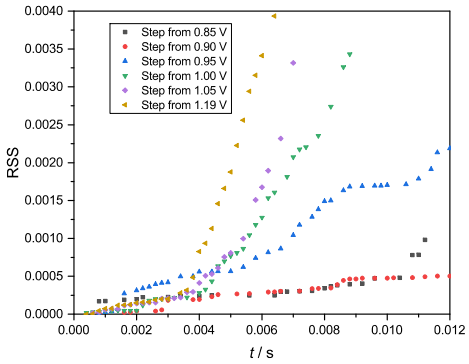

Figure 4.22: A zoom of residual sum of squares (RSS) from Fig. 4.21. The RSS value is only consistently less than 0.005 though about $t = 0.003$ which corresponds to about the first ten data points on each step. Data from EC file 57 at the CH4799 beamtime at ID31 at the ESRF in July 2017.

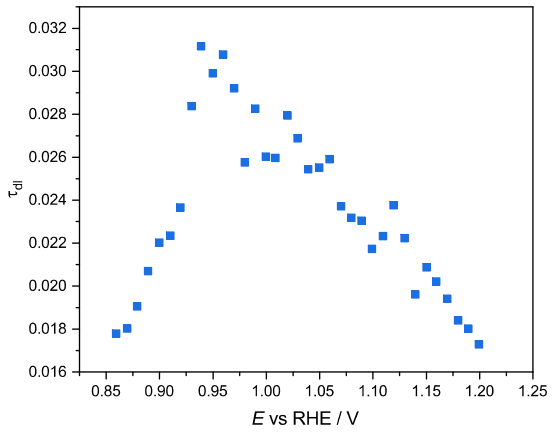

Figure 4.23: The time constant of the initial exponential decay plotted versus potential for the initial stages of the reduction portion of potential steps on Pt(100) in 0.1 M $HClO_4$ from the double layer. It can be seen that the time constant peaks at about 0.95 V. Data from EC file 57 at the CH4799 beamtime at ID31 at the ESRF in July 2017.

at the same potential, and so these values were plotted versus the potential which corresponds to the oxidation step just before the reduction as seen in Figs. 4.23, 4.24, and 4.25, respectively. As with the oxide data, it can be seen that the solution resistance is consistent throughout the potential range which is what is expected. The peak in both the capacitance and time constant graphs is interesting to see, but again points to a process that isn't double layer charging. The capacitance increases on the potential range from 0.85 V to about 0.95 V, which makes sense for reduction because as the potential increases, the amount of oxide that is present and therefore that can be reduced increases. This causes a sudden increase in capacitance of the metal as potential increases. At about 0.95 V the capacitance reaches a maximum and then begins to decrease as the oxide becomes a more irreversible process. If this was double layer charging, we'd expect the capacitance to be constant as the potential varies. Additionally, the values are of the same order of magnitudes as they were for oxidation, leading again to this process being too slow to be double layer but having R_s values on the right order of magnitude for the formula in Eq. 4.9.

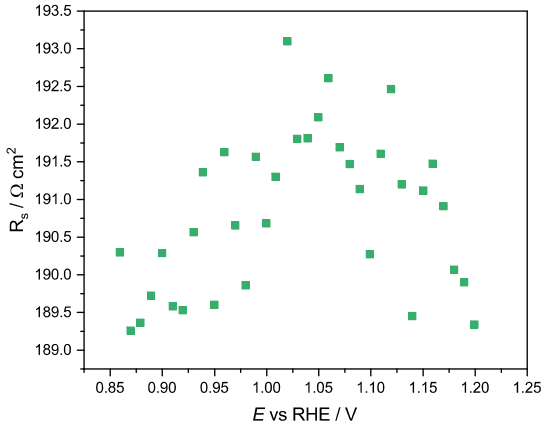

Figure 4.24: The solution resistance plotted versus potential for the initial stages of the reduction portion of potential steps on Pt(100) in 0.1 M $HClO_4$ from the double layer. It can be seen that the solution resistance is consistent throughtout the potential range. Data from EC file 57 at the CH4799 beamtime at ID31 at the ESRF in July 2017.

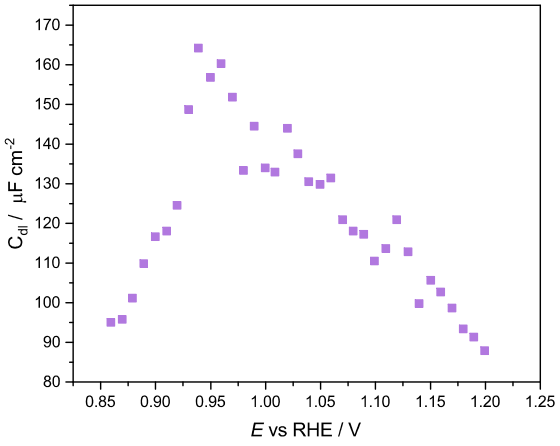

Figure 4.25: The capacitance of the initial exponential decay plotted versus potential for the initial stages of the reduction portion of potential steps on Pt(100) in 0.1 M $HClO_4$ from the double layer. It can be seen that the time constant peaks at about 0.95 V. Data from EC file 57 at the CH4799 beamtime at ID31 at the ESRF in July 2017.

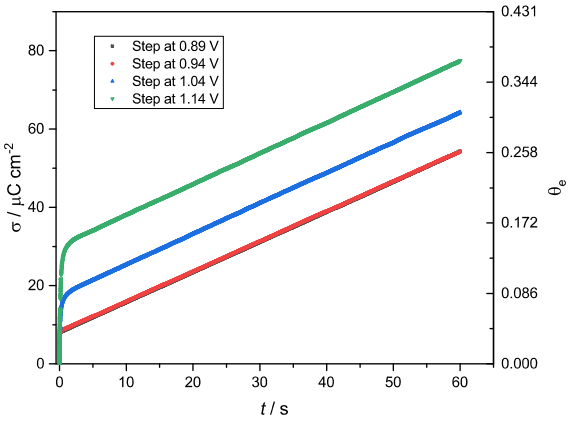

Figure 4.26: The charge associated with several representive steps on Pt(100) in 0.1 M $HClO_4$ from the double layer. It can be seen from the data that there is a linear slope indicating a constant increase of charge after the first 2 seconds or so whic shouldnt occur if the current for each step is decaying back to zero. This indicates that the current isn't decaying back to zero as initially thought. Data from EC file 57 at the CH4799 beamtime at ID31 at the ESRF in July 2017.

Charge and Coverage of Pt(100) in $HClO_4$ from the Double Layer

Keeping in mind that the double layer charging isn't affecting the charge of each step much, the integration of each step should yield the charge and therefore coverage due to oxide growth or reduction at each potential. Fig. 4.26 shows charge plotted versus time for the integration of a few representative steps on Pt(100) in 0.1 M $HClO_4$ stepping from 0.4 V (in the double layer region) at various potentials.. It can be seen from the Figure that the potential rise happens in the first two seconds, and then we see a linear rise for the rest of each step. That linear trend shouldn't be there if the current is decaying back to down to zero. More likely, the current is coming down to some value to just above zero which is causing a linear increase in charge over the entirety of the sixty second hold. Thus considerations should be made for the need for baseline corrections for something other than double layer charging. Beam damage can cause the oxidation of hydrogen peroxide impurities in solution to be oxidized to O_2 at potentials above 0.8 V. This induced oxidation causes a flat baseline correction

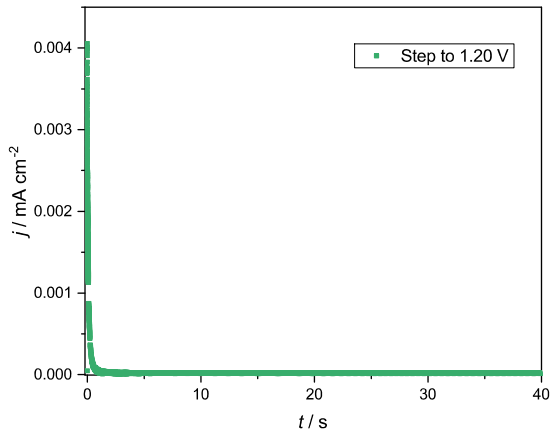

Figure 4.27: The raw step data from the step to 1.20 V on Pt(100) in 0.1 M $HClO_4$ from the double layer. Data from EC file 57 at the CH4799 beamtime at ID31 at the ESRF in July 2017.

because it is a process that is diffusion limited. Fig. 4.27 shows one of the steps out to 40 seconds. Looking at Fig. 4.27 it appears that the current bounces around zero, but upon taking a closer look we find that it comes down to just above zero, which acts as a baseline that causes the linear increase in the area as the step is integrated over the full 60 seconds as seen in Fig. 4.26. This was corrected for with a horizontal baseline whose height is the average of the last 1000 points of each step. Fig. 4.28 shows an example of this baseline in blue overlaid with the original step data for the step at 1.20 V in green.

Each step can be baseline corrected in this way and then integrated to find the charge associated with it. Fig. 4.29 shows charge corrected for by a constant current baseline plotted versus time for a few representative steps. It can be seen from this Figure that the charge levels off after the first few seconds indicating a current decaying back to zero as expected in the potential step experiments. The total charge and the coverage associated with each step was plotted versus potential for both the oxidation and reduction steps in Fig. 4.30. The oxidation and reduction steps have about the same charge at each potential indicating a fully reversible oxidation process.

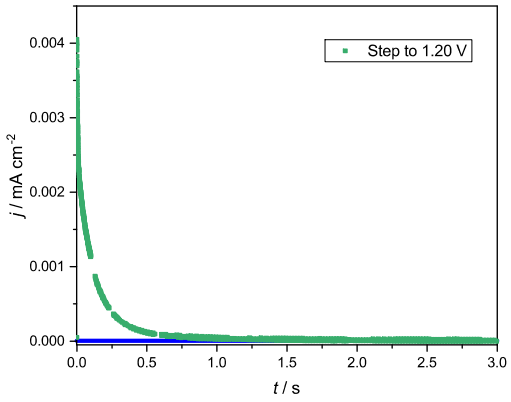

Figure 4.28: The step from Fig. 4.27 and the baseline used to correct for non-zero current. The value of the linear baseline is the average of the last twenty points of each step. Data from EC file 57 at the CH4799 beamtime at ID31 at the ESRF in July 2017.

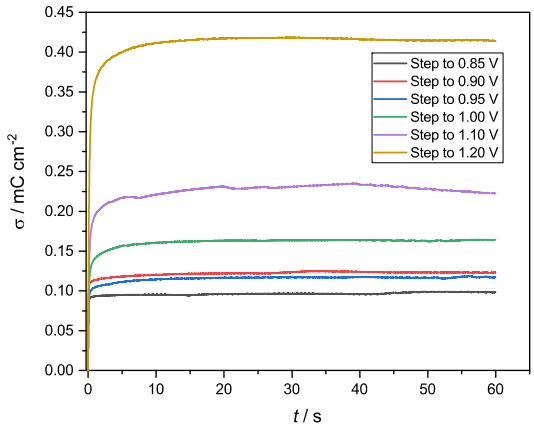

Figure 4.29: The charge associated with several representive steps on Pt(100) in 0.1 M $HClO_4$ from the double layer after being corrected for with a constant current baseline. It can be seen from the data that there is no longer a constant increase of charge after the first 2 seconds after correcting for the non zero current. Data from EC file 57 at the CH4799 beamtime at ID31 at the ESRF in July 2017.

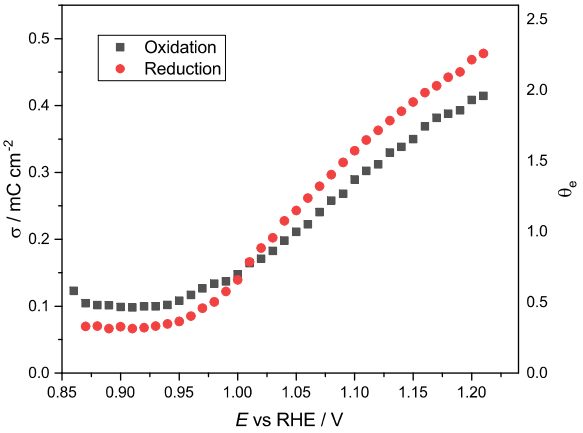

Figure 4.30: The θ_e and σ values plotted versus potential for steps on Pt(100) in 0.1 M $HClO_4$ from the double layer. The θ_e and σ values plotted versus potential for steps on Pt(100) in 0.1 M $HClO_4$ from 0.4 V (in the double layer region). The values for oxidation are shown in black and the values for reduction are shown in red. Data from EC file 57 at the CH4799 beamtime at ID31 at the ESRF in July 2017.

Thinking back to the shape of the raw data shown in Fig. 4.13, there appear to be two components to each step. The initial theory that this first component was attributed to double layer charging was disproved, leading to the belief that the oxidation has two phases. Fig. 4.31 shows the charges associated with both the first and second component of each step plotted versus potential. The first component is mostly constant at all of the potentials, where as the second component increases somewhat linearly with potential. This suggests a two step process for oxidation, the first that requires a constant charge and the second that has a charge that increases with potential. This points to an adsorption type first step and a place exchange type second step. It is seen in Fig. 4.31 that both components have about the same charge up until about 0.95 V, which is about where the current of the oxide peak starts to increase quickly as seen in the Pt(100) CV in Fig. 2.14. The division between the first and second component for Fig. 4.31 was determined by eye for each step and is therefore only an estimate of the total charge and trend for each component. The two component nature of the process seen agrees with the X-ray and electrochemical data

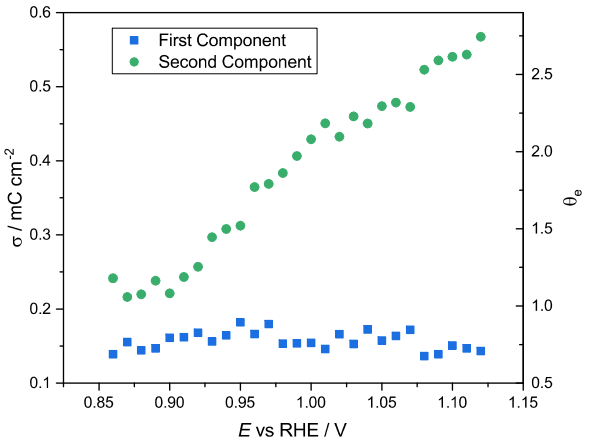

Figure 4.31: The charges of both components plotted versus potential for steps on Pt(100) in 0.1 M $HClO_4$ from a potential in the double layer region. The blue shows the first component, and the green shows the second component which includes the data out to the end of the step. The division between the first and second component was determined by eye for each step.

for Pt(111) shown in Fig. 4.11 which also shows two regions. Specifically it shows a two step oxidation reaction mechanism with first step that passes many electrons but doesn't place exchange atoms and a second step that passes 2 electrons for each place exchanged atom. A possible mechanism for this two step process is proposed as follows:

$$\mathrm{Pt(site)} + \mathrm{H_2O} \rightleftharpoons \mathrm{PtOH(ads)} + \mathrm{H^+} + e^- \tag{4.10}$$

$$\mathrm{PtOH(ads)} + \mathrm{OH^-} \rightleftharpoons \mathrm{PtO} + \mathrm{H_2O} + e^- \tag{4.11}$$

where the first step is adsorption of OH^-in solution to an available platinum surface site to form PtOH(ads). This process generates electrons but doesn't place exchange atoms. After some certain coverage, the second step which yields PtO begins. Both steps then occur simultaneously which would lead to 2 electrons for each place exchanged atom as indicated by the X-ray data.

Steps on Pt(100) in $HClO_4$ from the HUPD Region

This same step experiment was conducted on Pt(100) in 0.1 M $HClO_4$ during the IHRCH1354 beamtime at ID31 at the ESRF in March 2018. This time, however, instead of stepping from a potential in the double layer region, the potential was in the HUPD region (about 0.08 V). By analyzing this data in the same way as was done in Sec. 4.2.2, Fig. 4.32 was generated. Comparing this to the data in Fig. 4.30, which is Pt(100) steps from the double layer region, the most noticeable thing is the increase in the σ and θ_e values. Stepping from the HUPD region seems to result in θ_e values about 1.5 times higher than stepping from the double layer. This extra charge is likely from the additional peaks that are stepped over when stepping from a potential in the HUPD region than from stepping from a potential in the double layer. The shape of the oxidation data is quite similar to the shape of the oxidation data in Fig. 4.30. Both the step experiment from the double layer and the step experiment from the HUPD region show reduction values higher than oxidation values at higher potentials, but the reduction values are noticeably higher when stepping from the HUPD region, which is expected because holding at a more negative potential should result in more reduction.

Again the charges for the first and second component for this experiment were plotted versus potential as seen in Fig. 4.33. As in Fig. 4.31, the first component is mostly constant at all of the potentials, whereas the second component increases somewhat linearly with potential. This again suggests a two step process for oxidation, the first that requires a constant charge and the second that has a charge that increases with potential as proposed previously. The difference here is that the values of the second component are always larger than the first component, where as in Fig. 4.31 there were some potentials were both components were roughly equal. Additionally, the overall values for both components are larger. Likely this is due to the fact that when stepping from a potential in the HUPD region, we have to step

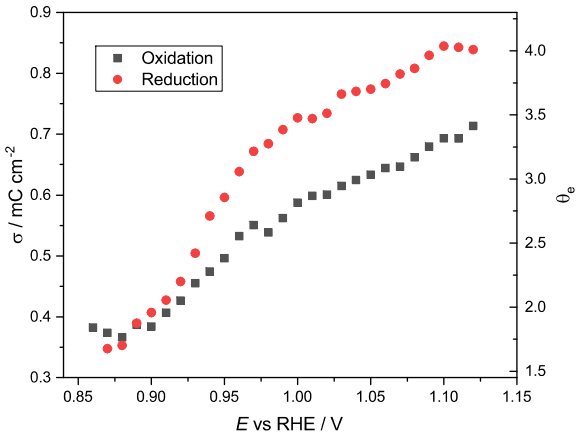

Figure 4.32: The θ_e and σ values plotted versus potential for steps on Pt(100) in 0.1 M $HClO_4$ from the HUPD region. The values for oxidation are shown in black and the values for reduction are shown in red. Data from EC file 24 at the IHCH1354 beamtime at ID31 at the ESRF in March 2018.

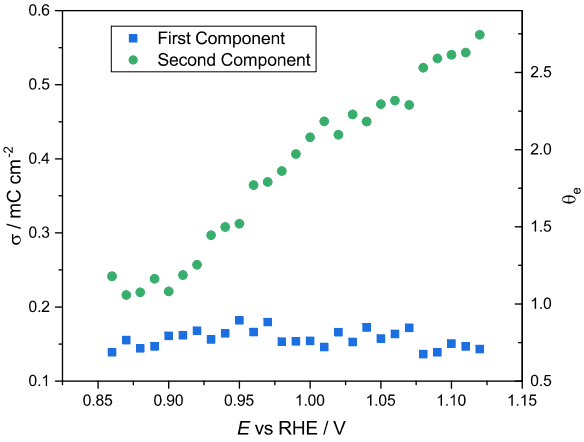

Figure 4.33: The charges of both components plotted versus potential for steps on Pt(100) in 0.1 M $HClO_4$ from a potential in the HUPD region. The blue shows the first component, and the green shows the second component which includes the data out to the end of the step. The division between the first and second component was determined by eye for each step.

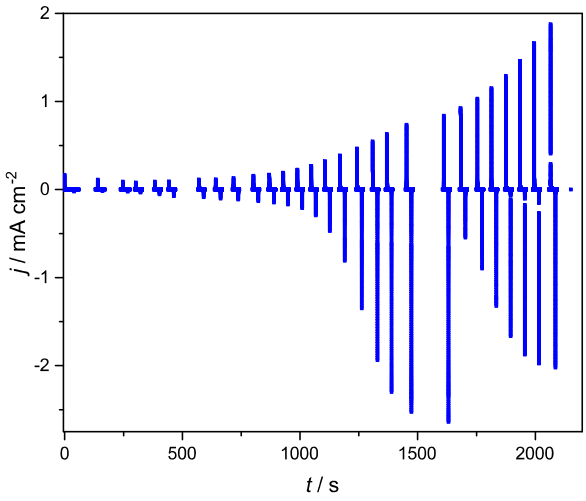

Figure 4.34: Raw data from a step experiment conducted on Pt(111) in 0.1 M $HClO_4$. Data from EC file sixc004 from the the IHCH10377 beamtime at ID31 at the ESRF in January 2017.

over some peaks that are missed when stepping from a potential in the double layer region and that is what is contributing the extra charge in both components.

Steps on Pt(111) in $HClO_4$ from the Double Layer

A similar step experiment was conducted on Pt(111) in 0.1 M $HClO_4$ during the IHCH10377 beamtime at ID31 at the ESRF in January 2017. The raw data for this experiment is shown in Fig. 4.34. By analyzing this data in the same way as was done in Sec. 4.2.2, Fig. 4.35 was generated.

It is interesting to compare this Figure to the data in Fig. 4.30, which is Pt(100) under the same circumstances. The biggest thing of note is that the σ for Pt(100) around 1.20 V is about double the σ value for Pt(111) at the same potential. It isn't surprising that the values on Pt(111) are less than on Pt(100) because Pt(111) is a more stable surface. The shape of the oxidation data also appears to almost be exponential in shape which wasn't the case with the Pt(100) data indicating a faster

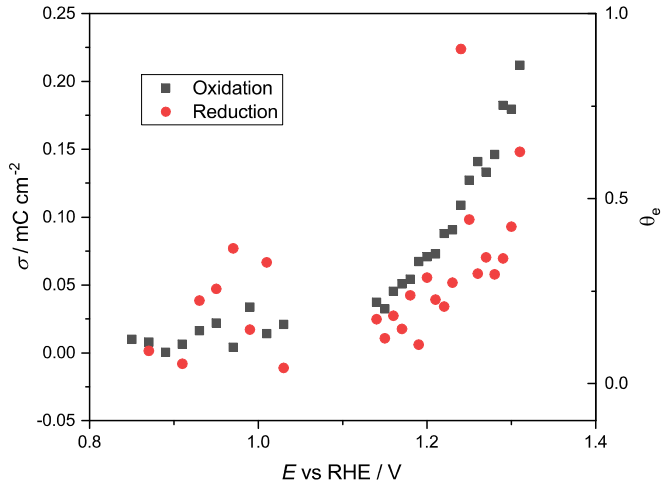

Figure 4.35: The θ_e and σ values plotted versus potential for steps on Pt(111) in 0.1 M $HClO_4$ from the double layer. Data from sixc file number 4 from the the IHCH10377 beamtime at ID31 at the ESRF in January 2017.

oxide growth rate at higher potentials for Pt(111) than Pt(100).

4.3 Sweep-Hold Experiments

It is interesting to compare the θ_e and σ values from step experiments and sweep-hold experiments to see if it matters whether potential is swept or stepped to the oxidation region. A sweep-hold experiment was conducted on Pt(100) in 0.1 M $HClO_4$ where the potential was held for five seconds at 0.15 V (which is in the HUPD region), swept up to a potential in the oxide region and held there for 20 seconds, swept down to 0.1 V, and then back to 0.15 V. The potentials in the oxide region ranged from 0.85 V to 1.25 V and were increased in 10 mV increments with a sweep rate of 20 mV/s. The original raw data for this experiment is shown in Fig. 2.7. As with all CV analysis in this thesis, the raw data was centered about the x-axis so that the areas of the HUPD regions for each CV are equal before any other analysis was done. To analyze sweep-hold data, the current decay at the hold potential is integrated in order to

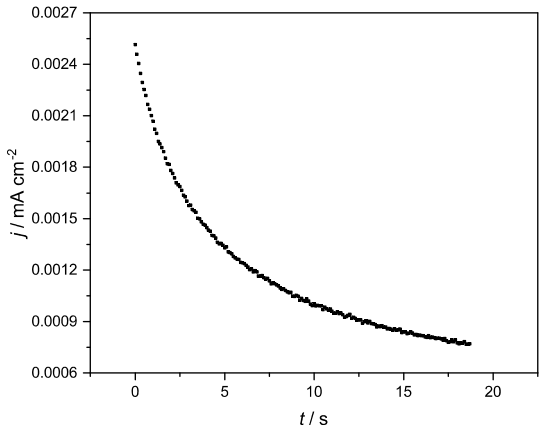

Figure 4.36: Zoom in of the current decay from the hold at 0.85 V from Fig. 2.7. Data from the from the CH5523 beam time in September 2018 at the ESRF, EC file 15.mps.

obtain θ_e and σ values. Fig. 4.36 shows a zoom in of the current decay at 0.85 V out to the last positive current data point. It can be seen from this Figure that the current appears to decay exponentially as it does in the step experiments, but there are not two distinct components as was seen in the potential step experiment current decay plots. This is likely because the effects of the first feature could be something that happened at potentials that were already swept over on this experiment and so the current decay here appears to have just one feature.

By design, a sweep hold experiment doesn't need to be corrected for double layer charging in the hold period. If we think about the equivalent circuit for a sweep hold experiment, the capacitor would be nearly fully charged by the time the potential hold occurs. Therefore the effect of the capacitor doesn't need to be considered because the effects would be minimal. The θ_e and σ values found both from integrating the current decay of each step in Fig. 2.7 and from integrating the entire oxide peak (corrected for double layer charging during the sweep portion) for each sweep are plotted versus potential in Fig. 4.37.

The black data set in Fig. 4.37 shows the θ_e and σ values found from integrating

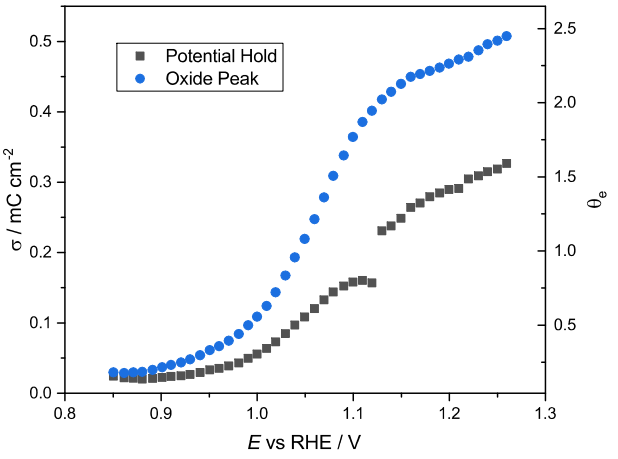

Figure 4.37: The θ_e and σ values for a sweep-hold experiment on Pt(111) in 0.1 M $HClO_4$. The black data set shows the values for just the current decay at the hold potentials for this experiment, and the blue shows the values for the entire oxidation peak from that cycle including the portion from the current decay. Data from the CH5523 beam time in September 2018 at the ESRF, EC file 15.mps.

just the current decay that occurs at the hold potentials in this experiment (an example of which is shown in Fig. 4.36). The black data only shows the charge associated with the hold at a specific potential, and therefore will be smaller than the charges at corresponding potentials for the potential step experiments. In order to compare this data to the potential step experiments, the total charge of the oxide peak (corrected for double layer charging with a constant current baseline determined as outlined in Sec. 4.1.2) needs to be calculated and then added to the charge of just the potential hold. Doing so yields the blue data set in Fig. 4.37, which show charge values that are comparable to the charges found in the Pt(100) step experiment from the double layer region (Fig. 4.30). The similarity in these values leads to the conclusion that both potential step and sweep-hold experiments capture the entire oxidation process at that step, and both are valid methods of studying oxide growth. Performing sweep-hold experiments whenever possible appears to be simpler electrochemically because it would require less processing in order to get the correct charge (ie no

constant baseline correction for things like hydrogen peroxide oxidation or background noise as was required for the step experiments both of which are shown in Sec. 4.2.2). However, the sweep-hold experiment doesn't show the two components of the current decay and therefore may be less useful when studying specifically the kinetics of the oxide growth and furthering the understanding of the work presented in this thesis. The results of this section and the entire fourth chapter will be summarized next in the final chapter.

Chapter 5

Conclusions

This thesis analyzes electrochemical and X-ray data collected at synchrotron facilities in Grenoble, France (ESRF) and Hamburg, Germany (DESY). Various types of electrochemical experiments such as cyclic voltammetry, potential step experiments, and sweep-hold experiments were conducted on the three low index platinum surfaces (111), (110), and (100). From analyzing the cyclic voltammetry (CV) data, the amount of charge and number of electrons passed that are attributed to the formation of the platinum oxide can be determined and then compared between the three platinum surfaces studied. The charge at various potentials can be tested via potential step experiments and then compared between the surfaces. Additionally, by comparing the resulting electrochemical charge and coverage to the results of the X-ray data, the oxidation number of the oxide species being formed on the surface can be determined.

One outcome of this research was a surface comparison between Pt(100), Pt(111), and Pt(110). From integrating the oxide peak in CV data, it was found that the charges for the initial oxidation for all three surfaces are within 15 μC cm^{-2} or about 0.1 ML of each other. Converted to electrons per surface atom, θ_e, the value is about 0.1 ML which leads to the conclusion that about the same amount of oxide is being

formed on each of the three surfaces. By comparing the X-ray data to the θ_e values for the oxide peak of Pt(111), it was concluded that the oxide being formed on that surface is in the 2+ oxidation state, which would be consistent with PtO.

Potential step experiments were conducted over a wide range of potentials in the oxide region for Pt(100) and Pt(111). The steps on the Pt(100) surface showed two distinct regions of current decay when stepping to potentials in the oxide region from a potential in the double layer region, however it was determined that the first feature was not attributed to double layer charging by modeling with equivalent circuits. The modeling showed that double layer charging is too fast a process to be seen in the step experiments that were conducted, and need not be corrected for when calculating charge. However, a baseline correction was required in order to accurately determine the charges. Throughout the step experiments, the charges for reduction and oxidation from the same experiment were comparable, meaning the amount that is oxidized and reduced was generally the same. The reduction values were slightly higher each time but not by much. Another outcome of the potential step experiments was a comparison of the charges on Pt(100) for stepping from a potential in the HUPD region versus stepping from a potential in the double layer region. It was found that stepping from a potential in the HUPD region seems to result in charges about 1.5-2 times higher than stepping from potentials in the double layer region. Both experiments show reduction values higher than oxidation values, but the reduction values are noticeably higher when stepping back to the HUPD region, which is attributed to holding at a more negative potential resulting in more reduction. Finally, the charges for the first and second component of the current decay for the oxidation portion of the step experiments were integrated separately and plotted versus potential. It was seen that the first component is one of constant charge that is independent of potential which indicate a process that doesn't change with potential, like adsorption. The second component appeared to increase somewhat linearly with potential. A two step reaction mechanism for oxidation was proposed

with the first step being PtOH adsorption and the second step being the creation of PtO from the adsorbed PtOH.

A sweep-hold experiment was conducted on Pt(100) in 0.1 M H_2SO. Noticeably the current decay at the hold potential in the oxide region showed only a single decay feature, unlike the step experiments which showed two. This was attributed to the first feature being something that happened at potentials lower than the hold potentials on the sweep experiment and so the current decay appears to have just one feature. Comparing the sweep-hold data to the corresponding step experiment on Pt(100), it can be seen that the charges are smaller for the sweep-hold experiment than for the step experiment. This is attributed to charge being lost in the sweep experiment at potentials in the oxide region that are lower than the hold potential that otherwise would've been captured in the step experiment to the same potential. To accurately compare these, the entire oxidation peak needed to be integrated and then added on to the charge calculated from the current decay at the hold potential. In doing this, it was found that the values for charge were similar when calculated via the data from the sweep-hold experiment and potential step experiment from a potential in the double layer region. This led to the conclusion that although performing sweep-hold and potential step experiments both give similar charge values and are valid methods of studying oxide growth, step experiments show the two components in the current decay and so performing potential step experiments to study kinetics in the future of this project would be advisable.

The future of this project is quite vast. A good start to expanding this research in the short term would be to compare the CV data for Pt(100) and Pt(110) with the X-ray data to find out if the slope of those graphs also conclude the formation of a 2+ oxidation species or if a different species is being formed on the various surfaces. Second, continuing with the fitting of the current decay on the step experiments for Pt(111) and Pt(100) from various hold potentials to test for the kinetic rate law would hopefully result in a calculation of the rate law and rate constant(s) for the oxidation

process. This could then be expanded to the Pt(110) surface.

In the longer term, it would be interesting to run the same experiments under different conditions (different electrolytes, in a non-inert atmosphere, etc). The experiments and calculations done in this thesis could be performed on higher index platinum surfaces, as well as be expanded to alloys of platinum to see how the presence of other metals effects the oxidation process (once the surface restructuring of platinum is well understood). In addition, expanding this research and running impedance experiments in parallel with the X-ray experiments could give more detailed insight into the kinetics of the oxidation and reduction pathways. It would also be interesting to test what happens to the surface over long term cycling experiments. Knowledge about the growth of oxide on platinum electrocatalysts is important as it affects the activity of the catalysts and their degradation through surface restructuring and dissolution. It is hoped that the fundamental insight from this study can help show the way toward improving platinum based catalysts, which are key in energy technologies such as fuel cells and electrolyzers.

References

[1] Mark C. Williams. Status and promise of fuel cell technology. *Fuel Cells*, 1(2):87–91, 2001.

[2] Tom R. Ralph. *Basic Principles of Fuel Cells*. Taylor and Francis, 2005.

[3] Hikmet Karakoc, Adnan Midilli, and Onder Turan. Green hydrogen and fuel cell systems. *International Journal of Energy Research*, 37(10):1141–1141, 2013.

[4] Shunichi Fukuzumi and Yusuke Yamada. Hydrogen peroxide used as a solar fuel in one-compartment fuel cells. *ChemElectroChem*, 3(12):1978–1989, 2016.

[5] Shunichi Fukuzumi, Yong-Min Lee, and Wonwoo Nam. Fuel production from seawater and fuel cells using seawater. *ChemSusChem*, 10(22):4264–4276, 2017.

[6] Peter Hoffman. *Tomorrow's Energy: Hydrogen, Fuel Cells, and the Prospects for a Cleaner Planet*. The MIT Press, 2012.

[7] William Davis. The world at one. *BBC Radio Times*, 182(2360), 1969.

[8] Ana M Gómez-Marín, Ruben Rizo, and Juan M Feliu. Some reflections on the understanding of the oxygen reduction reaction at pt(111). *Beilstein Journal of Nanotechnology*, 4:956–967, 2013.

[9] Vojislav R. Stamenkovic, Dusan Strmcnik, Pietro P. Lopes, and Nenad M. Markovic. Energy and fuels from electrochemical interfaces. *Nature Materials*, 16(1):57–69, 2016.

[10] C. P. Grey and J. M. Tarascon. Sustainability and in situ monitoring in battery development. *Nature Materials*, 16(1):45–56, 2016.

[11] Steven G. Rinaldo, Wendy Lee, Jürgen Stumper, and Michael Eikerling. Mechanistic principles of platinum oxide formation and reduction. *Electrocatalysis*, 5(3):262–272, 2014.

[12] Robert M. Darling and Jeremy P. Meyers. Kinetic model of platinum dissolution in PEMFCs. *Journal of The Electrochemical Society*, 150(11):A1523–A1527, 2003.

[13] Heather A. Baroody, Gregory Jerkiewicz, and Michael H. Eikerling. Modelling oxide formation and growth on platinum. *The Journal of Chemical Physics*, 146(14):144102, 2017.

[14] The US Department of Energy. Fuel cells, 2020. `https://www.energy.gov/sites/prod/files/2015/11/f27/fcto_fuel_cells_fact_sheet.pdf`.

[15] Holly L. S. Salerno, Frederick L. Beyer, and Yossef A. Elabd. Anion exchange membranes derived from nafion precursor for the alkaline fuel cell. *Journal of Polymer Science Part B: Polymer Physics*, 50(8):552–562, 2011.

[16] Khalid Zakaria, Matthew McKay, Ravikumar Thimmappa, Maksudul Hasan, Mohamed Mamlouk, and Keith Scott. Direct glycerol fuel cells: Comparison with direct methanol and ethanol fuel cells. *ChemElectroChem*, 6(9):2578–2585, 2019.

[17] Lidan Wang, Ying Liu, and Jianyou Wang. Crosslinked anion exchange membrane with improved membrane stability and conductivity for alkaline fuel cells. *Journal of Applied Polymer Science*, 136(44):48169, 2019.

[18] Takashi Hibino, Yanbai Shen, Masakazu Nishida, and Masahiro Nagao. ChemInform abstract: Hydroxide ion conducting antimony(v)-doped tin pyrophos-

phate electrolyte for intermediate-temperature alkaline fuel cells. *ChemInform*, 44(5), 2013.

[19] C. Lafforgue, A. Zadick, L. Dubau, F. Maillard, and M. Chatenet. Selected review of the degradation of pt and pd-based carbon-supported electrocatalysts for alkaline fuel cells: Towards mechanisms of degradation. *Fuel Cells*, 18(3):229–238, 2018.

[20] Holly L. S. Salerno and Yossef A. Elabd. Anion exchange membranes derived from nafion precursor for the alkaline fuel cell: Effect of cation type on properties. *Journal of Applied Polymer Science*, 127(1):298–307, 2012.

[21] Paul Stonehart. "development of advanced noble metal-alloy electrocatalysts for phosphoric acid fuel cells (PAFC)". *Berichte der Bunsengesellschaft für physikalische Chemie*, 94(9):913–921, 1990.

[22] D.-T. Chin and P. D. Howard. ChemInform abstract: Hydrogen sulfide poisoning of platinum anode in phosphoric acid fuel cell electrolyte. *ChemInform*, 18(14), 1987.

[23] J.M. Andújar and F. Segura. Fuel cells: History and updating. a walk along two centuries. *Renewable and Sustainable Energy Reviews*, 13(9):2309–2322, 2009.

[24] Mark K. Debe. Electrocatalyst approaches and challenges for automotive fuel cells. *Nature*, 486(7401):43–51, 2012.

[25] Yuefeng Song, Xiaomin Zhang, Kui Xie, Guoxiong Wang, and Xinhe Bao. High-temperature CO2 electrolysis in solid oxide electrolysis cells: Developments, challenges, and prospects. *Advanced Materials*, 31(50):1902033, 2019.

[26] Kodjo Agbossou, Mohan Lal Kolhe, Jean Hamelin, Étienne Bernier, and Tapan K. Bose. Electrolytic hydrogen based renewable energy system with oxygen recovery and re-utilization. *Renewable Energy*, 29(8):1305–1318, 2004.

[27] Frank A. de Bruijn, Robert C. Makkus, Ronald K.A.M. Mallant, and Gaby J.M. Janssen. Materials for state-of-the-art PEM fuel cells, and their suitability for operation above 100 deg c. In *Advances in Fuel Cells*, pages 235–336. Elsevier, 2007.

[28] Frédéric Maillard, Nathalie Job, and Marian Chatenet. Approaches to synthesize carbon-supported platinum-based electrocatalysts for proton-exchange membrane fuel cells. In *New and Future Developments in Catalysis*, pages 407–428. Elsevier, 2013.

[29] H. Angerstein-Kozlowska, B. MacDougall, and B. E. Conway. Origin of activation effects of acetonitrile and mercury in electrocatalytic oxidation of formic acid. *Journal of The Electrochemical Society*, 120(6):756, 1973.

[30] Wei Chen, Munil Sin, Ping-Jie Wei, Qian-Ling Zhang, and Jin-Gang Liu. Synergistic enhancement of electrocatalytic activity toward oxygen reduction reaction in alkaline electrolytes with pentabasic (fe, b, n, s, p)-doped reduced graphene oxide. *Chinese Journal of Chemistry*, 34(9):878–886, 2016.

[31] Nenad Markovic. Kinetics of oxygen reduction on pt(hkl) electrodes: Implications for the crystallite size effect with supported pt electrocatalysts. *Journal of The Electrochemical Society*, 144(5):1591, 1997.

[32] Pietro P. Lopes, Dusan Tripkovic, Pedro F.B.D. Martins, Dusan Strmcnik, Edson A. Ticianelli, Vojislav R. Stamenkovic, and Nenad M. Markovic. Dynamics of electrochemical pt dissolution at atomic and molecular levels. *Journal of Electroanalytical Chemistry*, 819:123–129, 2018.

[33] V. Climent and Juan M. Feliu. Thirty years of platinum single crystal electrochemistry. *Journal of Solid State Electrochemistry*, 15(7-8):1297–1315, 2011.

[34] Jeffrey Greeley and Nenad M. Markovic. The road from animal electricity to green energy: combining experiment and theory in electrocatalysis. *Energy & Environmental Science*, 5(11):9246, 2012.

[35] A. Hamnett. Mechanism and electrocatalysis in the direct methanol fuel cell. *Catalyst Today*, 38:445–457, 1997.

[36] J. Clavilier. The role of anion on the electrochemical behaviour of a 111 platinum surface an unusual splitting of the voltammogram in the hydrogen region. *Journal of Electroanalytical Chemistry and Interfacial Electrochemistry*, 107(1):211–216, 1980.

[37] M.D. Maciá, J.M. Campiña, E. Herrero, and J.M. Feliu. On the kinetics of oxygen reduction on platinum stepped surfaces in acidic media. *Journal of Electroanalytical Chemistry*, 564:141–150, 2004.

[38] Sanjeev Mukerjee, Supramaniam Srinivasan, Manuel P. Soriaga, and James McBreen. Effect of preparation conditions of pt alloys on their electronic, structural, and electrocatalytic activities for oxygen reduction - XRD, XAS, and electrochemical studies. *The Journal of Physical Chemistry*, 99(13):4577–4589, 1995.

[39] Maggie Teliska, Vivek S. Murthi, Sanjeev Mukerjee, and David E. Ramaker. Correlation of water activation, surface properties, and oxygen reduction reactivity of supported pt–m/c bimetallic electrocatalysts using XAS. *Journal of The Electrochemical Society*, 152(11):A2159, 2005.

[40] G. Tremiliosi-Filho, G. Jerkiewicz, and B. E. Conway. Characterization and significance of the sequence of stages of oxide film formation at platinum generated by strong anodic polarization. *Langmuir*, 8(2):658–667, 1992.

[41] Serhiy Cherevko, Nadiia Kulyk, and Karl J.J. Mayrhofer. Durability of platinum-based fuel cell electrocatalysts: Dissolution of bulk and nanoscale platinum. *Nano Energy*, 29:275–298, 2016.

[42] Joseph H. Montoya, Linsey C. Seitz, Pongkarn Chakthranont, Aleksandra Vojvodic, Thomas F. Jaramillo, and Jens K. Nørskov. Materials for solar fuels and chemicals. *Nature Materials*, 16(1):70–81, 2016.

[43] R. Wilson and A.P.F. Turner. Glucose oxidase: an ideal enzyme. *Biosensors and Bioelectronics*, 7(3):165–185, 1992.

[44] Joseph Wang. Electrochemical biosensors: Towards point-of-care cancer diagnostics. *Biosensors and Bioelectronics*, 21(10):1887–1892, 2006.

[45] B.E. Conway. Reflections on directions of electrochemical surface science as a leading edge of surface chemistry. *Journal of Electroanalytical Chemistry*, 524-525:4–19, 2002.

[46] Sergio Trasatti. 1799–1999: Alessandro voltas 'electric pile'. *Journal of Electroanalytical Chemistry*, 460(1-2):1–4, 1999.

[47] Emmanuel Zoulias, Elli Varkaraki, Nicolaos Lymberopoulos, Christodoulos N. Christodoulou, and George N. Karagiorgis. A review on water electrolysis. http://www.cres.gr/kape/publications/papers/dimosieyseis/ydrogen/AW

[48] Hermann Berg. Johann wilhelm ritter - the founder of scientific electrochemistry. *Review of Polarography*, 54(2):99–103, 2008.

[49] Chengxiang Xiang, Kimberly M. Papadantonakis, and Nathan S. Lewis. Principles and implementations of electrolysis systems for water splitting. *Materials Horizons*, 3(3):169–173, 2016.

[50] L. Carrette, K. A. Friedrich, and U. Stimming. Fuel cells - fundamentals and applications. *Fuel Cells*, 1(1):5–39, 2001.

[51] N. M. Marković, T. J. Schmidt, V. Stamenković, and P. N. Ross. Oxygen reduction reaction on pt and pt bimetallic surfaces: A selective review. *Fuel Cells*, 1(2):105–116, 2001.

[52] Roger Parsons. Interfaces in electrochemistry. *J. Electrochem. Soc.*, 127(176C), 1980.

[53] Roger Parsons and Richard Payne. The interface between mercury and aqueous perchloric acid. *Zeitschrift für Physikalische Chemie*, 98(1-6):9–22, 1975.

[54] Roger Parsons. The electrical double layer at solid/liquid interfaces. *Journal of Electroanalytical Chemistry and Interfacial Electrochemistry*, 118:3–18, 1981.

[55] B. E. Conway, B. Barnett, H. Angerstein-Kozlowska, and B. V. Tilak. A surface-electrochemical basis for the direct logarithmic growth law for initial stages of extension of anodic oxide films formed at noble metals. *The Journal of Chemical Physics*, 93(11):8361–8373, 1990.

[56] B.E. Conway. Electrochemical oxide film formation at noble metals as a surface-chemical process. *Progress in Surface Science*, 49(4):331–452, 1995.

[57] H. Angerstein-Kozlowska, B.E. Conway, K. Tellefsen, and B. Barnett. Stochastically-gated surface processes involving anions in oxidation of au. *Electrochimica Acta*, 34(8):1045–1056, 1989.

[58] D. Gilroy and B. E. Conway. Surface oxidation and reduction of platinum electrodes: Coverage, kinetic and hysteresis studies. *Canadian Journal of Chemistry*, 46(6):875–890, 1968.

[59] Brian E. Conway and Gregory Jerkiewicz. Surface orientation dependence of oxide film growth at platinum single crystals. *Journal of Electroanalytical Chemistry*, 339(1-2):123–146, 1992.

[60] Selwyn Hanselman, Ian T. McCrum, Marcel J. Rost, and Marc T. M. Koper. Thermodynamics of the formation of surface PtO2 stripes on pt(111) in the absence of subsurface oxygen. *Physical Chemistry Chemical Physics*, 22(19):10634–10640, 2020.

[61] David A. Harrington. Simulation of anodic pt oxide growth. *Journal of Electroanalytical Chemistry*, 420(1-2):101–109, 1997.

[62] Darrick V. Heyd and David A. Harrington. Platinum oxide growth kinetics for cyclic voltammetry. *Journal of Electroanalytical Chemistry*, 335(1-2):19–31, 1992.

[63] Ana M[a]. Gómez-Marín and Juan M. Feliu. Oxide growth dynamics at pt(111) in absence of specific adsorption: A mechanistic study. *Electrochimica Acta*, 104:367–377, 2013.

[64] Ana M. Gómez-Marín, Jean Clavilier, and Juan M. Feliu. Sequential pt(111) oxide formation in perchloric acid: An electrochemical study of surface species inter-conversion. *Journal of Electroanalytical Chemistry*, 688:360–370, 2013.

[65] Ana Ma. Gómez-Marín and Juan M. Feliu. Pt(111) surface disorder kinetics in perchloric acid solutions and the influence of specific anion adsorption. *Electrochimica Acta*, 82:558–569, 2012.

[66] Yi-Fan Huang, Patricia J. Kooyman, and Marc T. M. Koper. Intermediate stages of electrochemical oxidation of single-crystalline platinum revealed by in situ raman spectroscopy. *Nature Communications*, 7(1), 2016.

[67] Hideto Imai, Koichi Izumi, Masashi Matsumoto, Yoshimi Kubo, Kazuo Kato, and Yasuhiko Imai. In situ and real-time monitoring of oxide growth in a few monolayers at surfaces of platinum nanoparticles in aqueous media. *Journal of the American Chemical Society*, 131(17):6293–6300, 2009.

[68] Jakub Drnec, Martin Ruge, Finn Reikowski, Björn Rahn, Francesco Carlà, Roberto Felici, Jochim Stettner, Olaf M. Magnussen, and David A. Harrington. Initial stages of pt(111) electrooxidation: dynamic and structural studies by surface x-ray diffraction. *Electrochimica Acta*, 224:220–227, 2017.

[69] J. Clavilier, R. Faure, G. Guinet, and R. Durand. Preparation of monocrystalline pt microelectrodes and electrochemical study of the plane surfaces cut in the direction of the {111} and {110} planes. *Journal of Electroanalytical Chemistry and Interfacial Electrochemistry*, 107(1):205–209, 1980.

[70] J. Clavilier, R. Durand, G. Guinet, and R. Faure. Electrochemical adsorption behaviour of pt(100) in sulphuric acid solution. *Journal of Electroanalytical Chemistry and Interfacial Electrochemistry*, 127(1-3):281–287, 1981.

[71] F.T. Wagner and P.N. Ross. Leed analysis of electrode surfaces. *Journal of Electroanalytical Chemistry and Interfacial Electrochemistry*, 150(1-2):141–164, 1983.

[72] S. Motoo and N. Furuya. Electrochemistry of platinum single crystal surfaces. *Journal of Electroanalytical Chemistry and Interfacial Electrochemistry*, 172(1-2):339–358, 1984.

[73] M. Wasberg, L. Palaikis, S. Wallen, M. Kamrath, and A. Wieckowski. Leed / auger verification of the in situ method of preparation of pt (111) single crystal electrodes. *Journal of Electroanalytical Chemistry and Interfacial Electrochemistry*, 256(1):51–63, 1988.

[74] JosÃl' Solla-GullÃşn. Surface characterization of platinum electrodes. *Phys. Chem. Chem. Phys.*, 10(10):1359–1373, 2008.

[75] Hiroyuki Tanaka, Seiho Sugawara, Kazuhiko Shinohara, Takahiro Ueno, Shunsuke Suzuki, Nagahiro Hoshi, and Masashi Nakamura. Infrared reflection ab-

sorption spectroscopy of OH adsorption on the low index planes of pt. *Electrocatalysis*, 6(3):295–299, 2014.

[76] Carey L. Scortichnini and Charles N. Reilley. Surface characterization of pt electrodes using underpotential deposition of h and cu. *Journal of Electroanalytical Chemistry and Interfacial Electrochemistry*, 139(2):233–245, 1982.

[77] Carey L. Scortichini and Charles N. Reilley. Surface characterization of pt electrodes using underpotential deposition of h and cu. *Journal of Electroanalytical Chemistry and Interfacial Electrochemistry*, 139(2):247–264, 1982.

[78] C.L. Scortichini, F.E. Woodward, and C.N. Reilley. Surface characterization of pt electrodes using underpotential deposition of h and cu. *Journal of Electroanalytical Chemistry and Interfacial Electrochemistry*, 139(2):265–274, 1982.

[79] Roger Parsons. The rate of electrolytic hydrogen evolution and the heat of adsorption of hydrogen. *Transactions of the Faraday Society*, 54:1053, 1958.

[80] Jakub Tymoczko, Wolfgang Schuhmann, and Aliaksandr S. Bandarenka. The constant phase element reveals 2d phase transitions in adsorbate layers at the electrode/electrolyte interfaces. *Electrochemistry Communications*, 27:42–45, 2013.

[81] N Markovic. Surface science studies of model fuel cell electrocatalysts. *Surface Science Reports*, 45(4-6):117–229, 2002.

[82] Nuria Garcia-Araez, Victor Climent, and Juan M. Feliu. Analysis of temperature effects on hydrogen and OH adsorption on pt(111), pt(100) and pt(110) by means of gibbs thermodynamics. *Journal of Electroanalytical Chemistry*, 649(1-2):69–82, 2010.

[83] A Berna, V Climent, and J Feliu. New understanding of the nature of OH adsorption on pt(111) electrodes. *Electrochemistry Communications*, 9(12):2789–2794, 2007.

[84] Nuria Garcia-Araez, Victor Climent, Paramaconi Rodriguez, and Juan M. Feliu. Elucidation of the chemical nature of adsorbed species for pt(111) in h2so4solutions by thermodynamic analysis. *Langmuir*, 26(14):12408–12417, 2010.

[85] Víctor Climent, Roberto Gómez, José M. Orts, and Juan M. Feliu. Thermodynamic analysis of the temperature dependence of OH adsorption on pt(111) and pt(100) electrodes in acidic media in the absence of specific anion adsorption. *The Journal of Physical Chemistry B*, 110(23):11344–11351, 2006.

[86] Vladimir Tripković, Egill Skúlason, Samira Siahrostami, Jens K. Nørskov, and Jan Rossmeisl. The oxygen reduction reaction mechanism on pt(111) from density functional theory calculations. *Electrochimica Acta*, 55(27):7975–7981, 2010.

[87] Enrique Herrero and Juan M. Feliu. Kinetics at single crystal electrodes. In *Electrochemical Science for a Sustainable Society*, pages 113–146. Springer International Publishing, 2017.

[88] Akiyoshi Kuzume, Enrique Herrero, and Juan M. Feliu. Oxygen reduction on stepped platinum surfaces in acidic media. *Journal of Electroanalytical Chemistry*, 599(2):333–343, 2007.

[89] Yihua Liu, Andi Barbour, Vladimir Komanicky, and Hoydoo You. X-ray crystal truncation rod studies of surface oxidation and reduction on pt(111). *The Journal of Physical Chemistry C*, 120(29):16174–16178, 2016.

[90] H. You, D. J. Zurawski, Z. Nagy, and R. M. Yonco. In-situ x-ray reflectivity study of incipient oxidation of pt(111) surface in electrolyte solutions. *The Journal of Chemical Physics*, 100(6), March 1994.

[91] Jakub Drnec, David A. Harrington, and Olaf M. Magnussen. Electrooxidation of pt(111) in acid solution. *Current Opinion in Electrochemistry*, 4(1):69–75, 2017.

[92] Wanda Lew, Matthew C. Crowe, Eric Karp, Ole Lytken, Jason A. Farmer, Líney Árnadóttir, Carolyn Schoenbaum, and Charles T. Campbell. The energy of adsorbed hydroxyl on pt(111) by microcalorimetry. *The Journal of Physical Chemistry C*, 115(23):11586–11594, 2011.

[93] Timo Fuchs, Jakub Drnec, Federico Calle-Vallejo, Natalie Stubb, Daniel J. S. Sandbeck, Martin Ruge, Serhiy Cherevko, David A. Harrington, and Olaf M. Magnussen. Structure dependency of the atomic-scale mechanisms of platinum electro-oxidation and dissolution. *Nature Catalysis*, 2020.

[94] Alexander Björling and Juan M. Feliu. Electrochemical surface reordering of pt(111): A quantification of the place-exchange process. *Journal of Electroanalytical Chemistry*, 662(1):17–24, 2011.

[95] Gary A. Attard and Ashley Brew. Cyclic voltammetry and oxygen reduction activity of the pt{110}-(1x1) surface. *Journal of Electroanalytical Chemistry*, 747:123–129, 2015.

[96] Gary A. Attard, Katherine Hunter, Edward Wright, Jonathan Sharman, Ricardo Martínez-Hincapié, and Juan M. Feliu. The voltammetry of surfaces vicinal to pt{110}: Structural complexity simplified by CO cooling. *Journal of Electroanalytical Chemistry*, 793:137–146, 2017.

[97] Gary A. Attard, Katherine Hunter, Edward Wright, Jonathan Sharman, Ricardo Martínez-Hincapié, and Juan M. Feliu. The voltammetry of surfaces

vicinal to pt{110}: Structural complexity simplified by CO cooling. *Journal of Electroanalytical Chemistry*, 793:137–146, 2017.

[98] Mujib Ahmed, Gary A. Attard, Edward Wright, and Jonathan Sharman. Methanol and formic acid electrooxidation on nafion modified pd/pt{111}: The role of anion specific adsorption in electrocatalytic activity. *Catalysis Today*, 202:128–134, 2013.

[99] Gary A. Attard, Ashley Brew, Jin-Yu Ye, David Morgan, and Shi-Gang Sun. Oxygen reduction reaction activity on pt{111} surface alloys. *ChemPhysChem*, 15(10):2044–2051, 2014.

[100] David W.H. Rankin. CRC handbook of chemistry and physics, 89th edition, edited by david r. lide. *Crystallography Reviews*, 15(3):223–224, 2009.

[101] Zsolt Kerner, Tamás Pajkossy, Ludwig A Kibler, and Dieter M Kolb. The double layer capacity of pt(100) in aqueous perchlorate solutions. *Electrochemistry Communications*, 4(10):787–789, 2002.

[102] T. Pajkossy and D.M. Kolb. Double layer capacitance of pt(111) single crystal electrodes. *Electrochimica Acta*, 46(20-21):3063–3071, 2001.

[103] *Crystal data: determinative tables*. American Crystallographic Association, 2 edition, 1963.

[104] Victor Climent and Juan M. Feliu. Surface electrochemistry with pt single-crystal electrodes. In *Advances in Electrochemical Sciences and Engineering*, pages 1–57. Wiley-VCH Verlag GmbH & Co. KGaA, 2017.

[105] Mahesh G. Samant, Michael F. Toney, Gary L. Borges, Lesser Blum, and Owen R. Melroy. Grazing incidence x-ray diffraction of lead monolayers at a silver (111) and gold (111) electrode/electrolyte interface. *The Journal of Physical Chemistry*, 92(1):220–225, 1988.

[106] Mahesh G. Samant, Michael F. Toney, Gary L. Borges, Lesser Blum, and Owen R. Melroy. In-situ grazing incidence x-ray diffraction study of electrochemically deposited pb monolayers on ag(111). *Surface Science*, 193(1-2):L29–L36, 1988.

[107] Jia Wang, B. M. Ocko, Alison J. Davenport, and Hugh S. Isaacs. In situx-ray-diffraction and -reflectivity studies of the au(111)/electrolyte interface: Reconstruction and anion adsorption. *Physical Review B*, 46(16):10321–10338, 1992.

[108] José Solla-Gullón, Paramaconi Rodríguez, Enrique Herrero, Antonio Aldaz, and Juan M. Feliu. Surface characterization of platinum electrodes. *Phys. Chem. Chem. Phys.*, 10(10):1359–1373, 2008.

[109] TotalBoox and TBX. *In-situ Spectroscopic Studies of Adsorption at the Electrode and Electrocatalysis.* Elsevier Science, 2011.

[110] John Newman. Resistance for flow of current to a disk. *Journal of The Electrochemical Society*, 113(5):501, 1966.